

**Measurement of the Deep-Inelastic  
ep Scattering Cross Section  
using the Backward Silicon Tracker  
at the H1 Detector at HERA**

**DISSERTATION**

zur Erlangung des akademischen Grades  
**doctor rerum naturalium**  
(Dr. rer. nat.)

im Fach Physik

eingereicht an der

Mathematisch-Naturwissenschaftlichen Fakultät I  
der Humboldt-Universität zu Berlin

von

**Vladimir Vladimirovich Arkadov**

geboren am 24. Mai 1973 in Novomoskovsk, UdSSR

Präsident der Humboldt-Universität zu Berlin  
Prof. Dr. Dr. hc. H. Meyer

Dekan der Mathematisch-Naturwissenschaftlichen Fakultät I  
Prof. Dr. B. Ronacher

Gutachter/innen:

1. Prof. Dr. Th. Lohse
2. Prof. Dr. H. Kolanoski
3. Prof. Dr. C. Kiesling

Tag der mündlichen Prüfung: 31.10.2000

## Abstract

A measurements of the inclusive cross section for the deep-inelastic scattering of positrons off protons is presented at four momentum transfers squared  $1.5 \leq Q^2 \leq 15 \text{ GeV}^2$  in the Bjorken  $x$  range between 0.000024 and 0.075. The analysis is based on data collected by the H1 experiment at HERA in the year 1997 taken during a special minimum bias run for low  $Q^2$  values. A Backward Silicon Tracker (BST) has been used in this measurement for the first time. Use of this new detector component, as presented in this thesis, led to an extension of the kinematical region of the measurement towards high values of inelasticity  $y$  at low  $Q^2$  as well as towards the low  $y$  region which overlaps with fixed target experiments. The precision of the measurement is for the first time dominated by the systematic uncertainties. These are of the order of 3% as compared to typically 1-2% statistical accuracy. Part of the results presented in this analysis has been included into an H1 publication.

## Zusammenfassung

In der vorliegenden Arbeit wird die Messung des inklusiven tief-inelastischen Streuquerschnitts von Positronen an Protonen für Viererimpulsüberträge  $Q^2$  zwischen 1.5 und 15  $\text{GeV}^2$  und Werte der Bjorken- $x$  Variable zwischen 0.000024 und 0.075 beschrieben. Die Messung beruht auf speziellen Daten, die im Herbst des Jahres 1997 mit dem H1-Experiment am Beschleuniger HERA aufgezeichnet wurden. Zum ersten Mal wird der rückwärtige Silizium-Streifendetektor (BST) des H1-Experimentes für diese Messung verwendet. Die hier dargestellten Untersuchungen mit dieser neuen Detektorkomponente führen zu einer Erweiterung des kinematischen Meßbereiches, der nun sowohl große Inelastizitätswerte von  $y > 0.6$  bei niedrigen  $Q^2$  als auch eine Überlappung mit Daten von "Fixed Target"-Müon-Proton-Streuexperimenten erreicht. Erstmalg wird die Präzision dieser Messung von den systematischen Fehlern von etwa 3% dominiert, im Vergleich zu statistischen Fehlern von 1-2%. Die Resultate der Analyse wurden teilweise in eine Publikation der H1-Kollaboration aufgenommen.

# Contents

<b>1</b>	<b>Introduction</b>	<b>4</b>
<b>2</b>	<b>Theoretical Basics of Deep Inelastic Scattering</b>	<b>6</b>
2.1	A Bit of History . . . . .	6
2.2	Cross Section Calculation . . . . .	9
2.2.1	The DIS Kinematics . . . . .	9
2.2.2	Cross Section in Born Approximation . . . . .	10
2.2.3	Quark Parton Model . . . . .	12
2.2.4	Quantum Chromodynamics and DIS . . . . .	13
<b>3</b>	<b>The H1 Detector at HERA</b>	<b>17</b>
3.1	The HERA Accelerator . . . . .	17
3.2	Detector Overview . . . . .	18
3.2.1	Luminosity System . . . . .	19
3.2.2	Track Detectors . . . . .	21
3.2.3	Liquid Argon Calorimeter . . . . .	22
3.2.4	Backward Detectors . . . . .	23
3.2.5	Trigger System . . . . .	26
3.3	Kinematics Reconstruction . . . . .	27
3.4	Event and Detector Simulation . . . . .	31
3.5	The Data Sample . . . . .	32
3.5.1	Trigger and DAQ . . . . .	32
3.5.2	Run Selection and Time Stability . . . . .	33

<b>4</b>	<b>The Backward Silicon Tracker</b>	<b>36</b>
4.1	Purpose . . . . .	36
4.2	Design . . . . .	39
4.3	Data Acquisition . . . . .	41
4.4	Offline Reconstruction . . . . .	45
4.5	Internal Efficiencies . . . . .	47
4.6	Coherent losses . . . . .	48
4.7	Simulation of the BST . . . . .	51
4.8	Alignment . . . . .	51
4.8.1	Internal Alignment . . . . .	52
4.8.2	External Alignment . . . . .	53
4.8.3	Alignment of SpaCal and BDC . . . . .	54
<b>5</b>	<b>Energy Calibration</b>	<b>59</b>
5.1	Backward Calorimeter (SpaCal) Calibration . . . . .	59
5.2	Calibration of the Liquid Argon Calorimeter . . . . .	61
5.2.1	LAr Calibration with the “Lagrangian” Method . . . . .	63
5.2.2	Cross Check with the Iterative Method . . . . .	71
<b>6</b>	<b>Measurement of the DIS Cross Section</b>	<b>76</b>
6.1	Cross Section Determination . . . . .	76
6.2	Bin Selection . . . . .	78
6.3	Event Selection . . . . .	83
6.3.1	Cluster Radius Cut . . . . .	83
6.3.2	Hadronic Energy Fraction Cut . . . . .	85
6.3.3	$E - P_z$ Cut . . . . .	86
6.3.4	$P_t$ Balance Cut . . . . .	87
6.3.5	BST Related Cuts . . . . .	89
6.3.6	Vertex Position Cut . . . . .	93
6.4	Estimation of the Photoproduction Background . . . . .	94
6.5	Kinematic Distributions . . . . .	98
6.6	Systematic Errors . . . . .	101
6.7	Results for the DIS Cross Section . . . . .	103
6.7.1	Main Kinematic Region . . . . .	103
6.7.2	Cross Section at high $y$ . . . . .	103
6.8	Extraction of $F_2$ . . . . .	106
6.9	Concluding Remarks . . . . .	110

<b>7 Summary</b>	<b>112</b>
<b>A BST Electron Finder</b>	<b>114</b>
A.1 Introduction . . . . .	114
A.2 Objectives of the procedure . . . . .	114
A.3 General Description of the Routine . . . . .	115
A.4 Case 1: central vertex exists . . . . .	116
A.5 Case 2: central vertex does not exist . . . . .	120
A.6 Results . . . . .	122

# Chapter 1

## Introduction

A measurement of the inclusive deep-inelastic electron-proton scattering (DIS) differential cross section is presented using the H1 detector at HERA and, for the first time, the Backward Silicon Tracker (BST). The BST was fabricated by the H1 group in Zeuthen and installed in 1996. Its installation completed the upgrade of the backward apparatus of the H1 detector which consisted of replacing a Pb-Scintillator calorimeter (BEMC) by a Pb-fiber calorimeter (SpaCal) of high granularity and a multiwire proportional chamber (BPC) by a planar drift chamber (BDC). The analysis of the DIS cross section benefits from the high resolution of the angular measurement with the silicon tracker allowing also for electron identification and, thus, suppression of the neutral component of the photoproduction background. The latter is essential to extend the cross section measurement towards the kinematic region of large inelasticity  $y$  which permits the longitudinal structure function  $F_L$  to be accessed. At low  $y$  the event vertex is reconstructed using the scattered electron track measured with the BST. Thus, DIS events are identified and the kinematic region of the DIS fixed target experiments is reached.

The data used here were collected in September and October 1997 during a special data taking period dedicated to the region of low momentum transfers  $Q^2$ . The data set corresponds to an integrated luminosity of about  $2 \text{ pb}^{-1}$  resulting in typically 1–2% statistical errors. The high statistics of the data and new backward instrumentation allowed to understand systematic effects better than in previous DIS cross section analyses at low  $Q^2$ .

This thesis is organized as follows:

- The second chapter gives an introduction to the theory of deep inelastic scattering. Theoretical predictions for the evolution of the DIS cross section and the proton structure functions are discussed.
- The third chapter overviews the HERA accelerator and the H1 detector. The chapter proceeds with a description of methods for reconstruction of the kinematic variables with the H1 detector. A presentation of the analyzed data and their selection concludes the chapter.

- Chapter 4 introduces the Backward Silicon Tracker, the presented work is essentially based on. The systematic study of the detector response as well as its alignment with respect to the H1 coordinate system are discussed.
- The calibration of the electromagnetic and hadronic energy scales of the backward calorimeter is shortly described in the fifth chapter. Here, the main focus is on aspects of the hadronic energy scale calibration of the liquid argon calorimeter.
- The sixth chapter incorporates all necessary aspects of the double differential DIS cross section measurement. Special attention is paid to the role of the BST event validation in the cross section measurement. The double differential DIS cross section is measured with two different kinematic reconstruction methods which allowed to cross check the correctness of the systematic uncertainties. The chapter concludes with the results for the DIS cross section combined from the two methods depending on their resolutions. Also presented is the structure function  $F_2(x, Q^2)$  extracted from the measured cross section and a discussion of the obtained results.

This work used the BST and the SpaCal calorimeter to derive a cross section measurement. The points at high  $y$  entered the official release of structure function data by the H1 collaboration. The systematic work on the BST has been part of further analyses on the inclusive DIS and exclusive processes.

The thesis has one appendix devoted to an electron finding procedure developed for the DIS cross section measurement with the backward silicon tracker.

# Chapter 2

## Theoretical Basics of Deep Inelastic Scattering

### 2.1 A Bit of History

In 1911, Rutherford used  $\alpha$ -particles to resolve the structure of gold atoms by measuring the angles of the scattered particles [1]. This experiment was done before the Quantum Mechanics was developed which confirmed the cross section formula Rutherford did empirically establish in the non-relativistic case:

$$\frac{d\sigma}{d\Omega} = \frac{\alpha^2}{4(p\beta)^2 \sin^4(\theta/2)}. \quad (2.1)$$

Here,  $\alpha \approx 1/137$  and  $\beta$  denote a fine structure constant and velocity of the projectile, respectively.  $p$  is the momentum of the projectile and  $\theta$  its scattering angle in the laboratory frame where the target is fixed. Eq. 2.1 is written in the case of  $ep$  scattering when both projectile and the target have charge  $Z = 1$ .

The low energetic  $\alpha$ -particles were supposed to be point-like at that time compared to gold atoms. Later the  $\alpha$ -particles were identified with the  $He$  nucleus. To improve the experiment one has thus to take point-like projectiles such as the leptons. When using the spin-1/2 particles, like electrons, the Rutherford formula for scattering cross section receives corrections, which were calculated by Mott [2] in 1932:

$$\left(\frac{d\sigma}{d\Omega}\right)_{Mott} = \left(\frac{d\sigma}{d\Omega}\right) \cdot \frac{\cos^2(\theta/2)}{1 + \frac{2E}{M} \sin^2(\theta/2)}, \quad (2.2)$$

where  $\cos^2(\theta/2)$  and  $\left[1 + \frac{2E}{M} \sin^2(\theta/2)\right]^{-1}$  arise from the spin-1/2 of the electron and the target recoil, respectively.  $E$  corresponds to the energy of the electron and  $M$  is the target mass.

According to the Heisenberg principle ( $\Delta p \cdot \Delta x \sim \hbar$ ), with increasing energy the structure of the proton can be resolved deeper. It was Rosenbluth [3], who proposed

in 1950 to involve the proton electric and magnetic form factors characterizing the deviations from a point-like behavior of the proton. Assuming the proton to have spin  $1/2$ , it gave the Rosenbluth expression for elastic  $ep$  scattering:

$$\left(\frac{d\sigma}{d\Omega}\right)_{ep \rightarrow ep} = \left(\frac{d\sigma}{d\Omega}\right)_{Mott} \left[ \frac{G_E^2 + \tau G_M^2}{1 + \tau} \cos^2(\theta/2) + 2\tau G_M^2 \sin^2(\theta/2) \right], \quad (2.3)$$

where  $\tau \equiv -q^2/4M^2$  and  $G_E$ ,  $G_M$  are the electric and magnetic form factors of the proton, respectively.

In 1953, Hofstadter et al. [4] confirmed the correctness of Rosenbluth's approach. The proton form factors were found to drop sharply with increasing momentum transfer. That was the first evidence for a distributed structure of the proton within the sphere with an estimated radius of  $(0.85 \pm 0.1)$  fm [5]. The success of these early results with the elastic  $ep$  scattering led to the proposal to build a new accelerator at the Stanford Linear Accelerator Center (SLAC).

Meanwhile, theoreticians thought about the description of inelastic electron-proton scattering. At that time Quantum Electrodynamics (QED) was established already as a precise theory, so that the electromagnetic part of cross section description could be accurately calculated. As the basis for inelastic  $ep$  scattering cross section calculation, the result for electron-muon scattering was taken [6]. Then the following result for inelastic  $ep$  scattering cross section was obtained taking into account the unknown structure of the proton parameterized in terms of two structure functions  $W_1$  and  $W_2$  [7]:

$$\left(\frac{d\sigma}{dE'd\Omega}\right)_{ep \rightarrow eX} = \frac{\alpha^2}{4E^2 \sin^4(\theta/2)} \left( W_2(\nu, Q^2) \cos^2(\theta/2) + 2W_1(\nu, Q^2) \sin^2(\theta/2) \right). \quad (2.4)$$

Here, the structure functions  $W_1$  and  $W_2$  are related to their elastic counterparts  $G_E$  and  $G_M$ . They are functions of two independent variables  $\nu$  and  $Q^2$  which correspond to the energy and momentum transfer in the rest frame of the target proton.

$$\nu = E - E', \quad (2.5)$$

$$Q^2 = -q^2 = 4EE' \sin^2(\theta/2). \quad (2.6)$$

The structure functions  $W_1$  and  $W_2$  are underivable from the theory of strong interactions. These must be obtained from the experiment.

The rapidly increasing number of "elementary" particles had suggested that there exist more fundamental constituents of matter than the hadrons. In 1961, Gell-Mann and Ne'eman [8] independently proposed the *Eightfold Way* to classify the known baryons and mesons with the same spin, according to their charge and strangeness, using the SU(3) symmetry. The confirmation of SU(3) group by the discovery of the  $\Omega^-$  baryon in 1963 led to wide acceptance of the "Eightfold Way". This classification scheme could then be explained with elementary particle constituents, called *quarks*. This approach was independently proposed by Gell-Mann [9] and Zweig [10] in 1964.

In 1967, the Stanford linear accelerator started to operate. It was Bjorken [11], who proposed to investigate the structure functions in the limit  $Q^2 \rightarrow \infty$  and  $\nu \rightarrow \infty$  but  $\nu/Q^2$  fixed. He thus introduced a new variable  $x = Q^2/2M\nu$  which had to be kept constant. The most famous result of this pioneering inelastic  $ep$  scattering experiment was the evidence of so called *scaling invariance* of the proton structure functions  $W_1(x, Q^2)$  and  $W_2(x, Q^2)$ , i.e. there was no  $Q^2$  dependence of these functions found [12], i.e. in this Bjorken limit the structure functions tend to depend on the ratio  $x$  only:

$$\lim_{Bj} MW_1(\nu, Q^2) = F_1(x) + O(1/Q^2), \quad (2.7)$$

$$\lim_{Bj} \nu W_2(\nu, Q^2) = F_2(x) + O(1/Q^2). \quad (2.8)$$

This surprising feature was predicted by Bjorken in 1968 and is expected for scattering from a point-like object.

In 1968, Feynman [13] interpreted the SLAC results by applying his parton model. According to this model, the proton is constructed of free partons and the electrons scatter from the partons incoherently. Callan and Gross proposed then to investigate the spin of the partons, predicting that for spin-1/2 partons the equation

$$F_L(x) = 2xF_1(x) - F_2(x) = 0 \quad (2.9)$$

must be valid [14]. SLAC experiments confirmed this expectation. Partons were identified with quarks by Bjorken and Paschos [15] in 1969. The Bjorken  $x$  variable was interpreted as the fraction of parton momentum with  $0 < x < 1$ , where  $x = 1$  corresponds to elastic scattering.

Later, in different regions of  $x$  than originally measured, the violation of the scaling law was found in  $\mu N$  scattering [16]. The scaling violation was explained by gluon bremsstrahlung and pair production. This observation helped to establish a new theory of strong interaction, Quantum Chromodynamics (QCD) which predicted the existence of electrically neutral *gluons*. Experimental evidence of the gluons was observed at DESY by three jets events [17, 18]. QCD in conjunction with the electroweak theory constitute the *Standard Model* of elementary particle physics.

On October 19th, 1991, the first electron-proton colliding facility HERA started to operate at DESY in Hamburg. It greatly extended the kinematic range of DIS experiments towards high  $Q^2$  and low  $x$  since the center of mass energy was enlarged by about three orders of magnitude. The first measurements of  $F_2$  by the H1 [19] and the ZEUS Collaborations [20] discovered a steep rise of  $F_2(x, Q^2)$  towards low  $x$  at fixed  $Q^2$  (see Fig. 2.1). According to present understanding, this rise is due to the dominance of gluons at low  $x$ . A rising behavior was expected by Glück, Reya and Vogt [21]. Results for inclusive  $ep$  DIS cross section obtained at HERA during many years of successful operation yield new deep insight into the structure of the proton allowing for testing the underlying strong interaction theory in unprecedented details. This continues the long tradition of DIS experiments.

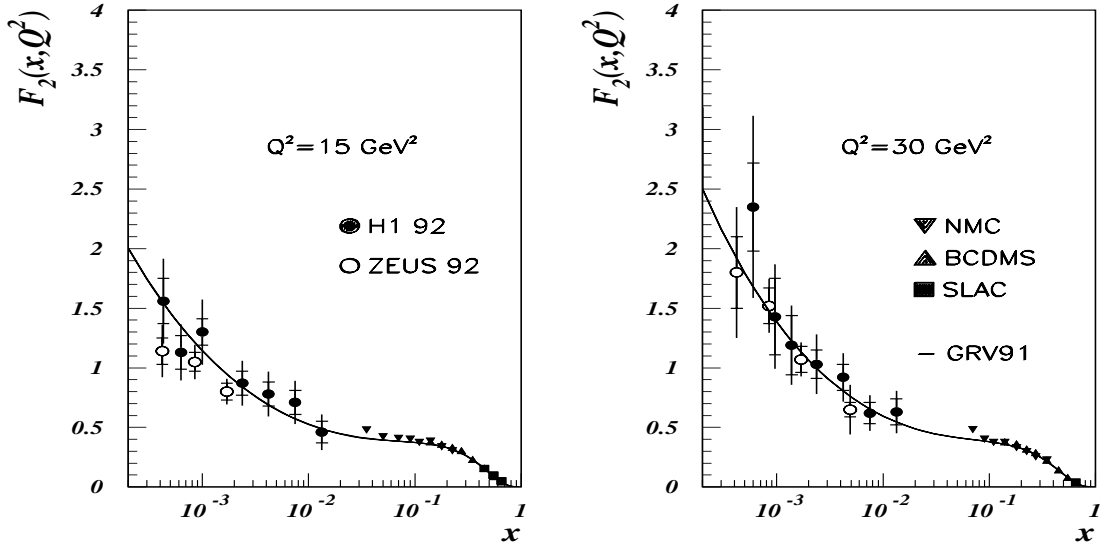


Figure 2.1: Measurements of the proton structure function  $F_2(x, Q^2)$  by the fixed target experiments SLAC, NMC and BCDMS and their extension towards low  $x$  represented by the first HERA data on  $F_2$ . The curve represents the expectation of this rising behavior by GRV'91 [21].

## 2.2 Cross Section Calculation

### 2.2.1 The DIS Kinematics

In inclusive deep inelastic scattering at low  $Q^2$ , the electron scatters off the proton by the exchange of a virtual photon. The diagram of this process,  $ep \rightarrow eX$ , is shown in Fig. 2.2. The four-momentum transfer squared  $Q^2$  and the Bjorken  $x$  variables can be defined by the four momenta of the incident and of the scattered electron and those of the proton:

$$Q^2 = -q^2 = -(k - k'), \quad x = \frac{Q^2}{2Pq}. \quad (2.10)$$

The inelasticity of the reaction is defined by the variable

$$y = \frac{Pq}{Pk}. \quad (2.11)$$

In the rest frame of the proton it corresponds to the relative energy transfer  $y = \nu/E$ . Another important variable of the DIS process is the invariant mass squared of the hadronic final state:

$$W^2 = (p')^2 = (P + q)^2 = Q^2(1 - x)/x + M_P^2. \quad (2.12)$$

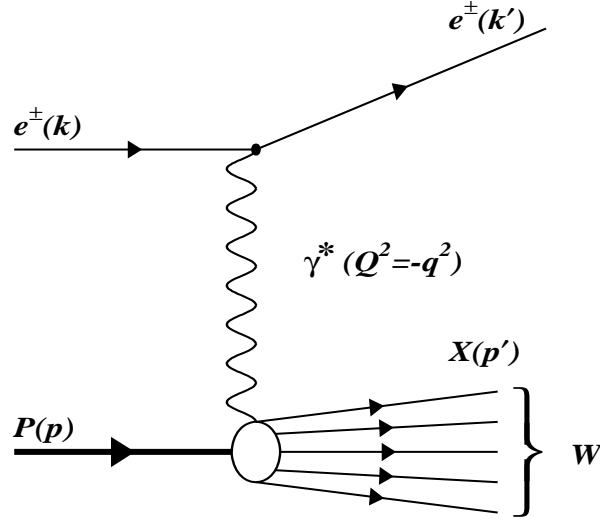


Figure 2.2: Schematic representation of inclusive electron proton scattering  $e^\pm p \rightarrow e^\pm X$  at low  $Q^2$  with the single photon exchange approximation. The four-momenta of the incoming and scattered lepton are  $k$  and  $k'$ , respectively. The four-momentum of the incident proton is  $p$  and  $p'$  denotes the four-momentum of the hadronic final state  $X$  with the invariant mass  $W$ .

The deep inelastic region is then defined by  $Q^2 > M_{proton}^2 \approx 1 \text{ GeV}^2$  and  $W^2 > M_{proton}^2$  requirement.

The  $Q^2$  values vary within the range  $0 < Q^2 < s$ , where

$$s = 2Pk = 4E_p E_e \quad (2.13)$$

denotes the energy in the center of mass system.

### 2.2.2 Cross Section in Born Approximation

To lowest QED order (Born Approximation) the DIS cross section calculation is based on separation between interactions of the virtual boson with the lepton and the proton which can be expressed in terms of corresponding tensors:

$$d\sigma \sim L_{\nu\mu} W^{\nu\mu}, \quad (2.14)$$

where  $L_{\nu\mu}$  is the leptonic tensor describing the interaction between electron and virtual photon. This part can be precisely calculated in QED, where the electron is treated as a point-like Dirac particle.

The  $W^{\nu\mu}$  parameterizes the hadronic current in terms of the metric tensor  $g_{\nu\mu}$ , four-momenta  $P$  and  $q$  and unknown scalar functions. Using Lorenz invariance and hadronic current conservation, this tensor can be reduced to two structure functions:

$$W^{\nu\mu} = W_1 \left( -g^{\nu\mu} + \frac{q^\nu q^\mu}{q^2} \right) + W_2 \frac{1}{M^2} \left( p^\nu - \frac{P \cdot q}{q^2} q^\nu \right) \left( p^\mu - \frac{P \cdot q}{q^2} q^\mu \right). \quad (2.15)$$

By including the photon flux factor and the phase space factor for outgoing electron, one obtains the following double differential inclusive  $ep$  scattering cross section, neglecting the mass of the electron:

$$\left( \frac{d^2\sigma}{dydQ^2} \right)_{ep \rightarrow eX} = \frac{4\pi\alpha^2}{sQ^4} \left( Q^2 \cdot MW_1 + \frac{1}{ys} \left[ (1-y)s^2 - M^2Q^2 \right] (\nu W_2) \right). \quad (2.16)$$

After involving the functional determinant  $\frac{EE'}{\pi} \frac{d^2\sigma}{dQ^2 d\nu} = \frac{d^2\sigma}{dE' d\Omega}$ , Eq. 2.16 yields the famous Rosenbluth formula (see Eq. 2.3).

Since the interaction between electron and proton is defined by the exchange of the virtual photon, its polarization states must be taken into account. One can consider the total cross section of the  $ep$  scattering as a sum over total absorption cross sections for transversely and longitudinally polarized virtual photons

$$\sigma^{tot} = \sum_{\lambda} \frac{4\pi\alpha^2}{K} \epsilon_{\lambda}^{\mu*} \epsilon_{\lambda}^{\nu} W_{\nu\mu}, \quad (2.17)$$

where  $K$  is a photon flux factor<sup>1</sup> and  $\epsilon_{\lambda}^{\mu}$  are the polarization vectors of virtual photons specified by the helicity  $\lambda$  [24]. The helicity  $\lambda = \pm 1$  and  $\lambda = 0$  correspond to the longitudinally and transversely polarized virtual photon, respectively. And the double differential DIS cross section can be written as

$$\frac{d^2\sigma}{dE' d\Omega} = \Gamma (\sigma_T + \epsilon\sigma_L), \quad (2.18)$$

where

$$\sigma_T = \frac{4\pi\alpha^2}{K} W_1 \quad (2.19)$$

and

$$\sigma_L = \frac{4\pi\alpha^2}{K} W_L = \frac{4\pi\alpha^2}{K} \left[ \left( 1 - \frac{\nu^2}{q^2} \right) W_2 - W_1 \right] \quad (2.20)$$

are the cross sections of the interaction with the transverse and longitudinally polarized virtual photon.  $\Gamma$  is the virtual photon flux defined as

$$\Gamma = \frac{K}{4\pi\alpha^2} \frac{2E'}{\epsilon q^2 (\epsilon - 1)}, \quad (2.21)$$

where  $\epsilon = [1 + 2(1 - \nu^2/q^2) \tan^2(\theta_e/2)]^{-1}$  defines the photon polarization.

A function often used to measure the behavior of the probability of longitudinal photon absorption to the transversal one is defined by the ratio

$$R(\nu, Q^2) = \frac{\sigma_L(\nu, Q^2)}{\sigma_T(\nu, Q^2)} = \frac{W_L(\nu, Q^2)}{W_1(\nu, Q^2)} = \frac{F_L(\nu, Q^2)}{F_2(\nu, Q^2) - F_L(\nu, Q^2)}, \quad (2.22)$$

where the denominator in the last term originates from the following relation:  $F_L(\nu, Q^2) = 2xF_1(\nu, Q^2) - F_2(\nu, Q^2)$ .

---

<sup>1</sup>The definition of the flux factor is somewhat arbitrary. Here, the virtual photon flux is defined as in [23]. It involves the constraint on the total  $\gamma^*p$  cross section in the photoproduction limit ( $Q^2 \rightarrow 0$ ) to coincide with the one of the real photon exchange, i.e.  $\lim_{Q^2 \rightarrow 0} \sigma_{\gamma^*p}^{tot}(Q^2, \nu) = \sigma_{\gamma p}^{tot}(\nu)$  must be satisfied.

### 2.2.3 Quark Parton Model

Feynman proposed a model, where the proton consists of quasi-free point-like partons in the frame, where the proton is moving with infinite momentum. The cross section of deep inelastic  $ep$  scattering is then the incoherent sum over all electron-parton scattering cross sections:

$$\left(\frac{d\sigma}{dx dQ^2}\right)_{ep \rightarrow eX} = \sum_i \int dx e_i^2 q_i(x) \left(\frac{d\sigma}{dx dQ^2}\right)_{eq_i \rightarrow eq_i}, \quad (2.23)$$

where  $q_i(x)$  is the parton momentum density of the parton  $i$  with the charge  $e_i$  inside the proton. The four momentum transfer  $Q^2$  and  $x$  correspond to the mass of the virtual photon and the fraction of the proton momentum carried by the parton which is hit by the exchanged virtual photon, respectively.

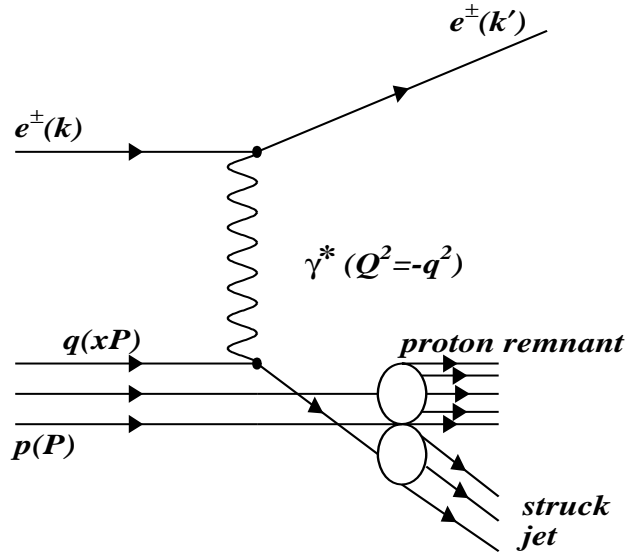


Figure 2.3: Schematic representation of deep inelastic  $ep$  scattering in the Quark Parton Model. The virtual photon interacts with a free, point-like charged parton carrying a fraction  $xP$  of the proton momentum. The interaction proceeds with hadronization resulting in a “proton remnant” jet and a “struck jet” emitted along the direction of the struck quark.

The first deep inelastic scattering experiments [25] on the measurement of  $R = \sigma_L/\sigma_T$  showed that the Callan-Gross relation (Eq. 2.9) holds. The partons of the proton are Dirac particles, since

$$\sigma_T = 0 \quad \text{for spin-0 partons,} \quad (2.24)$$

$$\sigma_L = 0 \quad \text{for spin-1/2 partons.} \quad (2.25)$$

Study of quantum numbers of the Feynman’s partons allowed to identify them with Gell-Man’s and Zweig’s quarks (see Section 2.1).

In the naive Quark-Parton-Model the proton structure functions can be expressed as a sum of the (anti)quarks momentum density distributions  $q_i(x)$  weighted with their electric charge  $e_i$  squared

$$F_2 = \sum_i e_i^2 x [q_i(x) + \bar{q}_i(x)]. \quad (2.26)$$

Since the proton consists of two  $u$  and one  $d$  valence quarks, the following counting rules must be satisfied:

$$\int_0^1 dx (u(x) - \bar{u}(x)) = 2, \quad \int_0^1 dx (d(x) - \bar{d}(x)) = 1. \quad (2.27)$$

Various combinations of structure functions in charged lepton and in neutrino-nucleon scattering were intensively studied and a number of counting rules was postulated. For example, the difference of the structure function  $F_2$  measured in neutrino- and antineutrino-proton scattering obeys the ‘‘Adler’’ sum rule:

$$\int_0^1 \frac{dx}{2x} [F_2^{\bar{\nu}p} - F_2^{\nu p}] = 2 \quad (2.28)$$

which describes the difference of the valence quarks in the proton. The analog of the ‘‘Adler’’ counting rule in case of charged lepton-proton neutral current scattering is provided by the ‘‘Gottfried’’ sum rule:

$$\int_0^1 \frac{dx}{2x} [F_2^{\mu p} - F_2^{\mu n}] = 1/3 + 2/3 \int_0^1 dx [\bar{u}(x) - \bar{d}(x)] = 1/3 \quad (2.29)$$

which describes the asymmetry between the sea quarks  $\bar{u}$  and  $\bar{d}$  by deviation of the integral from its predicted value of 1/3.

Conservation of the total proton momentum leads to the expectation

$$\sum_i \int_0^1 dx x [q_i(x) + \bar{q}_i(x)] = 1. \quad (2.30)$$

Yet, a surprising result was that integration over the experimental data on  $F_2^{\nu p, \nu n}(x)$  gave  $\epsilon \approx 0.5$  [26]. Thus, a substantial part of the proton’s momentum is carried by the neutral constituents. These are the gluons of QCD.

## 2.2.4 Quantum Chromodynamics and DIS

Violation of the scaling hypothesis observed by all lepton and neutrino nucleon scattering experiments was consistent with the presence of gluons inside the proton. The

simple Quark Model could not explain the following paradoxes: inability to observe free quarks, existence of only  $q\bar{q}$  and  $qqq$  type bound states and the violation of the Fermi statistics by the  $\Delta^{++}$  state with  $uuu$  structure. The last point was resolved by the introduction of a new quantum number which later was called “color” [27]. It was postulated that each quark had one of 3 colors: red, blue or green and the observed hadrons were color singlet states. The interaction between quarks happened by color exchange mediated by gluons. Consequently, gluons carried combinations of color mixing, such as  $rg$ ,  $gb$ , and so on. Since the physical observables must be colorless, neither quarks, nor gluons are observed. This effect was called “confinement” and up to now cannot be fully explained by the theory.

The naive QPM was modified in order to describe the more complex proton structure and interactions. All the phenomena mentioned above were explained in terms of Quantum Chromodynamics, the theory of strong interactions between quarks by the gluon exchange<sup>2</sup>. These interactions are similar to the Coulomb ones, yet color plays the role of the charge. Since the gluons are also “colored”, contrary to virtual photons, they may interact with each other. The quarks obey SU(3) internal “color” symmetry, which gives rise to eight additional self-coupling zero mass vector bosons, namely gluons. Due to self-coupling of the gluons, contrary to QED, where a screening effect makes the  $\alpha$  coupling constant decreasing with increasing  $Q^2$ , the strong coupling constant  $\alpha_s$  vanishes logarithmically with increasing  $Q^2$  because of anti-screening effect. This behavior is called “asymptotic freedom”. In the leading order approximation the strong coupling constant  $\alpha_s$  is given by the equation:

$$\alpha_s(Q^2) = \frac{4\pi}{\beta_0 \ln \frac{Q^2}{\Lambda^2}} \quad \text{with} \quad \beta_0 = 11 - \frac{2}{3}n_f, \quad (2.31)$$

where  $n_f$  is the number of quark flavors and  $\Lambda$  characterizes the energy scale at which the strong coupling constant becomes large. This is also a sign of the breakdown of the perturbative calculations at  $Q^2 \approx \Lambda^2$ . The value of  $\Lambda$  can be deduced from experimentally measurable  $\alpha_s$ . The latter value is, by convention, represented at  $Q^2 = M_Z^2$  where  $M_Z$  is the mass of the  $Z_0$  boson. The world average value is  $\alpha_s(M_Z^2) = 0.118 \pm 0.003$  [30]. The corresponding  $\Lambda$  value is about 200 MeV for  $n_f=4$ .

According to the QCD *factorization theorem* [31] the structure functions can be expressed as a convolution of coefficient functions  $C_a^{V,i}$ , given by pQCD for a particular exchanged boson  $V$ , parton  $i$  and a structure function  $a$  with parton distributions  $f_{i/h}$ . These are specific to the hadron  $h$  but universal for  $V$  and  $a$  as schematically presented in Fig. 2.4. The factorization theorem allows to write the following equation for structure function  $F_2$ :

$$F_2^{V,h}(x, Q^2) = \sum_{i=f,\bar{f},g} \int_x^1 dz C_2^{V,i} \left( \frac{x}{z}, \frac{Q^2}{\mu^2}, \frac{\mu_F^2}{\mu^2} \alpha_s(\mu^2) \right) f_{i/h}(z, \mu_F, \mu^2), \quad (2.32)$$

---

<sup>2</sup>A review about the present status of the QCD as the asymptotically free field theory of quark-gluon interactions and its foundation can be found in [28] and [29], respectively.

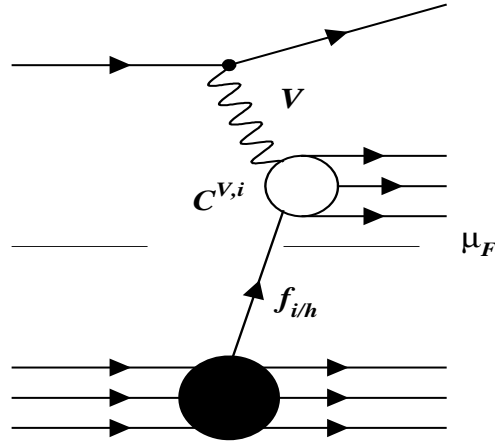


Figure 2.4: Schematic representation of the factorization theorem. Explanation see in the text.

where the summation is performed over all hadron constituents (quarks, antiquarks, gluons). The structure function  $F_2$  is composed of two components, namely a probability density  $f_{i/h}$  of finding a parton with fractional proton momentum  $z$  in the proton and a coefficient term  $C_2^{V,i}(x/z)$ . The last term is computable and describes a “history” of the interacting parton, i.e. evolving from radiative process off the initial parton. There are two mass scales in the theorem. The renormalization scale  $\mu$  defines the separation between the finite and the divergent contributions in the renormalization procedure. The factorization scale  $\mu_F$  defines the boundary between the perturbative and non-perturbative regions. Both scales  $\mu$  and  $\mu_F$  are arbitrary and serve to absorb infrared (ultraviolet) divergences in pQCD. One has certain freedom to choose a renormalization scheme. The most convenient scheme in deep-inelastic scattering is the DIS scheme in which the structure function  $F_2$  is given by the parton model formula 2.26 also in NLO. All orders of perturbation theory are absorbed into the distribution functions  $q$  and  $\bar{q}$  for  $\mu = \mu_F = Q$ . For theoretical calculations one often uses the modified minimal subtraction scheme ( $\overline{MS}$ ) which follows the idea of dimensional regularization by t’ Hooft and Veltman [32]. Here, only the divergent part of the coefficient functions is absorbed into the renormalized quark distributions for  $\mu = \mu_F$ .

Another important outcome of the factorization theorem is the possibility to evolve the parton densities from a certain  $Q_0^2$  to any other  $Q^2$  value. Since  $F_2$  is a measurable quantity and therefore can not depend on  $\mu_F$ , the following equation holds:

$$\mu_F^2 \frac{dF_2(x, Q^2)}{d\mu_F^2} = 0. \quad (2.33)$$

This leads to a set of integro-differential equations named DGLAP [33] after Dokshitzer, Gribov, Lipatov, Altarelli and Parisi. In terms of gluon ( $g(x, Q^2)$ ), singlet

( $\Sigma(x, Q^2) = \sum_i [q_i(x, Q^2) + \bar{q}_i(x, Q^2)]$ ) and nonsinglet ( $q^{NS}(x, Q^2) = \sum_i [q_i(x, Q^2) - \bar{q}_i(x, Q^2)]$ ) density functions, the evolution equations can be written as:

$$\begin{aligned} \frac{d\Sigma(x, Q^2)}{d \ln Q^2} &= \frac{\alpha_s(Q^2)}{2\pi} \int_x^1 \frac{dy}{y} [\Sigma(y, Q^2) P_{qq}(x/y) + g(y, Q^2) P_{qg}(x/y)], \\ \frac{dg(x, Q^2)}{d \ln Q^2} &= \frac{\alpha_s(Q^2)}{2\pi} \int_x^1 \frac{dy}{y} [\Sigma(y, Q^2) P_{gq}(x/y) + g(y, Q^2) P_{gg}(x/y)], \end{aligned} \quad (2.34)$$

for the coupled pair of singlet-gluon equations, and as:

$$\frac{dq^{NS}(x, Q^2)}{d \ln Q^2} = \frac{\alpha_s(Q^2)}{2\pi} \int_x^1 \frac{dy}{y} q^{NS}(y, Q^2) P_{qq}(x/y) \quad (2.35)$$

for the nonsinglet distributions. Here the splitting functions  $P_{ij}(z)$  represent the probability of a parton  $j$  emitting a parton  $i$  with momentum fraction  $z$  of the parent parton, when the scale changes from  $Q^2$  to  $Q^2 + d \ln Q^2$ . The splitting functions are calculable by perturbative expansion:

$$P_{ij}(z, \alpha_s(Q^2)) = \frac{\alpha_s}{2\pi} P_{ij}^{(0)}(z) + \left(\frac{\alpha_s}{2\pi}\right)^2 P_{ij}^{(1)}(z) + \dots \quad (2.36)$$

At the moment the splitting functions are calculated up to next to next to leading order of the pQCD [34].

Summarizing the information given above, one can consider the deep inelastic  $ep$  scattering process as an incoherent sum of the virtual photon-parton interaction cross sections. The double differential cross section at low  $Q^2$  is defined by two structure functions  $F_2(x, Q^2)$  and  $F_L(x, Q^2)$ :

$$\frac{d^2\sigma}{dx dQ^2} = \kappa \left( F_2(x, Q^2) - \frac{y^2}{Y_+} F_L(x, Q^2) \right), \quad Y_+ = 1 + (1-y)^2, \quad \kappa = \frac{2\pi\alpha^2}{Q^4 x} Y_+. \quad (2.37)$$

In the DIS renormalization scheme, the structure function  $F_2$  is given to all orders of perturbative theory by  $F_2(x, Q^2) = x \sum_i e_i^2 [q_i(x, Q^2) + \bar{q}_i(x, Q^2)]$ , where the parton momentum density distribution functions evolve according to DGLAP Eqs. 2.34.

The longitudinal structure function  $F_L(x, Q^2)$  differs from zero due to QCD radiative corrections proportional to  $\alpha_s$  [28]:

$$\begin{aligned} F_L(x, Q^2) &= x \sum_{i=f, \bar{f}} e_f^2 \int_x^1 \frac{dz}{z} f_i(z, Q^2) \left\{ \frac{\alpha_s}{2\pi} \left[ 2C_F \frac{x}{z} \right] + \dots \right\} \\ &+ x \sum_{i=f, \bar{f}} e_f^2 \int_x^1 \frac{dz}{z} g(z, Q^2) \left\{ \frac{\alpha_s}{2\pi} \left[ 4T_R \left( 1 - \frac{x}{z} \right) \right] + \dots \right\}, \end{aligned} \quad (2.38)$$

where  $C_F = 4/3$  and  $T_R = 1/2$ .

# Chapter 3

## The H1 Detector at HERA

In this chapter the *Hadron-Elektron-Ring-Anlage* HERA, the first  $ep$  collider in the world, is introduced in Section 3.1. The H1 detector and its major components as well as their role in the analysis are described in Section 3.2. The standard kinematic reconstruction methods used in the present analysis are explained in Section 3.3. The chapter continues with a sketch of event simulation programs (Section 3.4) and concludes with the presentation of data used in this work.

### 3.1 The HERA Accelerator

HERA represents an important step in the development of the facilities for the study of the matter structure. It comprises a chain of preaccelerators, DESY-II ( $e^\pm$ ), DESY-III ( $p$ ) and PETRA are used as boosters. HERA consists of two independent accelerator storage rings accommodated in a 6.3 km long tunnel where 820 GeV protons collide with 27.6 GeV electrons. Since summer 1998 the proton energy is 920 GeV. A schematic view of the HERA machine together with the injection system is shown in Fig. 3.1. PETRA accelerates and stores electrons up to 12 GeV and protons up to 40 GeV. The electron beam is then injected into HERA and guided by a warm magnet system of 0.165 T, while protons are injected into a ring with superconducting magnets of 4.68 T. The HERA accelerator was designed for 210 circulating bunches with 760  $\mu\text{A}$  protons and 290  $\mu\text{A}$  electrons each resulting in bunch crossing intervals of 96 ns corresponding to a rate of 10.4 MHz (see Table 3.1). The design luminosity was  $1.5 \times 10^{31} \text{ cm}^{-2}\text{s}^{-1}$ . Since 1994, HERA operates with a positron beam<sup>1</sup>. The lifetime of positrons is longer than that of electrons due to repelling the remaining (positively charged) beam gas ions reducing the beam gas interactions and thus the loss of particles. Two big detectors (H1 and ZEUS) are operated at HERA using its  $ep$  colliding mode. One of them, the H1 detector, will be described in the next section.

---

<sup>1</sup>Since the DIS cross section at low  $Q^2$  is nearly independent of the lepton beam charge, in the following and throughout this thesis the incident and scattered lepton will be referred to as electrons.

	Design		1997		units
	<i>p</i> -ring	<i>e</i> -ring	<i>p</i> -ring	<i>e</i> -ring	
Nominal energy	820	30	820	27.6	GeV
Number of bunches	210	210	175+6	175+14	
<Current>	159	58	74	28	mA
$\sigma_x/\sigma_y$ at I.P.	0.29/0.7	0.26/0.02	0.21/0.04		mm
$\sigma_z$	110	8.0	115		mm
Peak Luminosity	$1.5 \times 10^{31}$		$1.01 \times 10^{31}$		$\text{cm}^{-2}\text{s}^{-1}$
Integrated Luminosity	50		34		$\text{pb}^{-1}/\text{year}$

Table 3.1: HERA design parameters (from [35]) and its performance in the year 1997.  $\sigma_{x,y,z}$  stand for the  $x$ ,  $y$  and  $z$  spread of the beam at the interaction point (I.P.).

## 3.2 Detector Overview

The H1 detector is a general purpose apparatus designed for the investigation of high-energy interactions of electrons and protons at HERA. In the design of the H1 detector prime attention has been given to the clean identification of electrons and to their energy measurement. The sketch of the H1 detector is illustrated in Fig. 3.2.

The H1 detector is a nearly hermetic apparatus located concentrically around the beam pipe. Its acceptance for final state particles is limited only by the forward and backward beam pipe holes. Due to the imbalance in the energy of the colliding beams most of the scattered particles are boosted in the proton direction. Therefore, the detector is asymmetric and better instrumented in the outgoing proton direction, which defines, by convention, the positive  $z$  direction of the H1 coordinate system. The polar angle is defined with respect to this direction. Therefore, the components of the detector situated on the positive side from the interaction point are referred to as “forward” and those on the negative side as “backward”. The components placed around the interaction point are called “central”.

The major goal of this experiment is to measure precisely the angles and energies of the final state particles as well as to identify the scattered electron. To facilitate this the H1 detector is composed of a central and forward tracking system surrounded by liquid argon (LAr) electromagnetic and hadronic calorimeters. The backward part of the detector is supplemented by the backward drift chamber (BDC), the electromagnetic and hadronic Spaghetti calorimeter (SpaCal) and a new backward silicon tracker (BST). A superconducting cylindrical coil with a diameter of 6 m and a length of 5.75 m provides a uniform magnetic field of 1.15 T. The iron return yoke of the magnet is filled with limited streamer tubes surrounding the whole detector, which serves for measuring the tails of hadronic showers and the muon tracks.

This thesis concerns a low  $Q^2$  deep inelastic scattering analysis, therefore a special focus is put on the description of the backward part of the detector. The description of the BST which is the main detector for this work will be presented in the next chapter.

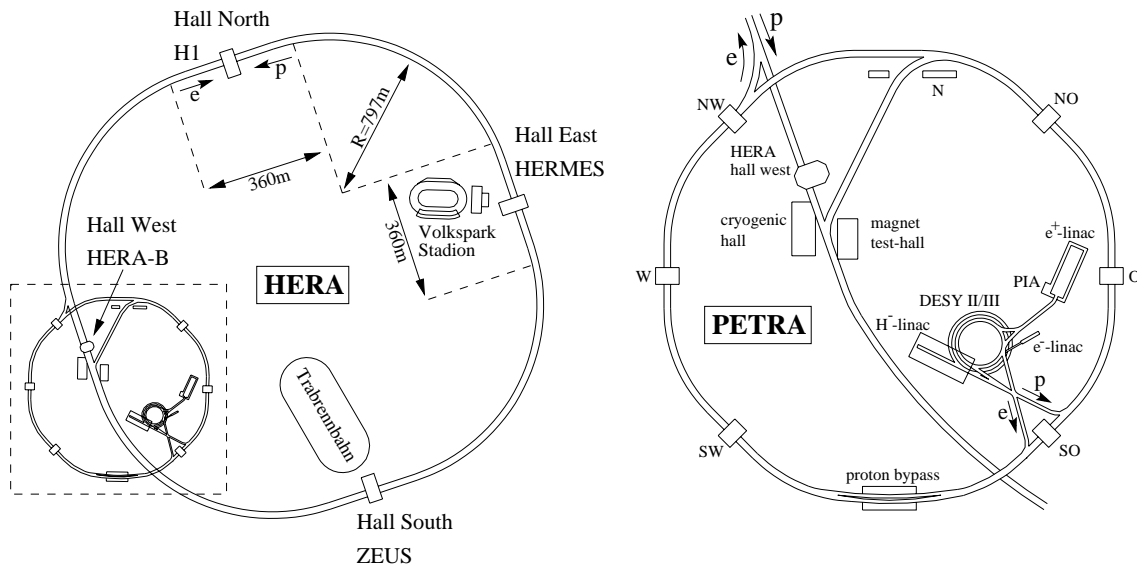


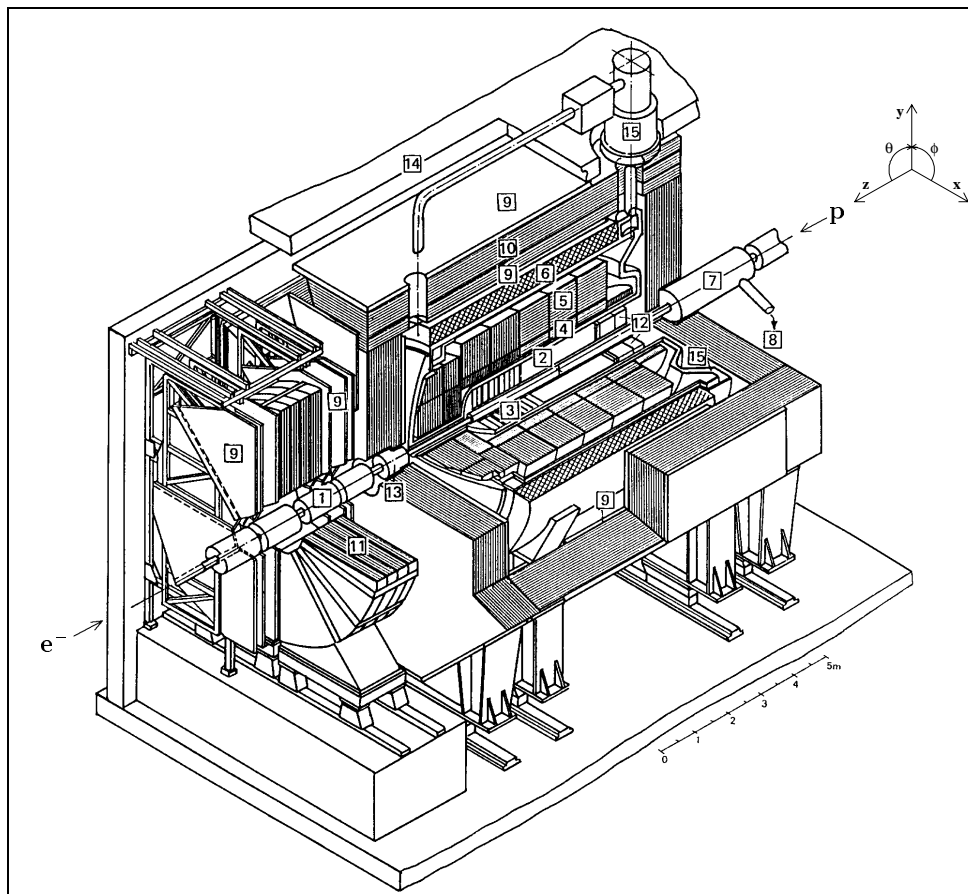
Figure 3.1: Schematic view of the  $ep$  storage ring HERA (left) together with the major experiments. The right figure presents a zoomed view of the HERA preaccelerator chain.

### 3.2.1 Luminosity System

The luminosity measurement is based on detecting the Bethe-Heitler bremsstrahlung events  $ep \rightarrow ep\gamma$ . Since this cross section is very large and well known, the luminosity can be calculated from the event rate taking into account the detector acceptance. The general view of the luminosity system is shown in Fig. 3.3. The luminosity system serves several purposes [36]:

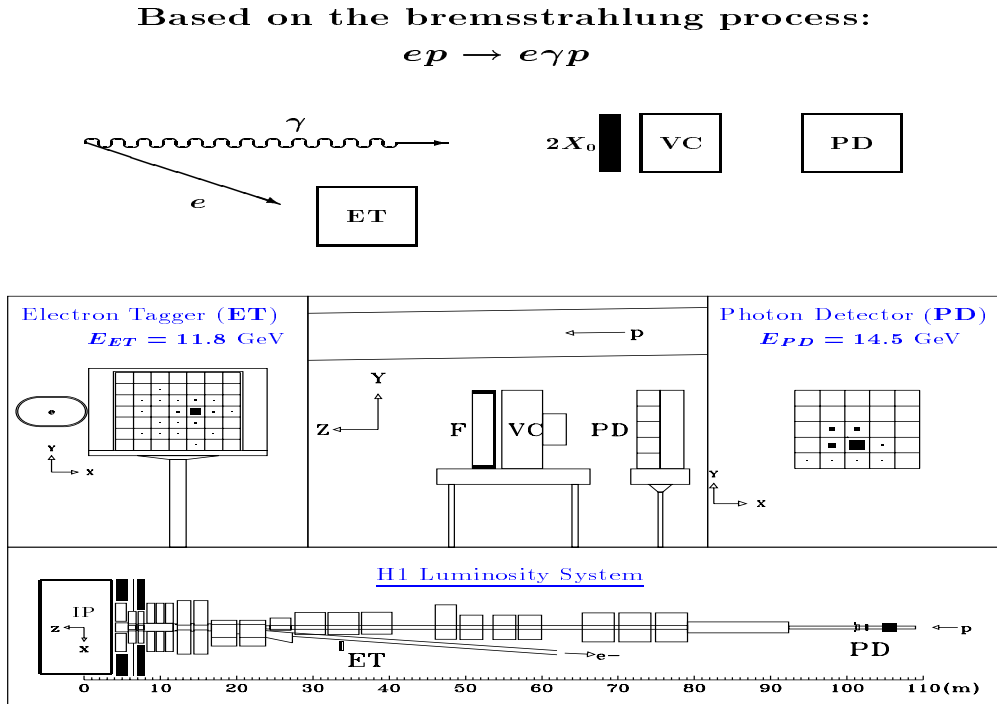
- online luminosity measurement by the *coincidence* method when the  $e$  and  $\gamma$  in the final state are simultaneously detected;
- offline luminosity measurement by the *single-photon* method which counts the rate with the photon energy above a certain threshold;
- electron beam monitoring for the HERA machine;
- energy measurement for electrons scattered at  $Q^2 < 0.01 \text{ GeV}^2$  (tagging of photoproduction events) using the photon detector as a veto (see Section 6.4);
- measurement of photons from initial state radiation in DIS.

The luminosity system comprises two small electromagnetic calorimeters, the electron tagger (ET) and the photon detector (PD), situated in the HERA tunnel at  $z$  positions of  $-34.4 \text{ m}$  and  $-102.9 \text{ m}$ , respectively. The ET consists of  $7 \times 7$  cells covering a total area of  $154 \times 154 \text{ mm}^2$ . The electrons scattered with energy between 10



- |  |   |
|--|---|
| <b>1</b> Beam pipe and beam magnets      | <b>9</b> Muon chambers                  |
| <b>2</b> Central tracking device         | <b>10</b> Instrumented iron yoke        |
| <b>3</b> Forward tracking device         | <b>11</b> Forward muon toroid           |
| <b>4</b> Electromagnetic LAr calorimeter | <b>12</b> Backward calorimeter (SpaCal) |
| <b>5</b> Hadronic LAr calorimeter        | <b>13</b> PLUG calorimeter              |
| <b>6</b> Superconducting coil (1.15 T)   | <b>14</b> Concrete shielding            |
| <b>7</b> Compensating magnet             | <b>15</b> Liquid argon cryostat         |
| <b>8</b> Helium supply for <b>7</b>      |   |

Figure 3.2: 3D sketch of the H1 detector.



and 20 GeV are deflected by the beam optics, pass an exit window at  $z=-27.3$  m and hit the ET. The angular acceptance of the ET is about 5 mrad. The PD consists of  $5 \times 5$  cells covering a total area of  $100 \times 100$  mm<sup>2</sup>. The photons leave the proton beam pipe through a window at  $z=-92.3$  m, where the beam pipe bends upwards, and hit the PD. The angular acceptance of the PD amounts to about 0.45 mrad.

### 3.2.2 Track Detectors

The H1 tracking system has been constructed in order to provide simultaneous track triggering, reconstruction, momentum measurement of charged particles and particle identification for the event topology particular to HERA  $ep$  collisions. As was mentioned, the geometry of the H1 detector is asymmetric since most of the particles are boosted into forward direction. Consequently, in order to maintain good efficiency for triggering and reconstruction over the whole solid angle, the tracking system was divided into two mechanically distinct detector modules, the central tracker (CTD) and forward tracker (FTD).

The CTD comprises 6 coaxial tracking chambers in the region of  $-1.5 < z < 2.5$  m. It is divided in an inner and a similar outer part. Next to the beam pipe the central inner proportional chamber (CIP) is situated. It consists of two double layers located concentrically around the beam pipe. Each layer is segmented into 480 pads which collect the charge induced by the crossing charged particles. The CIP is surrounded by

the central inner z-drift chamber (CIZ). The CIZ is optimized for the exact measurement of the z-coordinate of the track. It comprises 16 rings of polygonal shaped drift cells with 4 sense wires oriented perpendicular to the beam axis. The CIP and the CIZ supplement the central inner jet chamber (CJC1) which has wires oriented parallel to the beam axis. The outer part of the CTD consists of the central outer proportional chamber (COP), the central outer z-chamber (COZ) and the outer central jet chamber (CJC2). The CIP and COP provide a fast timing signal used to distinguish successive beam crossings on the first trigger level. The design of the CJC1 and CJC2 is optimized to measure tracks in the  $r - \phi$  plane. The drift cells in the chambers are inclined with respect to the radial direction by about  $30^\circ$ , such that in the presence of the magnetic field the ionization electrons drift approximately perpendicular to it. The resolution of the  $z$  vertex position and the polar angle measurement are substantially improved by using CIZ and COZ information. A special combined fit-reconstruction procedure [37] yields a  $z$  vertex position resolution of about 2 mm and a track  $\theta$  measurement accuracy of about 1 mrad.

The forward tracking detectors consist of three supermodules. Each supermodule comprises three different orientations of planar wire drift chambers for accurate  $\theta$  measurement, a multiwire proportional chamber (FWPC) for fast triggering, a passive transition radiator and a radial wire drift chamber providing accurate  $r\phi$  information. The FTD accepts particles within the polar angle range  $5^\circ \leq \theta \leq 25^\circ$ . A combination of FWPC hits with the hits of the COP pads and those of the CIP builds a “ray” trigger condition used to select events with tracks originating from the interaction region.

### 3.2.3 Liquid Argon Calorimeter

The liquid argon calorimeter (LAr) was designed to provide clear identification and a precise energy measurement of electrons and particles from the hadronic final state with high density in the central and forward detector regions. In order to meet these requirements the calorimeter is constructed with high segmentation and placed inside the large coil. This minimized the amount of dead material in front of the electromagnetic calorimeter and the overall size and weight.

The liquid argon calorimeter covers the angular range between  $4^\circ$  and  $153^\circ$ . It consists of electromagnetic and hadronic parts segmented in eight self supporting “wheels” as shown in Fig. 3.4, each of them segmented in  $\phi$  into eight stacks or octants.

The electromagnetic part of the LAr is made of Pb absorber plates and has a total thickness varying between 20 and 30 radiation lengths for electrons representing 1.0-1.4 interaction lengths for hadrons. The hadronic stacks are fabricated of stainless steel absorber plates and have a thickness of 5 to 8 interaction lengths. A tail catcher system (TC) surrounds the LAr and provides a rough reconstruction of the hadronic shower tails using streamer tubes that instrument the iron yoke.

The energy resolution of the electromagnetic calorimeter is  $\sigma/E \approx 10\%/\sqrt{E} \oplus 1\%$ . The hadronic calorimeter has an energy resolution of  $\sigma/E \approx 50\%/\sqrt{E} \oplus 2\%$ . In

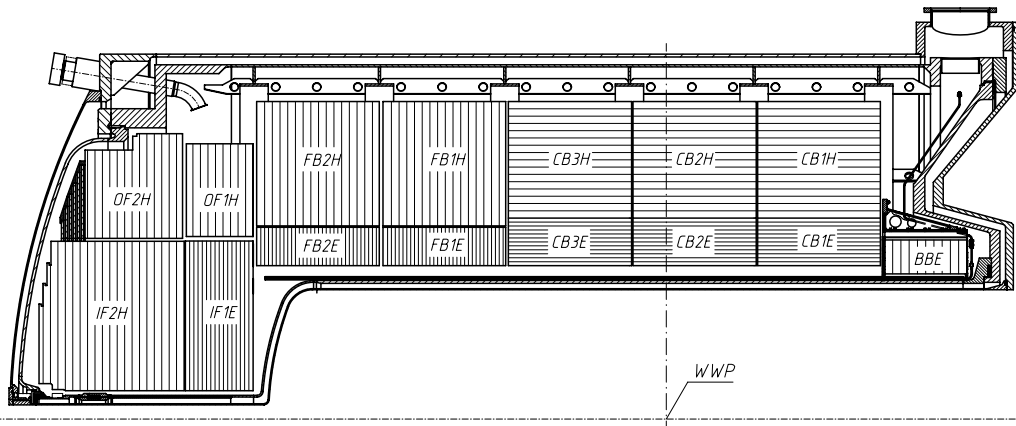


Figure 3.4: Schematic view of the LAr calorimeters.

LAr parameters	electromagnetic part	hadronic part
Granularity (number of channels) Depth	10 to 100 cm <sup>2</sup> (30784) 20 to 30 X <sub>0</sub>	50 to 2000 cm <sup>2</sup> (13568) 4.7 to 7 λ <sub>abs</sub>
Resolution $\sigma(E_{e,h})/E_{e,h}$	10%/√E <sub>e</sub> ⊕ 1%	50%/√E <sub>h</sub> ⊕ 2%
Stability of electronic calibration	≤ 0.2% over one month	
LAr purity (decrease of signal)	≤ 0.2% over one year	
Noise per channel	10 to 30 MeV	
Angular coverage - dead channels	5° < θ < 154°	< 0.3%

Table 3.2: Summary of LAr calorimeter technical parameters.

Table 3.2 important parameters of the LAr calorimeter are summarized. The LAr calorimeter is non-compensating. Therefore, a special software weighting technique [38] is applied to get the proper hadronic energy scale. Both the electromagnetic and hadronic absolute energy scales were initially calibrated up to a few hundred GeV during test beam exposures at the CERN-SPS [39, 40] and later refined using H1 data (see Section 5.2). Use of the  $P_t$  balance between the scattered electron and the hadronic final state particles led to a hadronic absolute energy scale accuracy of 2% as will be described in Section 5.2.1. Presently, the absolute electromagnetic energy scale of the LAr is known with  $\sim 1\%$  accuracy verified by various calibration methods [41].

### 3.2.4 Backward Detectors

The measurement of the proton structure function at very small values of Bjorken  $x$  has become an area of key interest at HERA. This requires efficient electron identification and a precise measurement of the energy and polar angle of the electron scattered

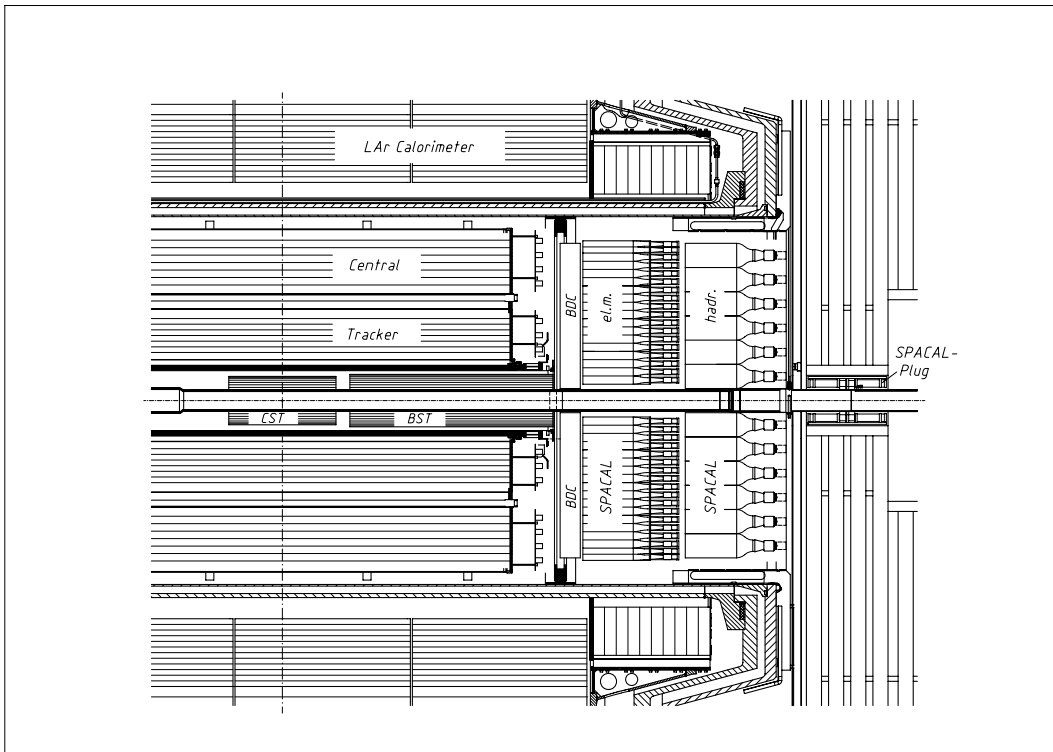


Figure 3.5: Schematic view of the backward part of the H1 detector.

into the backward region of the H1 detector. In order to improve the H1 instrumentation the collaboration exchanged its backward apparatus completely. The data of the year 1997, described here, were the first taken with the completed new backward part of the detector consisting of three elements schematically sketched in Fig. 3.5: a lead/scintillating-fiber calorimeter (SpaCal) [42], a planar drift chamber (BDC) [43] and a silicon tracker (BST) [44].

- The **SpaCal calorimeter** is located in the  $z$  range between -151 cm and -244 cm. It consists of electromagnetic and hadronic sections with an outer radius of 80 cm and the inner one of 5.7 cm. The angular coverage of the hadronic calorimeter near the pipe is extended by an additional backward plug calorimeter.

The electromagnetic calorimeter is fabricated sandwichlike using grooved lead plates and scintillating fibers with 0.5 mm diameter. It is composed of 1192 cells, each has an active volume of  $4 \times 4 \times 25 \text{ cm}^3$ . This corresponds to 27.5 radiation lengths ensuring full containment of the deposited electromagnetic energy. The light signal from the fibers is transmitted through a light mixer to photomultiplier tubes (PMT). The scintillation light is then converted into an electric pulse with an amplification (gain) of  $\approx 10^4$ . Due to an extremely low noise level ( $\approx 3 \text{ MeV}$ ) the low trigger thresholds of 1-3 GeV are determined by background rates and not by electronics limitations. Furthermore, a reliable reconstruction of small

Acceptance	$153^\circ \leq \theta_e \leq 177.8^\circ$
Energy Resolution (EM) $\sigma_E/E$ , $E$ in GeV	$7.5\%/\sqrt{E} \oplus 2\%$
Energy Scale Uncertainty (EM)	0.3% at 27.5 GeV
Energy Resolution (Hadrons) $\sigma_E/E$ , $E$ in GeV	$\sim 30\%/\sqrt{E}$
Spatial Resolution $\sigma_r$	3.4 mm
Time Resolution $\Delta t$	$\leq 1$ ns
Noise level $\Delta E$	$\leq 3$ MeV

Table 3.3: Performance parameters of the SpaCal calorimeter.

energy deposits is enabled. Because of a very fast time response ( $\leq 1$  ns) the SpaCal allows to suppress the beam gas background.

The electromagnetic SpaCal has a very good homogeneity and high energy resolution of  $7\%/\sqrt{E} \oplus 1\%$ . The good spatial resolution of  $3.8/\sqrt{E} \oplus 3$  mm provides the important additional possibility to identify the scattered electron by its transverse cluster profile.

The hadronic section of the SpaCal consists of 136 cells with a cross section of  $12 \times 12$  cm<sup>3</sup> which roughly corresponds to the lateral dimensions of hadronic showers. The active depth of the cells is limited to 25 cm due to constraints from the iron return yoke of the H1 magnet. Thus the hadronic section adds about one interaction length of material to the electromagnetic one, which provides also one interaction length. The hadronic energy resolution of the calorimeter is about  $30\%/\sqrt{E}$ .

- The **Backward Drift Chamber** has been designed to supplement the measurement of the scattered electron made by SpaCal with a track segment. It is mounted in front of SpaCal at a  $z$  position of -146 cm and covers the polar angle range between  $153^\circ$  and  $177.5^\circ$ . The BDC is subdivided into 8 octants consisting of 4 double layers of sense wires rotated by  $11.25^\circ$  to obtain a rough measurement of the azimuthal angle. To optimize the  $\theta$  measurement the signal wires are oriented perpendicular to the beam axis. Since the event rate rapidly increases with increasing of the polar angle of the scattered electron, the BDC has three regions with different cell sizes, in order to avoid a high occupancy of the signals at low radii. The acceptance of this analysis is limited to the region of the BDC with finer cell sizes of 1 cm what gives about 0.5 mrad angular resolution if no shower occurred in the material in front of the BDC.
- The **Backward Silicon Tracker** provides an exact measurement of the scattered electron angle at low  $Q^2$ . It supplements the event vertex determination at low  $y$  and at high  $y$ , i.e. in those kinematical regions where the final state particles escape the CTD acceptance. At high  $y$  the BST provides a substantial suppression of the neutral component of the photoproduction background by matching of a track with the SpaCal cluster.

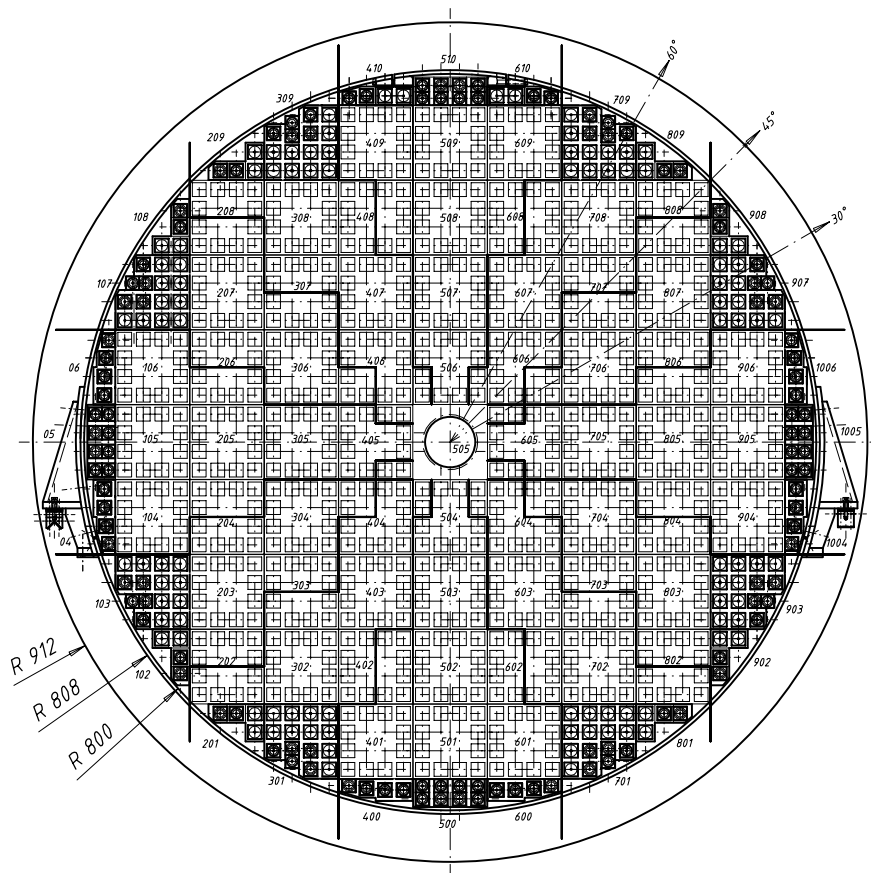


Figure 3.6: Schematic transverse view of the SpaCal electromagnetic calorimeter.

The BST, in its 1997 configuration, is a 4 plane silicon detector telescope arranged concentrically around the beam pipe which covers a polar angle range between  $171.5^\circ$  and  $176.5^\circ$ . It is described in detail in Chapter 4.

### 3.2.5 Trigger System

The H1 trigger system presently includes three levels of event filtering: L1, L2 and L4. An additional offline event selection is performed on level L5.

- The first trigger level L1 is a dead-time free system. It is synchronized to the HERA clock (10.4 MHz) and provides a trigger decision after  $2.5 \mu s$ . During this time the full information is stored in pipelines. There are up to 128 trigger conditions (subtriggers) composed as logical AND combinations of various trigger elements which represent different trigger signals coming from the detector components. The logical OR of the 128 subtriggers constitutes the L1 accept. Any L1 subtrigger rate can be downscaled in order to meet the readout bandwidth constraints. If a subtrigger condition is fulfilled, its “raw” bit is set. If the event

is selected after possible prescaling according to certain subtrigger, the “actual” trigger bit is set;

- L2 validates the L1 decision within 20  $\mu\text{s}$  using more detailed trigger data and more complicated algorithms (neural network and topological triggers). Upon a positive L2 trigger decision the readout of the event is started. The full digitized event information is collected and transferred to the trigger level L4 (presently bypassing the level L3);
- At L4, a processor farm consisting of 36 parallel processors acts asynchronously as a filter on the full data to reduce the logging volume. Additional background suppression is performed here, using reconstructed event information. About 20% of the events pass the L4 selection cuts. These are written on tape. For monitoring purposes, one out of 100 rejected events is written to a separate data file.

In the L5 level the full offline event reconstruction is performed. The events are classified in an analysis dependent way according to their physics properties. Unclassified events are rejected and the selected ones are written to a so-called Data Summary Tape (DST), which is the starting point for further physics analyses.

### 3.3 Kinematics Reconstruction

Experimental study of the double differential deep-inelastic scattering cross section requires a reconstruction of two kinematic variables (Eq. 2.37), usually taken to be  $Q^2$  and  $x$  or  $y$ . These three variables have a simple relation:

$$Q^2 = xys, \quad (3.1)$$

where  $s$  is the energy in the center of mass system,  $s \approx 4E_e E_p \approx 9 \cdot 10^4 \text{ GeV}^2$ . Due to the almost complete  $4\pi$  coverage of the H1 detector, the possibility to measure both leptonic and the hadronic final states is provided. Kinematics reconstruction determines their energies and the scattering angles which are defined with respect to the proton beam direction. Thus, one measures the four-vectors of the incoming ( $k$ ) and the scattered electron ( $k'$ ), of the incoming proton ( $p$ ) and of the outgoing hadrons ( $p'$ ) which are defined as follows:

$$k = \begin{pmatrix} E_e \\ 0 \\ 0 \\ -E_e \end{pmatrix} \quad k' = \begin{pmatrix} E'_e \\ E'_e \sin \theta \\ 0 \\ E'_e \cos \theta \end{pmatrix} \quad p = \begin{pmatrix} E_p \\ 0 \\ 0 \\ E_p \end{pmatrix} \quad p' = \begin{pmatrix} E_h \\ P_x^h \\ P_y^h \\ P_z^h \end{pmatrix}. \quad (3.2)$$

Hence, the kinematics determination is overconstrained which allows to use various combinations of these four-vectors to reconstruct the kinematic variables. This nice

feature gives not only the opportunity to cross check the quality of the reconstruction but permits also a flexible choice of the reconstruction methods according to their resolutions in the particular kinematical regions. Various aspects of the kinematics reconstruction at HERA were intensively studied [48].

Since the detector has a limited acceptance due to the holes for beam access, a loss of final state particles is unavoidable. Hence, variables used for kinematics reconstruction are to be preferred which are rather insensitive to these losses. One of such variables is the transverse momentum  $P_t$  since for particles lost in the beam pipe it is about zero. The  $P_t$  is suitable not only for kinematics reconstruction but also for calibration purposes (see Section 6.3.4) due to a natural constraint on the momentum conservation:

$$P_t^{had} + P_t^e = \sum_h E_h \sin \gamma_h + E_e' \sin \theta_e = 0, \quad (3.3)$$

where  $\theta_e$  and  $\gamma_h$  are the polar angles of the scattered electron and of a hadronic final state particle, respectively.

Another important quantity is the  $E - P_z$  variable defined as follows:

$$E - P_z = \Sigma + E_e' \cdot (1 - \cos \theta_e), \quad \text{with } \Sigma = \sum_h E_h \cdot (1 - \cos \gamma_h). \quad (3.4)$$

Here, the summation  $\sum_h$  is performed over the hadronic final state particles, and their masses are neglected. Due to the factor  $(1 - \cos \theta)$ , the  $E - P_z$  variable is insensitive to energy loss in forward direction but very sensitive to losses or noise in the backward part of the detector. Due to energy and longitudinal momentum conservation, one has the relation which is disturbed only by radiation and imperfect reconstruction:

$$E - P_z = 2E_e. \quad (3.5)$$

Relation 3.5 is utilized to suppress photoproduction background when the scattered electron escapes detection as well as initial state radiation when the radiated photon carries a substantial part of the  $E - P_z$ . Furthermore, as in the case of the  $P_t$  balance, the quantity  $E - P_z$  is used for calibration purposes.

Using  $P_t^{had}$  and  $\Sigma$  variables, it is possible to define a hadronic energy and angle via:

$$E_{jet} = \frac{P_{t,had}^2 + \Sigma^2}{2\Sigma}, \quad (3.6)$$

$$\tan \frac{\theta_h}{2} = \frac{\Sigma}{P_t^{had}}.$$

The latter corresponds to the polar scattering angle of the struck quark in the parton picture. Redundancy of the final state measurement permits to calculate the hadronic angle using the measurement of the scattered electron, denoted as  $\gamma_e$ :

$$\tan \frac{\gamma_e}{2} = \frac{y_e}{1 - y_e} \tan \frac{\theta_e}{2}. \quad (3.7)$$

Here,  $y_e$  is the inelasticity reconstructed with an “electron method” which is described next.

In the presented analysis four reconstruction methods have been used for particular reasons which are discussed briefly in the following:

1. The **Electron Method** is based on the measurement of the polar angle  $\theta_e$  and the energy  $E'_e$  of the scattered electron. In this case the event kinematics can be reconstructed as follows:

$$y_e = 1 - \frac{E'_e}{E_e} \sin^2 \frac{\theta_e}{2}, \quad Q_e^2 = \frac{E_e'^2 \sin^2 \theta_e}{1 - y_e}, \quad x_e = \frac{Q_e^2}{s y_e}. \quad (3.8)$$

This method relies on the incident energy of the electron  $E_e$  and, hence, is affected by photon bremsstrahlung off the incoming electron. This affects the kinematics reconstruction and has to be corrected for.

The reconstruction accuracy in  $Q^2$ ,  $x$  and  $y$  depends on the energy and the angle precisions as [49]:

$$\begin{aligned} \frac{\delta Q^2}{Q^2} &= \frac{\delta E_e}{E_e} \oplus \tan\left(\frac{\theta}{2}\right) \cdot \delta\theta, \\ \frac{\delta x}{x} &= \frac{1}{y} \cdot \frac{\delta E_e}{E_e} \oplus [\tan\left(\frac{\theta}{2}\right) + \left(\frac{1}{y} - 1\right) \cdot \cot\left(\frac{\theta}{2}\right)] \cdot \delta\theta, \\ \frac{\delta y}{y} &= \left(1 - \frac{1}{y}\right) \cdot \frac{\delta E_e}{E_e} \oplus \left(\frac{1}{y} - 1\right) \cdot \cot\left(\frac{\theta}{2}\right) \cdot \delta\theta, \end{aligned} \quad (3.9)$$

where  $\oplus$  denotes the quadratic summation of the terms. The error due to the polar angle  $\theta_e$  of the scattered electron is rising  $\sim \tan(\theta_e/2)$ . This is one of the reasons discussed in the next chapter to have a silicon tracker in the backward part of the detector.

It is also important to notice that the  $y$  resolution becomes perfect at very low  $x$ , improving as  $(1 - y)/y$ . The use of the electron method for this region is, thus, preferable. The applicability of the electron method has been restricted to larger  $y$  due to the term  $1/y$  (see Eqs. 3.9). For  $y < 0.15$ , methods are used which employ the kinematics reconstruction derived from hadrons.

2. The **Hadronic Method** [50] uses the hadronic variables  $P_t^{had}$  and  $\Sigma$ , measured by the calorimeters or eventually by both the calorimeters and the tracking detectors. The kinematic variables can be then expressed as follows:

$$y_h = \frac{\Sigma}{2E_e}, \quad Q_h^2 = \frac{P_t^{had}}{1 - y_h}, \quad x_h = \frac{Q_h^2}{s y_h}. \quad (3.10)$$

The precision of this method depends on the calorimeter sampling fluctuation which become more important at low  $P_t$ . At high  $y$  the resolution in  $Q_h^2$  and  $x_h$  degrades with the kinematical factor  $\sim 1/(1 - y)$  which limits the applicability of the hadronic method to small  $y$ . The electronic noise and a backscattering of the forward particles plays a crucial role for the accuracy of this method at low  $y$ .

This method also suffers from radiative processes. In order to make it less depend on initial state bremsstrahlung,  $2E_e$  can be replaced by the measured variable  $E - P_z$ . The resolution in kinematic variables can be improved by using electron  $P_t$  instead of the hadronic one. Both features were realized in the following method:

3. The  **$\Sigma$  method** [51] makes more efficient use of the redundancy of the measurement combining both the leptonic and the hadronic variables:

$$y_\Sigma = \frac{\Sigma}{E - P_z}, \quad Q_\Sigma^2 = \frac{P_{t,e}^2}{1 - y_\Sigma}, \quad x_\Sigma = \frac{Q_\Sigma^2}{sy_\Sigma}. \quad (3.11)$$

The inelasticity  $y_\Sigma$  in this case can be expressed by the purely leptonic and hadronic  $y$  variables:

$$y_\Sigma = \frac{y_h}{1 + y_h - y_e}. \quad (3.12)$$

For non-radiative events, the variable  $y_\Sigma$  coincides with  $y_h$ . They are about the same for low  $y$ . The resolution in  $Q_\Sigma^2$  is significantly better than that of  $Q_h^2$  due to the use of the leptonic  $P_t$  which at low  $Q^2$  is measured with the backward detectors. Still, it is about two times worse than the  $Q^2$  resolution from the electron method. The  $\Sigma$  method has been used for medium and low  $y$ , because the  $\Sigma$  variables have superior resolution due to the absence of the  $\sim 1/y$  term. The resolution of the kinematic variables depends on the electromagnetic and hadronic energy scale calibrations. The quality of these calibrations can be controlled with a reconstruction method which relies only on the hadronic angle and the one of the scattered electron.

4. The **Double Angle Method** [52] is based on the polar angles of the scattered electron  $\theta_e$  and that of the hadronic system  $\gamma$ :

$$y_{DA} = \frac{\tan(\theta_h/2)}{\tan(\theta_e/2) + \tan(\theta_h/2)}, \quad Q_{DA}^2 = 4E_e^2 \frac{\cot(\theta_e/2)}{\tan(\theta_e/2) + \tan(\theta_h/2)} \quad (3.13)$$

and

$$x_{DA} = \frac{Q_{DA}^2}{sx_{DA}}. \quad (3.14)$$

This method gives a good resolution in the region of medium  $y$  ( $0.05 < y < 0.3$ ). At large and small values of  $\theta_e$  and  $\theta_h$  the resolution in kinematic variables degrades as:

$$\delta Q_{DA}^2 = \frac{y-2}{\sin \theta_e} \delta \theta_e \oplus \frac{-y}{\sin \theta_h} \delta \theta_h, \quad \delta x_{DA} = \frac{-1}{\sin \theta_e} \delta \theta_e \oplus \frac{-1}{\sin \theta_h} \delta \theta_h. \quad (3.15)$$

Since the large polar angles of the scattered electron and small hadronic angles correspond to low  $Q^2$  and low  $y$  regions, respectively, the use of the DA method is problematic here. Due to the relative insensitivity of the kinematics reconstruction to the overall energy scale the DA method is widely exploited for calibration purposes.

The redundancy of the measurement of the final state variables needed for deep-inelastic scattering kinematics reconstruction was exploited in the present analysis in order to optimize the resolution of the kinematic variables. The electron method was used for  $y > 0.15$ . Due to the good  $y$  resolution, a  $y$  binning was used for  $y > 0.6$ . The  $\Sigma$  method was used for  $y < 0.15$ . A coarser binning at very low  $y$  was chosen to account for degrading resolution at low  $y$  as discussed in Section 6.2. A comparison of double differential cross sections obtained with these two systematically different methods is given in Section 6.5.

### 3.4 Event and Detector Simulation

A detailed simulation of the H1 experiment comprises two general steps: generation of  $ep$  physics events and of the detector response.

1. The physics simulation includes a generation of the DIS process events and their background. The following software packages have been used:
  - **DIS** events are generated using DJANGO [53] event generator which is based on Lund Monte Carlo generator ARIADNE [54] and HERACLES [55]. The ARIADNE program uses Color Dipole Model [56] and includes the generation of diffractive events. The GRV 5.04 [57] parton density parameterization with the Leading Order DGLAP evolution was utilized. The HERACLES program includes electroweak interactions, the  $F_L(x, Q^2)$  structure function and performs first order radiative corrections to the DIS process. The calculations were cross checked using various tools and a very good agreement between them all has been found [37].
  - The **COMPTON** [58] program has been used to calculate the elastic contribution to the QED Compton events since the HERACLES does not perform this correction. There were  $6 \text{ pb}^{-1}$  QED Compton events generated and added to the DJANGO event sample normalized to data luminosity.
  - **Low W**: Due to basic parton model assumption, the event generation in DJANGO is limited to hadronic system mass  $W > 5 \text{ GeV}$ . “Low W” events were generated with HERWIG [59] event generator which uses a built-in cluster model and includes an average treatment of the resonance region.
  - **Photoproduction** is the main physical background process which complicates the deep-inelastic scattering cross section measurement at low  $Q^2$  especially at high  $y$ . The PHOJET [60] event generator has been used to simulate this source of background for systematic studies. It is necessary to estimate the amount of photoproduction events which fake the DIS signature. The estimated contribution of such events normalized to data luminosity was then subtracted bin-wise from the data (see Section 6.4). The event generator PHOJET uses the ideas of the two-component Dual Parton Model

(DPM) [61] combined with perturbative QCD and simulates both so called soft and hard subprocesses by an unitarization scheme. This program incorporates major components of the total photoproduction cross section such as non-diffractive, single and double diffractive and vector meson production. A detailed study of the hadronic final state performed in [62] showed a significant excess of baryon generation which was reduced by a factor two. A CKMT [63] parton density parameterization has been used and the first order radiative corrections have been applied.

2. The correct detector simulation takes most of the time. The generated Monte Carlo events are the subject for further reconstruction performed in two stages:

- **H1SIM** [64] is the program package based on GEANT [65] software. It reads the events and simulates the H1 detector response taking into account the geometry and acceptance of its subdetectors as well as dead material distributed within the detector. A shower simulation in the passive and active material is done with the program H1FAST using some shower parameterizations.
- **H1DIGI** runs after H1SIM and performs a so-called “digitization” of the simulated hits. It applies the efficiency and noise corrections and calibration constants obtained from data and test beam studies (see Chapter 5).

The DIS Monte Carlo event sample used in the presented low  $Q^2$  analysis corresponds to an integrated luminosity of  $3.457 \text{ pb}^{-1}$  resulting in typically less than 1% statistical error in the analysis bins. Its contribution to the total error is achieved to be negligible. The  $\gamma p$  Monte Carlo event sample amounts in total  $0.5 \text{ pb}^{-1}$  and is sufficient for estimation of the remaining photoproduction background. It is important to notice that the simulated events proceeded the same reconstruction and analysis chain as the real data. Comparisons between data and Monte Carlo simulation in this analysis are shown with simulated spectra normalized to data luminosity.

## 3.5 The Data Sample

In August 1997 it was proposed to take data with a special “minimum bias” run with triggers opening the inner SpaCal region in order to get an unbiased data sample for  $Q^2$  range below  $10 \text{ GeV}^2$  [66]. The precision of data previously taken was about 10 % which was dominated by the systematic errors. In order to reach better understanding of systematic effects and to reduce the statistical errors, a data sample of about  $2 \text{ pb}^{-1}$  was taken within two weeks in the fall of 1997.

### 3.5.1 Trigger and DAQ

Special DIS physics triggers were proposed [67]. Since the trigger rate rises rapidly with decreasing  $Q^2$  and with increasing  $y$ , a compromise in trigger definitions had to

Subtrigger	Definition	Comments
S0	$E > 5 \text{ GeV} \ \& \ r > 10 \text{ cm}$	minimum bias, main trigger
S3	$E > 10 \text{ GeV}$	minimum bias, lowest $Q^2$ trigger
S9	$E > 2 \text{ GeV} \ \& \ t_0 \ \& \ r > 10 \text{ cm}$	high $y$ trigger using tracks

Table 3.4: Definition of the DIS subtriggers which were used in the the minimum bias run, see text.

be found concerning minimum energy and fiducial cut values applied using the SpaCal L2 trigger system [68]. This was realized with three subtriggers devoted to certain kinematic regions: S0, S3 and S9.

All these subtriggers are primarily based on an inclusive electron trigger (IET) of the backward calorimeter which can be set to three energy thresholds in the range between 100 MeV and 20 GeV. The IET trigger is active during the expected time of arrival of signals from good  $ep$  interactions only, thus it is rather insensitive to beam background.

The S0 was the main subtrigger of the low  $Q^2$  run with an IET energy threshold of 5 GeV. The second level radius fiducial cut was set to  $>$  about 10 cm in order to ensure the BST to be in the trigger acceptance.

The S3 was used to reach lowest possible  $Q^2$  values. It has no L2 validation requirements but the energy threshold had to be set to 10 GeV in order to provide a reasonable trigger rate.

The S9 is the special high  $y$  subtrigger with lowest energy threshold set to 2 GeV. A requirement for tracks pointing to the vertex region had to be included in its definition, which, in conjunction with a  $t_0$  condition from the proportional chambers, provides a sample of DIS events. The S9 trigger definition is complemented by the L2 cut in order to further reduce trigger rate. An additional suppression of the trigger rate was applied by masking out the problematic regions in the SpaCal.

During the minimum bias run a new L4 strategy, namely autoprescaling, was successfully applied. The basic idea of this approach is to automatically adjust the prescale factors of triggers depending on the beam currents and background conditions in order to make optimal use of luminosity [69].

### 3.5.2 Run Selection and Time Stability

The data is taken in a “lumi fill” which is the period from the moment when HERA announces luminosity until one of the beams is dumped or lost. During lumi fills H1 accumulates data in a sequence of “runs” which are the quanta for database information. For example, the accumulated luminosity is a run dependent quantity. If some

Runs	Comments
200445	Strange L5 weights
201141	Lumi platform mistakenly moved
201281 - 201283	BST readout problem
201293	BST readout problem
201439	No L4 histograms for BST (not efficient)
201441	BST readout problem
201445	BST readout problem
201470 - 201481	BST is not operational
201220	Pretest for L4 scheme 2000

Table 3.5: List of bad runs for minimum bias run.

kinds of problems occur by data taking, the whole run or part of it must be dropped from analysis. There were more than one thousand runs taken during the minimum bias run in the range between #200444 and #201519, resulting in a luminosity of more than  $2 \text{ pb}^{-1}$  suitable for further analysis. Not all runs could be used in analysis due to detector instability, large background, obvious hardware problems or even different L4 filter schemes. Therefore, before starting the DIS analysis a run preselection is required. The following criteria were applied to select a reliable data sample:

- **Run quality:** First, the shift crews provides H1 with a run classification based on their own experience with the hardware or software conditions during each run. Afterwards the runs were checked by different offline criteria and classified as good, medium or poor. Only good or medium runs were selected.
- **Trigger phase 2:** There were only two phases in the minimum bias run. The first phase has usually bad beam conditions causing inability to switch on the trackers or requiring its ramping. In this phase the SpaCal triggers are highly prescaled.
- **High voltage - Readout status:** The HV status of the most important components of the H1 detector (SPACAL, BDC, BST, CIP, COP, CIZ, CJC and LAr) for low  $Q^2$  DIS analysis was checked. If the fraction of time when all relevant detector components were at nominal HV was lower than 70% - a run was not accepted. The value of 70 % has been chosen from stability studies [70]. A run was not accepted if one of the important branches was not in readout.
- **L4 readout tests** for a future readout scheme were performed during lumi fills 1593 and 1594. These have been skipped in the analysis.
- **BST readout status:** Additionally to the HV status, BST efficiency was explicitly checked offline. There were some runs found where the BST seemed to be operational but no L4 histograms could be found or it had zero efficiency. Those runs were also excluded from the analysis (see Table 3.5).

The list of runs rejected by hard- or software problems was obtained from a bank PQR7. The final event sample comprises 208 runs. A fraction of 33% of the luminosity was thus *a priori* removed from the data sample.

# Chapter 4

## The Backward Silicon Tracker

This chapter describes the main aspects of the Backward Silicon Tracker in its 1997 configuration. The motivation to supplement the backward apparatus of the H1 detector with the BST is discussed first. An overview of the technical design of the tracker and its readout system is given in Section 4.2 and Section 4.3, respectively. The ideas of the online hit recognition and offline track reconstruction are briefly described then.

The second part of the chapter is devoted to a detailed study of the BST performance based on the  $ep$  data. This study comprises an efficiency investigation of the detector and its readout chain (Section 4.5 and Section 4.6, respectively). The tracker alignment is described in Section 4.8.

The chapter concludes with a description of the alignment procedure of the backward calorimeter SpaCal and the backward drift chamber BDC which is essential for cross checking the angular measurement with the BST and for further physics analysis.

### 4.1 Purpose

The Backward Silicon Tracker is installed in the backward region of the H1 detector (see Fig. 4.1) and serves for identification of the scattered electron and precision measurement of its polar angle in the  $Q^2$  range between 1 and 20 GeV<sup>2</sup>. The coverage of the kinematic region with the BST is illustrated in Fig. 4.2, showing lines of constant scattering angles and energies in the  $(x, Q^2)$  plane at nominal beam energies at HERA. The measurement of the inclusive  $ep$  DIS cross section at high  $y$  benefits from the insensitivity of the silicon detectors to neutral final state particles whose electromagnetic component can mimic an electron signature in the backward electromagnetic calorimeter SpaCal.

A major design criterion for the BST has been that the contribution of the BST to the  $x$  and  $Q^2$  resolutions should not exceed the one of the backward electromagnetic calorimeter, i.e. a few per cent. The resolution of the kinematic variables was

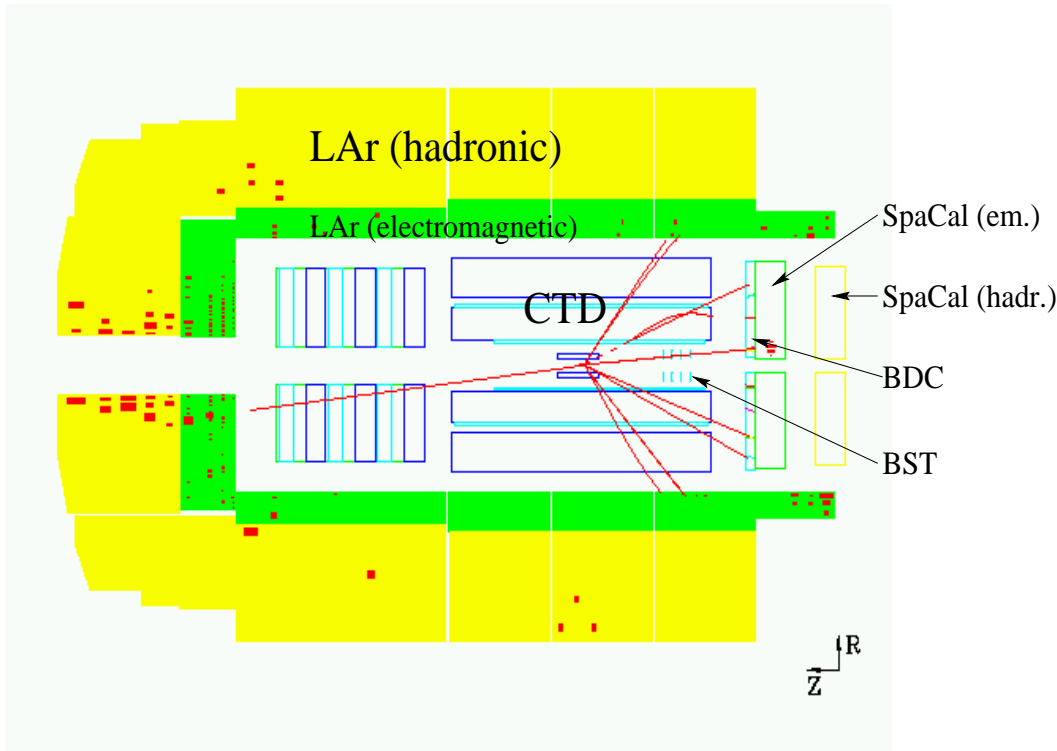


Figure 4.1:  $R - Z$  view of the H1 detector with a typical of a DIS event with the scattered electron measured with the BST.

investigated with a Monte Carlo simulation. The results of a resolution study using non-radiative events is presented in Fig. 4.3 for  $y > 0.15$  where the electron method is best applicable. Also shown (where visible) are the results obtained without the BST. As expected, the BST angular measurement does not contribute significantly to the total kinematic resolution which is dominated by the SpaCal energy measurement (see Eqs. 3.9). Typical resolution values are 3% for  $Q^2$ , 7% for  $x$  and 4% for  $y$ . These values permit a fine binning in  $Q^2$  and  $y$  which is necessary for the determination of the longitudinal structure function  $F_L$ .

Different physics requirements lead to the following tasks of the BST:

- The polar angle of the scattered electron has to be measured with an accuracy of better than 1 mrad;
- The detector efficiency has to be high for efficient electron identification which is done by validating the electron candidate cluster in the SpaCal with a linked track measured with the BST (see Appendix A) and for suppression of photoproduction background at high  $y$  by rejecting its neutral component due to  $(\pi^0 \rightarrow 2\gamma)$  decays. Partially, charged hadrons are rejected by the matching requirement of a BST track with a SpaCal electron candidate cluster (see Section 6.4);
- At large  $x$  and low  $Q^2$  DIS events at HERA are characterized by a single backward scattered electron. With the BST these events could be saved for kinematic reconstruction and data be obtained in the overlap region with the fixed target experiments (see Section 6.2).

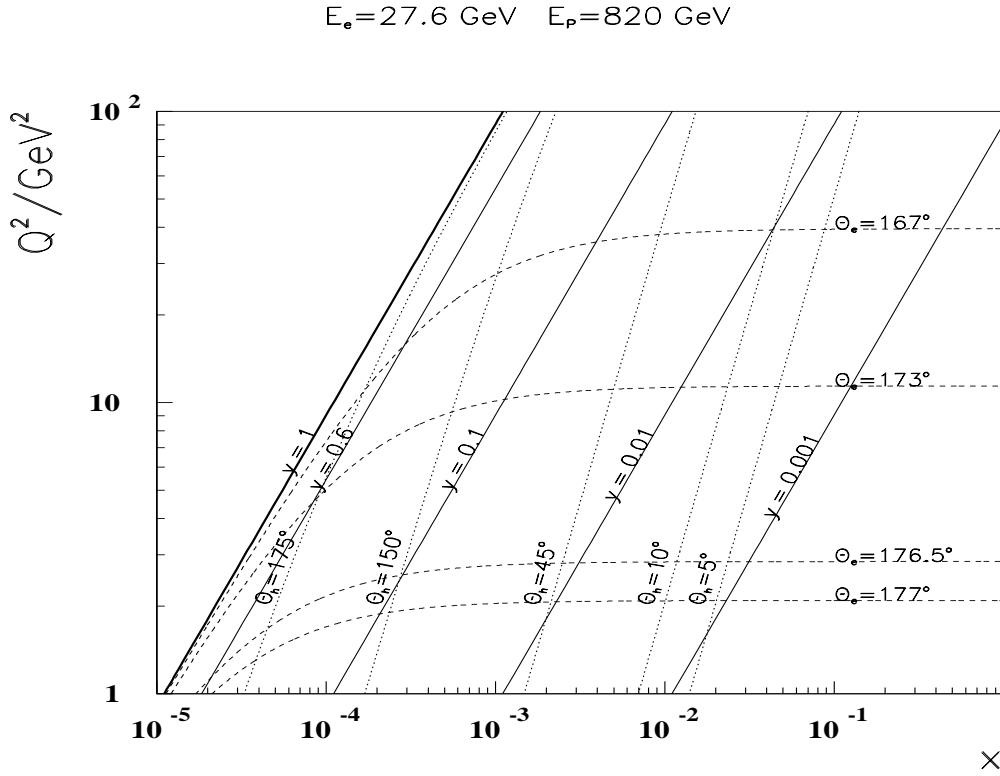


Figure 4.2: Kinematic range covered by the BST. The dashed lines of constant polar angle  $\theta_e$  represent the BST acceptance. The outer (inner) lines mark the “2-out-of-4” (“4-out-of-4”) region which is accessed with two or four BST planes out of the 4 existing. The dotted curves correspond to constant jet angles  $\theta_h$ . Also shown are lines of constant inelasticity  $y$ .

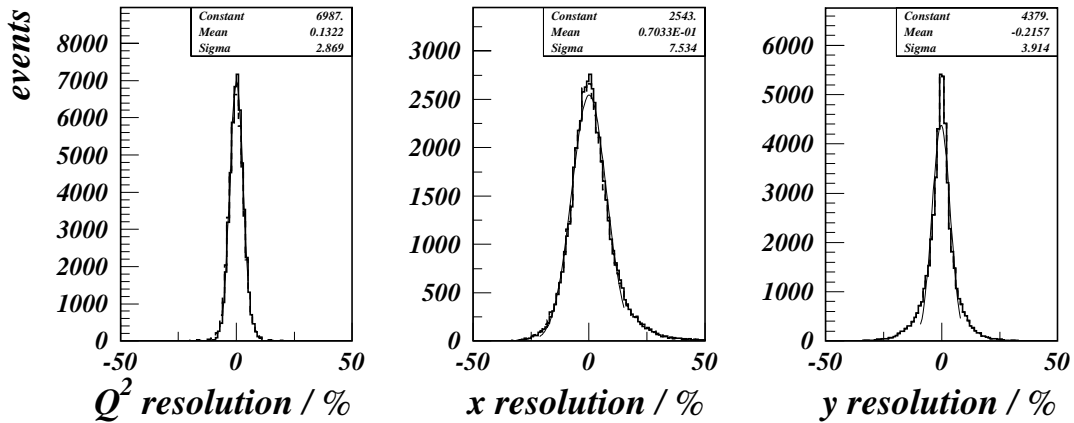


Figure 4.3: The resolution of the kinematic variables in the low  $Q^2$ , high  $y$  region with and without using the BST illustrated by the solid and hatched curves, respectively.

## 4.2 Design

The BST geometry was optimized in order to provide a most efficient registration of the scattered electron and to obtain the required angular measurement accuracy [72, 73]. The BST was installed in the H1 detector in the year 1996 and it was equipped with programmable readout electronics in the year 1997. Initially, the silicon tracker consisted of four planes arranged concentrically around the beam axis. Its schematical sketch is illustrated in Fig. 4.4. The  $z$ -positions of the active planes satisfy the requirement of forming trigger roads for the BST pad trigger detector [74]. Such a non-equidistant arrangement ensures the largest possible plateau of the BST polar angle acceptance and obeys the following relation:

$$z_{i+1} = z_i \cdot \sqrt[n]{\frac{r_{max}}{r_{min}}}, \quad (4.1)$$

where  $r_{min}$  and  $r_{max}$  denote the inner and outer active radius of the sensitive detector region and  $n = 8$  corresponds to the radial subdivision of the trigger detectors. The  $z$ -positions of the planes are -73.20, -80.03, -87.50 and -95.66 cm, corresponding to the first, second, third and fourth plane, respectively. Each plane is composed of 16 identical wedge shaped silicon detectors with  $r_{min} = 5.9$  cm and  $r_{max} = 12.04$  cm. The outer radius of the detectors is limited by the inner proportional chamber and by the space needed for the hybrid electronics and for cabling of the central silicon tracker. The detectors are staggered in  $z$  with a 3 mm overlap in  $\phi$  allowing for some redundancy in track reconstruction and for a hermetic angular measurement. The support structure is made of carbon fiber reinforced plastics (CFRP) to which the detector modules are fixed. Each module consists of a Silicon wafer and a thin single layer printed circuit board (hybrid) which carries the amplifier chips bonded to the sensor as schematically illustrated in Fig. 4.5.

The BST is composed of two symmetric half shells. The halves are enclosed by an inner and outer shield made of a G10 foil carrying a double sided 35  $\mu\text{m}$  Cu layer.

Each step of detector construction was controlled in order to reach best possible mechanical accuracy. Position markers on the sensors allow to align the detectors on the CFRP support frame such that the strips of the 16 detectors of one plane form a circle with respect to the central axis. This is controlled using a microscope and a turnable PC-steered  $x,y$ -table. The radial position of the modules is determined by position pins on the CFRP frame to a precision of 30  $\mu\text{m}$ . The  $z$ -positions of the planes are precisely defined by CFRP/Aluminum distance between the detector planes. The final alignment is done using  $ep$  data and is described in Section 4.8.

### Wafers

The active material of the detectors is n-type silicon, 300  $\mu\text{m}$  thin. About 22000 electron-hole pairs are produced by a single minimum ionizing particle scattered in the active volume of the wafer. Applying a depletion voltage between p-side and n-side of the silicon sensors creates a reverse-biased p-n-junction. The electron-hole pairs drift

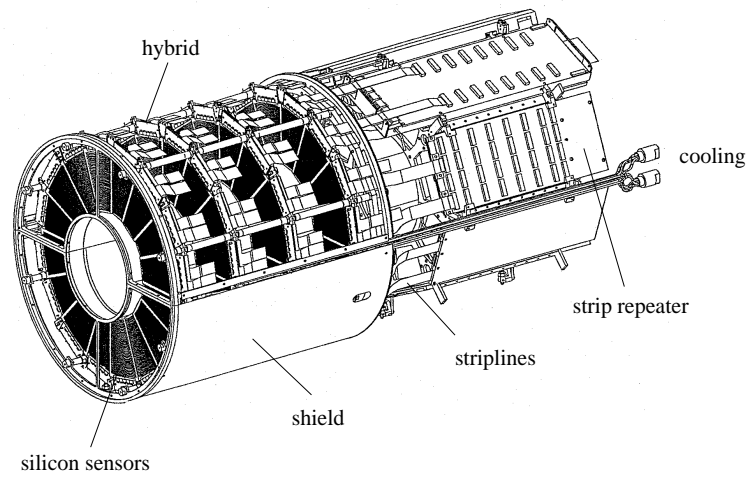


Figure 4.4: Schematic view of the 4 plane BST detector with associated front-end (repeater) electronics.

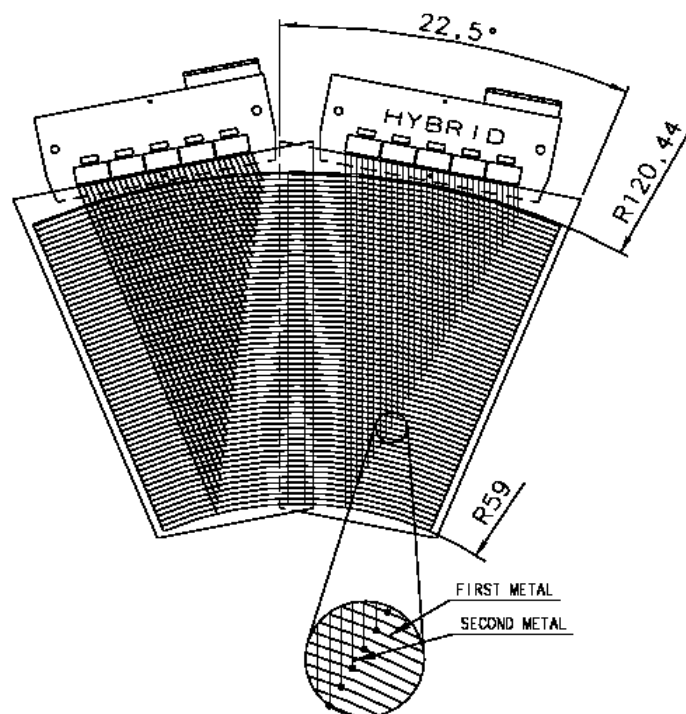


Figure 4.5: Schematic view of two adjacent BST sensors.

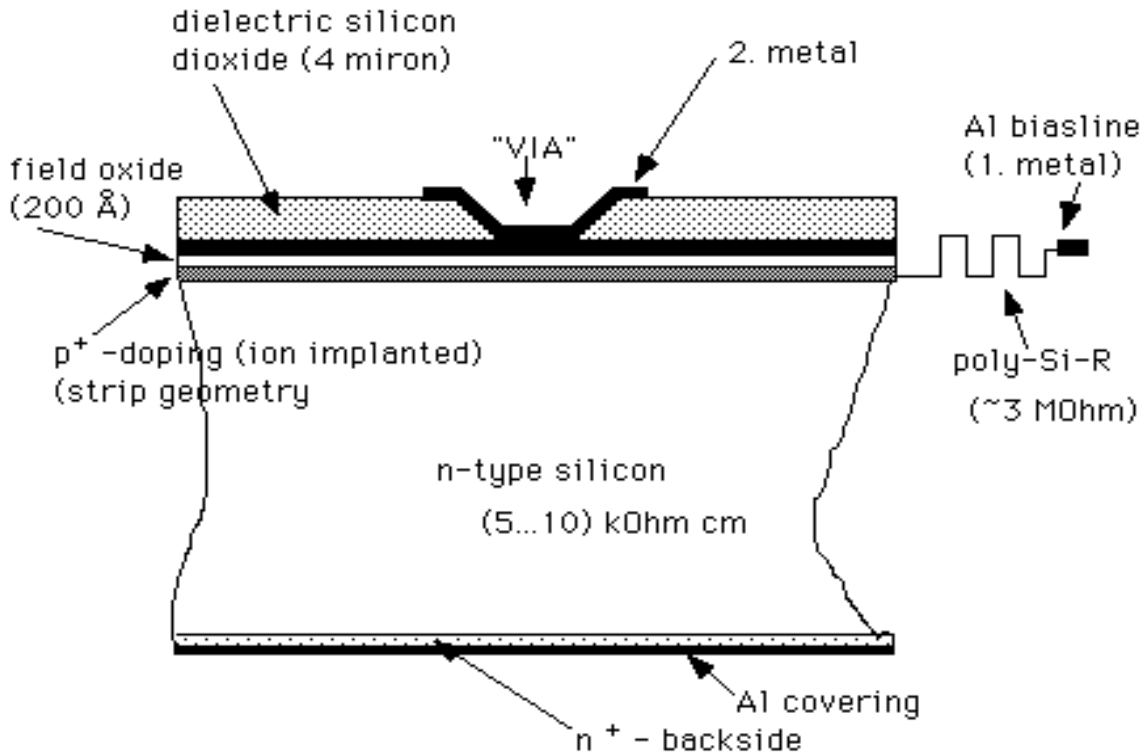


Figure 4.6: Cross section of the single sided, double metal,  $300\ \mu\text{m}$  thin silicon  $p^+$ -type strip detector of the BST.

in the fully depleted silicon substrate to the  $p^+$ -implant strips and to the n-side contact, respectively. The design of the AC-coupled wafer is shown in Fig. 4.6. Since the wafers are mounted almost perpendicular to the direction of the incident particles, the contribution of the wafers to the dead material in front of the SpaCal is less than 3% of  $X_0$  [72]. The main contribution to the dead material arises from the readout electronics, cabling and mechanics of the BST contributing about 10-30% of  $X_0$  depending on the angular range. The radial strip geometry and the desire to mount the electronics in the outer part of the BST required to use a double metal layer technology. The sensor has 1280 concentric AC-coupled  $p^+$  strips with a pitch of  $48\ \mu\text{m}$ , each second strip being read out. The second metal layer on a thick dielectric serves for routing the charge, induced by a charged particle, to the outer end of the sensors (see Fig. 4.5). It has accordingly 640 read out lines connected to each second strip from the first metalization.

### 4.3 Data Acquisition

The parameters of the silicon strip detector and the environment in which it is operated impose particular challenges and constraints on the readout of the BST:

1. The large number of readout strips requires a highly integrated front end system;

# BST • Strip Detector Modules & Wiring

Setup: BST1 (1997)

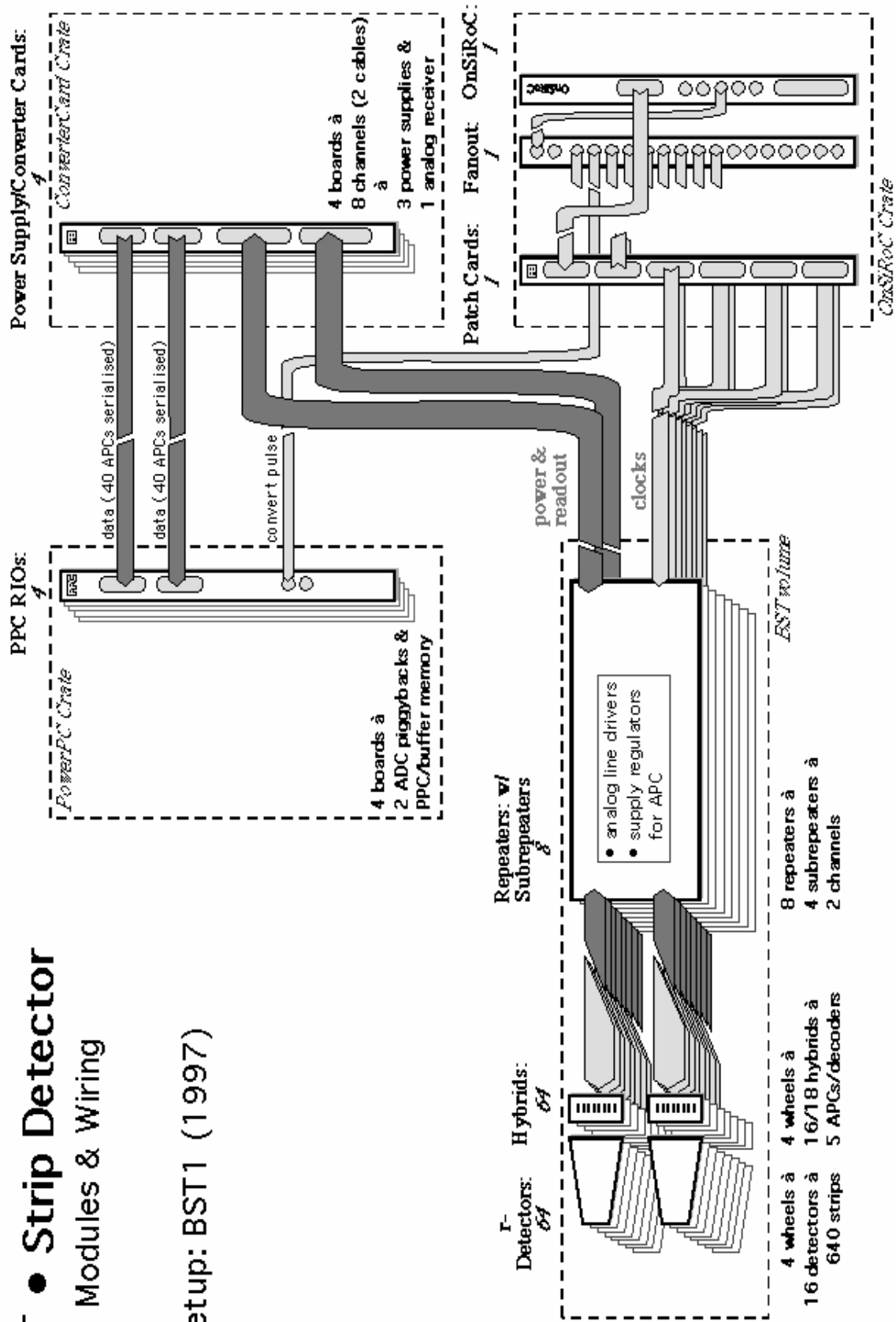


Figure 4.7: Schematic diagram of the BST readout system. Dark and light lines correspond to data readout and synchronization with the HERA clock, respectively.

2. The HERA bunch repetition rate of 10.4 MHz requires a multi-event pipeline buffer in order to decouple the processing stage and the online hit finding procedure from the front end data;
3. The readout has to be fast enough in order to produce no additional dead time and reduce the large data volume;
4. Finally, the readout electronics must be sufficiently radiation hard for the application at HERA.

The readout chain of the strip detector signals is schematically represented in Fig. 4.7. It comprises the following elements:

### Front end readout

In order to minimize the attenuation of the small signals induced by the charged particles traversing the fully depleted silicon substrate, the front end electronics is carried by so-called hybrid PC-boards which are glued and bonded directly to the silicon sensors. The main components of the hybrid electronics are: five amplifier **A**nalog **P**ipeline **C**hips (APC) [75] specially developed for H1, five decoder chips which generate 14 steering signals which are necessary to operate the APC from only four control lines, and an analog cable driver.

Each APC supports parallel sampling of 128 channels. Each APC channel consists of a low power, low noise charge sensitive preamplifier followed by a storage network of latch capacitors to record data from 32 consecutive bunch crossings. The depth of 32 pipeline elements is matched to the first level trigger decision, which has to be taken within about  $2.5 \mu\text{s}$ . When a trigger stops the sampling, the pipeline can be re-read by the input preamplifier and charge will be stored on a latch capacitor of each channel. This procedure reduces the power consumption and allows online noise suppression by subtraction and addition of several pipeline buffers. This is realized in a special “sequencer code” running on the OnSiRoC module. Dedicated tests showed a radiation hardness of about 100 krad of the powered chip. During three years of running the APC’s of the BST received an integrated dose of maximum 43 krad depending on their azimuthal and radial position as is shown in Fig. 4.8. So far no degradation of the readout performance was observed.

### Repeater Boards

The repeater electronics serves for voltage supply, APC steering and signal transmission purposes. It consists of eight multilayer printed circuit boards placed concentrically around the beam pipe just behind the active BST area (see Fig. 4.4). Eight detectors of two  $\phi$  sectors are connected to one motherboard. The repeater electronics performs a bias voltage filtering and provides current sources and power converters for the hybrid supply. A video amplifier is used for long line analog signal transmission to the electronic trailer via about 35 m of coaxial cables.

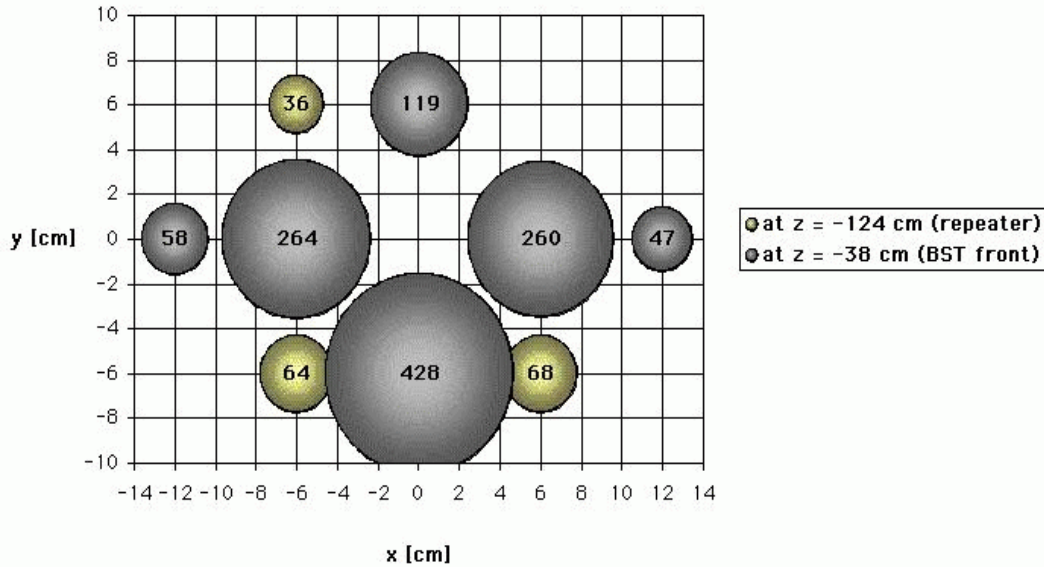


Figure 4.8: Radiation dose absorbed by different parts of the BST during three years of operation. The values are given in Grays (10 Gy=1 krad).

### OnSiRoC

The **Online Silicon Readout Controller** was developed in order to cope with the complex requirements of controlling and recording the information from the APC. This VME module comprises a single channel sequencer (a programmable unit which controls the OnSiRoC functions), pedestal memory, buffer and channel counters, a 4 channel sampling ADC and raw data memory plus a complete hybrid powering system. In 1997, the complete analog readout and digitization needed about 1 ms. This is below the value of the slowest readout branch and, thus, introduced no additional dead time. In order to disentangle the multiple functions of the OnSiRoC, two of its three tasks were given to separate electronic modules: the hybrid electronics and bias voltage is supplied by converter cards and the analog-to-digital strip signal conversion and hit recognition is done on commercial Power-PC boards with 10 MHz FADC attached to it.

### Power-PC and Online Data Processing [77]

The digitized pulses are examined by a hit finding procedure running on Power-PC-based VME modules of the type CES RTPC 8067 which have an PCI interface with the 12 bit ADCs. This system allows programmable online data reduction, hit finding and multi-event buffering. The BST produces a data flow of about 40000 digital amplitude signals per event which has to be reduced by 2-3 orders of magnitude within 10 ms in order to fit to the 4 kbyte storage space for the BST readout branch. This requires a special hit detection algorithm which has been developed in the C language, avoiding mathematical library functions such as square root in order to speed up the analysis procedure. The algorithm has been implemented in 32 bit integer arithmetics on the

processor which permits pipelined instruction processing with three integer processing units.

### Hit Recognition

At each processor start the online data processing requires normally  $n = 64$  events for initialization to calculate pedestal and noise values. These are derived from the common mode corrected amplitudes  $A_i$ , pedestals  $P_i$  and noise squared  $N_i$  applying a weight  $w = 1/n$ , according to the following iterative formulae:

$$\begin{aligned} P'_i &= (1 - w)P_i + A_i, \\ N'_i &= (1 - w)N_i + w(A_i - P_i)^2. \end{aligned} \quad (4.2)$$

The subsequent hit finding procedure determines common mode and common slope for each APC by a straight line fit of the pedestal subtracted amplitudes versus channel numbers. Here, the noisy strips and outliers (signals are treated as outliers, too) are masked out. Then the correct amplitude is calculated according to the formula:

$$A_i = A_i^0 - P_i - (C_k + S_k \cdot i), \quad (4.3)$$

where  $A_i^0$  is the raw amplitude of the strip  $i$  with the pedestal  $P_i$  of the APC  $k$  with the common mode  $C_k$  and common slope  $S_k$ . The cluster search is performed for each strip using a window of three channels since the tracks are almost perpendicular to the detectors. The cluster is treated as a signal if the sum of the amplitudes squared in the window exceeds a certain threshold depending on the noise. This procedure can be inferred from a pedestal subtracted raw event shown in Fig. 4.9. The candidate hits are read out in a condensed format (address, pulse height and noise squared) and stored in a bank (SIFE), available on raw data tapes for further reconstruction.

## 4.4 Offline Reconstruction

The BST reconstruction code (BSTREC) [78] searches for tracks calculating a triplet sagitta  $s = (r_1 + r_3)/2 - r_2$  between the hit coordinates  $r_i$  measured in three successive planes  $i$ . The resolution of the BST related to the sagitta as  $s \cdot \sqrt{2/3}$  is shown in Fig. 4.10 (left). This quantity exhibits a clear signal from the tracks above a small combinatorial background. Prior to application of sagitta cut, the internal alignment has to be performed (see Section 4.8.1). Because of the high resolution of the BST and its good S/N performance, the sagitta cut can be used as the main filter of the pattern recognition.

The distribution of the signal-to-noise is shown in Fig. 4.10 (right). The  $S/N$  ratio has a peak value of about 13 and shows the performance of the combinatorial filter algorithm. A cut  $S/N > 5$  is chosen as a good compromise between picking up noise and signal loss which is below 5%.

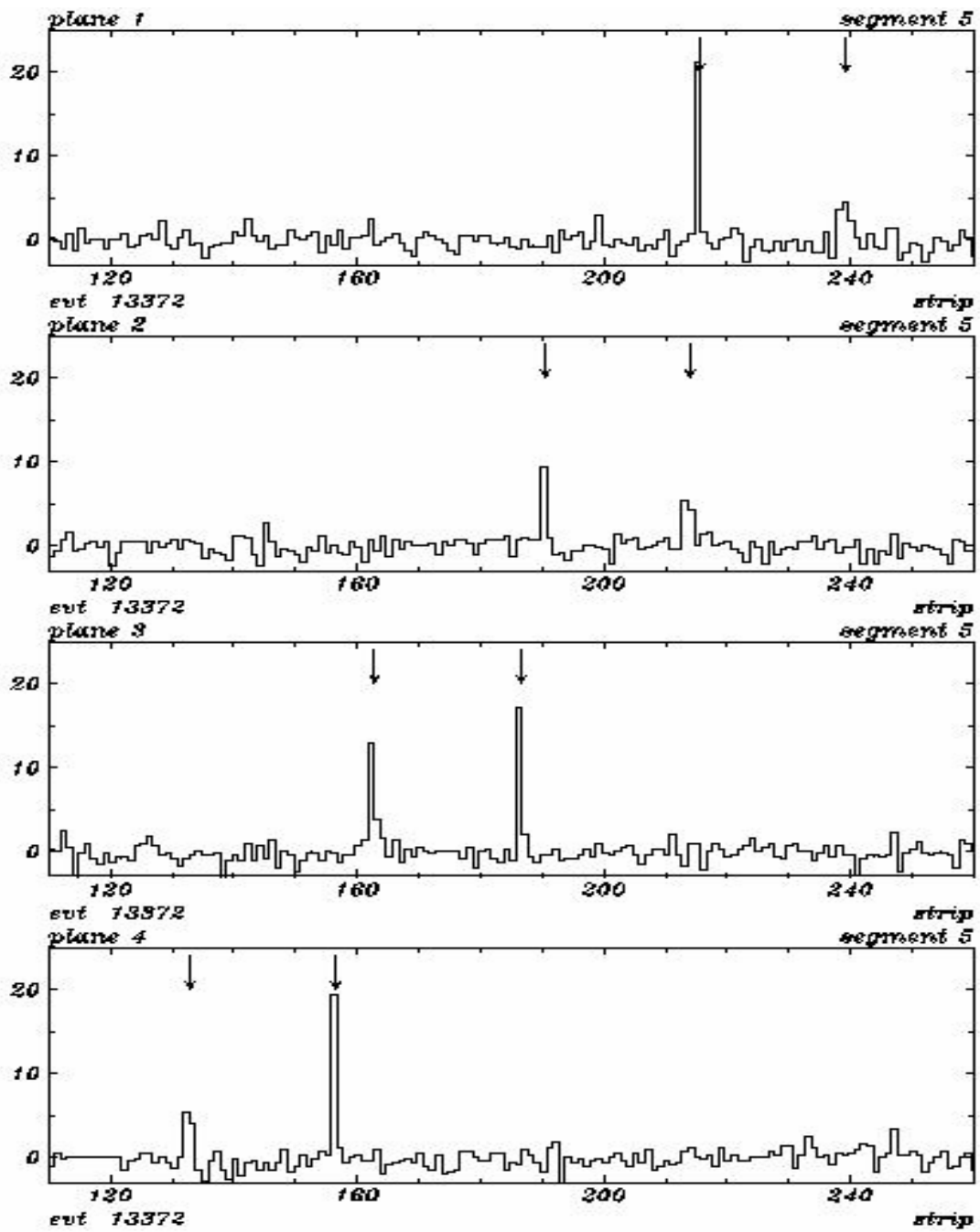


Figure 4.9: An example of an event with the recognized hits induced by two charged particles which crossed the four successive planes of the BST.

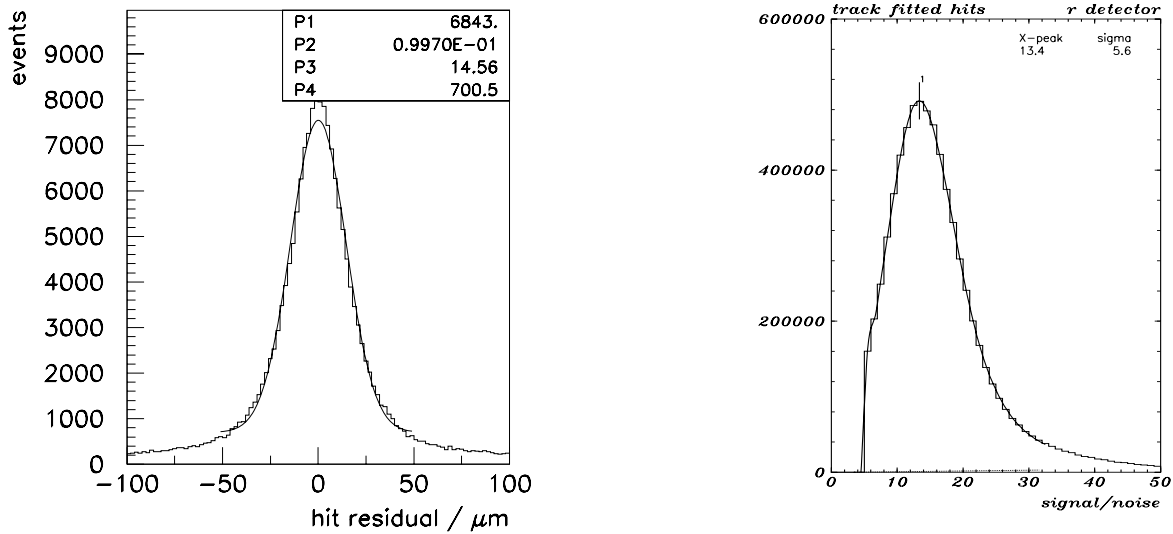


Figure 4.10: Left: Residual distribution of the BST. Right: Signal to noise ratio of the 64 detectors constituting the BST. A cut  $S/N > 5$  has been applied during offline data processing.

Up to 250 hits which passed the offline filter are stored in a bank (BRSE) available on DST's. For the physics analysis a special algorithm (“electron finder”, see Appendix A) was developed. This algorithm performed track reconstruction in the BST using SpaCal cluster information to recognize electrons and to extend the BST acceptance range. During Ntuple production up to 70 BST hits were accepted, in order to be able to possibly improve the alignment or detector efficiency description in Monte Carlo simulation. These hits were preselected in a wide  $\phi$ -window around the SpaCal cluster and stored permitting thus to rerun the BST electron finder on the Ntuple level.

## 4.5 Internal Efficiencies

The measurement of the deep-inelastic cross section requires a precise knowledge of the detector efficiencies and their correct implementation in the Monte Carlo simulation. Thus, prior to physics analysis the efficiency of the BST response was studied in detail. Using the redundancy of the BST having four planes an internal detector efficiency for each module could be determined. Use of external SpaCal and vertex information defined the overall efficiency and allowed to check in particular the readout.

A sample of events with a track in the BST acceptance linked to a most energetic cluster in the SpaCal with energy above 20 GeV has been used to monitor the internal efficiencies. This requirement ensures a clear electron signature. A good vertex reconstructed with the central tracking detectors was required in order to suppress QED Compton events. Further, the azimuthal angle of a track measured with the SpaCal

was used in order to identify the BST sector being crossed by the scattered electron. A strict  $\phi$  cut around the  $\phi$  center of a given sector was applied to prevent any sector misidentification.

A single hit efficiency has been determined with the requirement that a hit in the studied detector has to be assigned to a track defined by all three adjacent detectors. If a sector contains a dead detector, two adjacent detectors define the track.

The results of this study are presented in Fig. 4.11 which shows the internal efficiencies of all 64 detectors except three which were off or run with very low efficiency, all three marked as “dead” in the figure. The average value of the BST internal efficiency is about 92% excluding these three “dead” detectors. The detector inefficiency originates from several reasons: i)  $\sim 1.5\%$  due to dead channels (not connected strips or shorts) measured in a laser beam test carried out prior to installation [79], ii)  $\sim 5\%$  due to the  $S/N$  cut, iii) the rest  $\sim 1.5\%$  could be due to occasional high noise.

## 4.6 Coherent losses

The study of the detector internal efficiency showed a detector performance resulting in bigger than 90% single hit efficiency on average. Taking into account the track reconstruction algorithm based on the “2-out-of-4” concept (see Appendix A), one expects an external efficiency to be very close to 100% according to the binomial expression:

$$\varepsilon_{ext} = \varepsilon_{int}^4 + 4\varepsilon_{int}^3(1 - \varepsilon_{int}) + 6\varepsilon_{int}^2(1 - \varepsilon_{int})^2 \approx 100\% \quad \text{for } \varepsilon_{int} = 92\%. \quad (4.4)$$

Eq. 4.4 is valid for the case when a track crosses all four planes of the BST. Therefore, to check the presence of possible coherent losses in the readout chain, event candidates were preselected in the 4-out-of-4 region of the BST using a prediction based on the SpaCal high energetic cluster validated by the BDC drift chamber and the  $z$ -vertex position measured with the central trackers to an accuracy of better than 0.3 mm. Both cuts exclude a bias of the analysis by final state photons.

Events which passed these cuts were checked with respect to the total number of hits in the preselected BST quadrant defined by the SpaCal cluster position. Events with less than two hits were considered to be due coherent loss in the readout chain since the expected external inefficiency in case of no coherent losses is very close to zero.

Fig. 4.12,a) shows the total hit number distribution for such events where a clear peak at zero represents the full readout losses. This type of losses is basically caused by so-called “hot” or “silent” quadrants. A quadrant (four sectors of the BST) was considered as “hot” when the number of hits found by the online hit finding procedure exceeded 500 in a given Power-PC. In this case the quadrant is declared to be “hot” and the found hits are dropped. This means that for an event with total number of hits equal to zero on analysis level, more than 500 hits were found in each BST quadrant

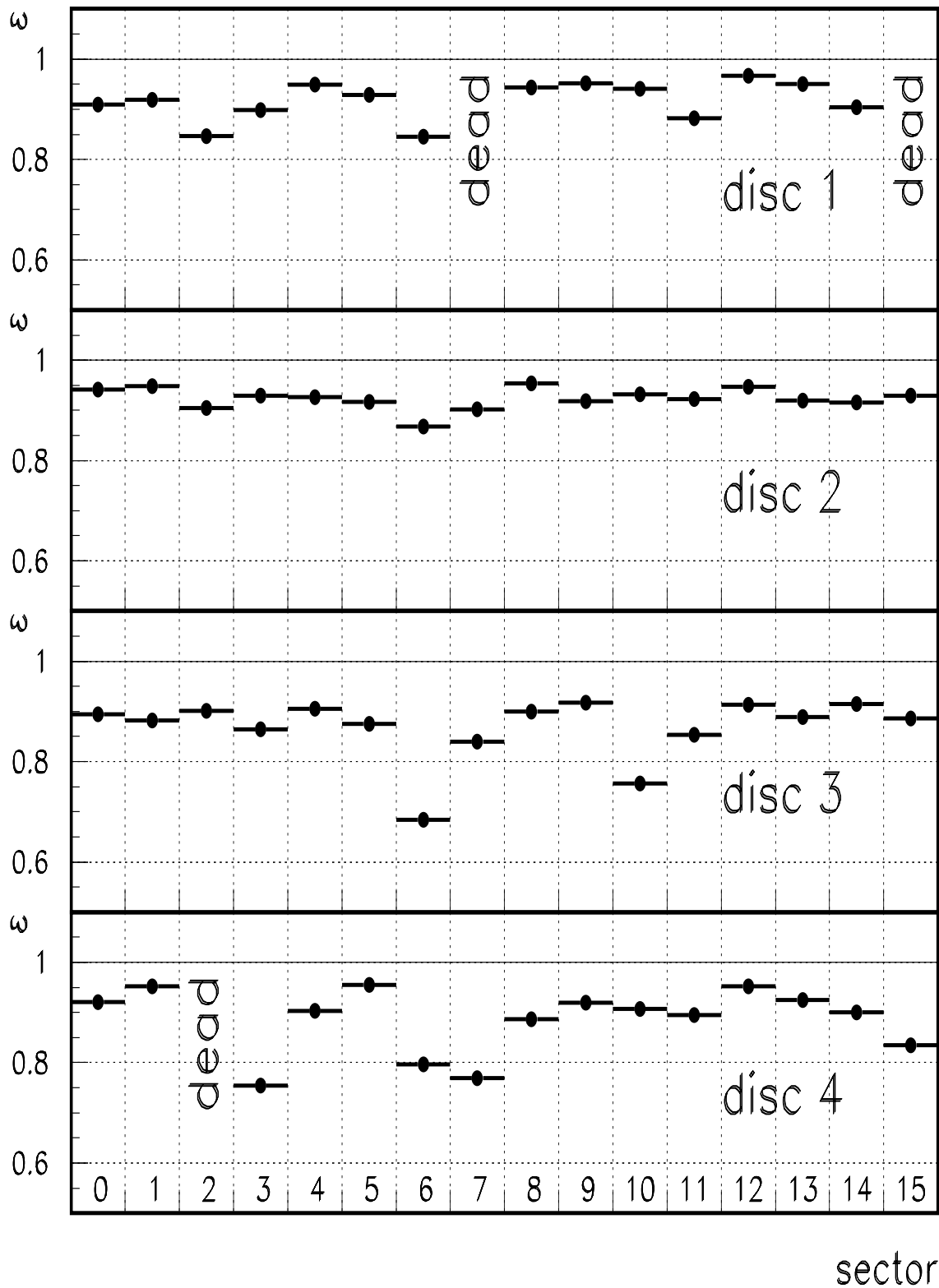


Figure 4.11: The internal efficiencies of the BST detectors for the special low  $Q^2$  run taken in October 1997.

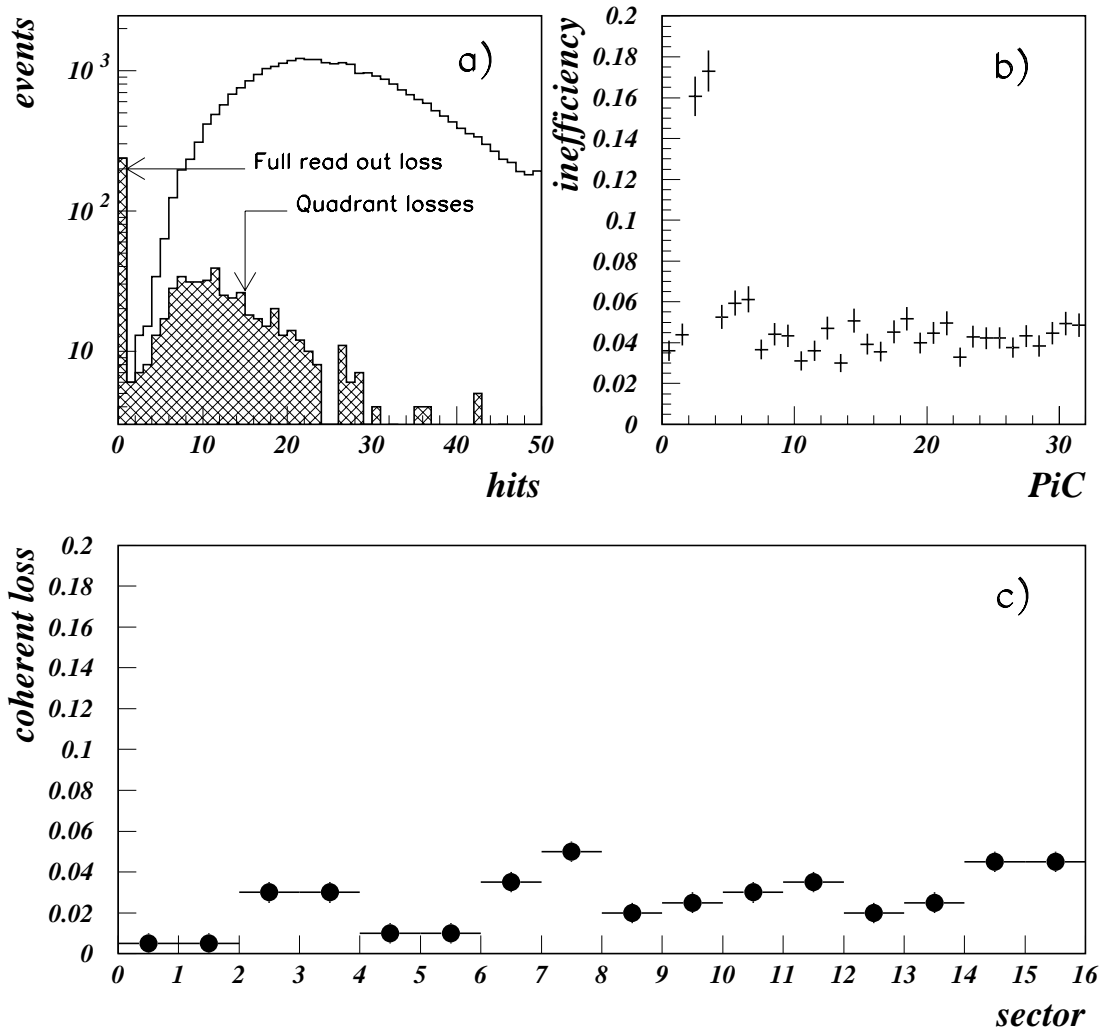


Figure 4.12: a) Distribution of the total number of hits in the BST in case when all four planes are crossed by an electron track (open histogram). The dashed histogram represents the part of events with identified coherent losses either fully or quadrant-wise (see in the text). b) Inefficiency plotted as a function of the number of the storage capacitor in the APC ("pipeline counter PiC"). Two pipeline counters out of thirty two were found to be less efficient resulting in about 0.5% of the coherent losses. The total amount of the coherent losses is presented in plot c) sector-wise.

by the online hit finding procedure. According to present understanding, a quadrant becomes “hot” or “silent” due to non-adjustable gain of preamplifiers and offset<sup>1</sup> of the analog signals on FADC’s. It results in higher risk of output amplitudes to be in overflow (for “hot” quadrant) or in underflow (for “silent” quadrant) of the FADC dynamic range. In both cases, the common mode correction and, consequently, the correct hit finding procedure are impossible.

Two pipeline counters were found to be about 15% less efficient (see Fig. 4.12,b)) because the pattern sequencer on the OnSiRoC showed occasional synchronization problems which led to sampling errors. The coherent losses in the BST amounted to about 4% in average. They were estimated sector-wise (see Fig 4.12,c)) and implemented in Monte Carlo simulation.

## 4.7 Simulation of the BST

The BST geometry corresponding to the 1997 data taking has been stored in a bank (BGAS). The dead material of the backward silicon tracker which comprises the supporting structure, front end readout electronics and the cooling system, was correctly simulated in the H1SIM program. On the simulation level it is checked whether a charged track scattered in the active volume of the BST. If yes, then the hits corresponding to this track are generated. The dead material distribution is taken into account in order to simulate the radiation processes. On the hit digitization level (H1DIGI) the simulated hits are kept according to a dead detector map written in a bank (BSSW) (see Section 4.5) and assuming the single hit efficiency to be 95% estimated from data. The noise probability of about 1.5 per mil estimated from data was used to generate fake hits. The hit positions were smeared taking into account the detector spatial resolution of 16  $\mu\text{m}$ . This information was then stored in a bank (BDSS). The simulated events were reconstructed in the same way as real data. Additional corrections related to the detector efficiencies and readout have been applied during the analysis in order to ensure a correct description of the backward silicon tracker in the Monte Carlo simulation (see Section 6.3.5).

## 4.8 Alignment

In order to benefit from the high spatial resolution, an accurate alignment of the detector planes with respect to each other as well as of the detector as a whole is obligatory. The alignment constants of the backward silicon tracker were determined from data. The applied procedure comprises two basic steps:

- **Internal alignment** of the radial positions of the 64 detectors;

---

<sup>1</sup>The gain and the offset are adjustable since 1998.

- **External alignment** of the BST with respect to the H1 coordinate system assuming that the tracker can be treated as a rigid body.

Since the internal and external alignments are correlated the procedure of the BST alignment has been performed iteratively.

### 4.8.1 Internal Alignment

For the first iteration of the internal alignment the minimization of the hit residuals has been exploited. It allowed to calculate the displacements of the detectors belonging to one sector. A further improvement of the internal alignment was achieved by focusing of the BST tracks to the vertex measured with the central tracker detectors. This has been done by re-adjusting the radial positions of the detectors.

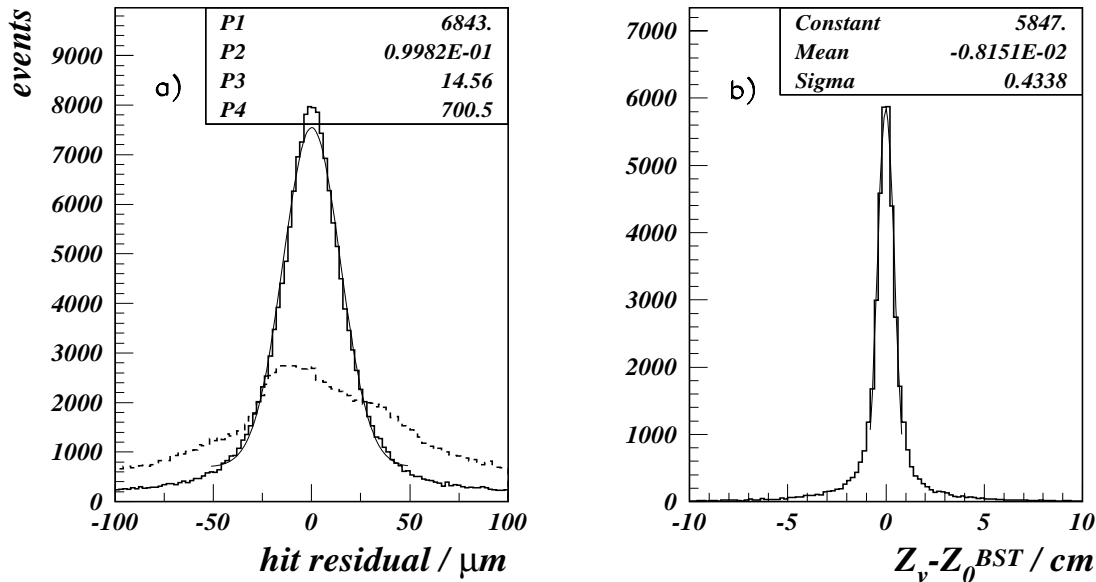


Figure 4.13: Quality of the internal alignment. a) represents the hit residuals for all 64 detectors before (dashed curve) and after (solid histogram) performing the internal alignment. b) shows the difference between the vertex measured with the central tracker detectors requiring its accuracy to be better than 0.3 cm and the one reconstructed with the BST after alignment.

The quality of the internal alignment can be demonstrated by the residuals before and after alignment presented in Fig. 4.13,a). The vertex reconstruction accuracy is shown in Fig. 4.13,b). Note that the BST geometry is not optimized for the vertex measurement. Still, a precision of about 4 mm in the  $z$ -vertex position has been obtained.

	$R_a/\text{cm}$	$\phi_a/\text{rad}$	$Z_a/\text{cm}$	$\theta_x/\text{rad}$	$\theta_y/\text{rad}$
value	0.13	-1.38	-0.29	0.0062	0.0004

Table 4.1: The BST external alignment parameters.

## 4.8.2 External Alignment

In order to measure the polar angle of the scattered electron, the BST has to be aligned with respect to the H1 coordinate system. The  $z$ -vertex position is the most precise reference coordinate for the BST since any radial displacement of the detector positions will result in the biased reconstructed vertex position multiplied with a factor  $\cot(\theta_e)$  which is 11.5 for the electron scattered at  $175^\circ$ . It has thus been utilized for the external alignment procedure.

Prior to installation the BST was measured on a 3D coordinate measurement device. It was seen that it may be treated as a rigid cylinder. This has five degrees of freedom, as is shown in the Fig. 4.14. Possible shifts of the tracker can be parameterized with three parameters  $R_a$ ,  $\phi_a$  and  $Z_a$  and its inclination with respect to the  $x$  and  $y$  axes described by two Euler angles  $\theta_x$  and  $\theta_y$ , respectively. The third Euler angle can be omitted due to the  $\phi$  symmetry of the tracker. The difference between event vertices measured with the BST and with the CTD can then be expressed in terms of these five free parameters:

$$\begin{aligned}
 Z_0 - Z_v &= R_a \cdot \cos(\phi - \phi_a) \cdot \cot \theta - Z_a && \text{translation} \\
 &+ (\theta_x \cos \phi + \theta_y \sin \phi) \cdot (Z_{rot} - Z_v) \cdot \cot \theta, && \text{rotation}
 \end{aligned} \tag{4.5}$$

where  $Z_v$  is the  $z$ -vertex position measured with the central tracking detectors and  $Z_0$  is the vertex position reconstructed with a BST track of polar angle  $\theta$ . The azimuthal angle  $\phi$  is given by the backward calorimeter SpaCal.  $Z_{rot}$  is the  $z$ -position of the BST rotation center which has been chosen at the middle of the BST active area as this gives the best decoupling between rotation and translation of the tracker.

The five free parameters in Eq. 4.5 were obtained by fitting the difference  $Z_0 - Z_v$  as a function of  $Z_v$  and  $\phi$ . This procedure has been repeated three times with improved internal alignment. The final values of the external alignment parameters are given in Table 4.1. They appear to be covered by the approximate tolerances of the BST installation.

The external alignment has to be performed prior to the second iteration of the internal alignment of the tracker components with the tracks focused on the vertex, in order to get rid of the common nonlinear effects peculiar to the tracker as a whole. This permits to reduce the internal alignment task to the simple radial translation of the detectors.

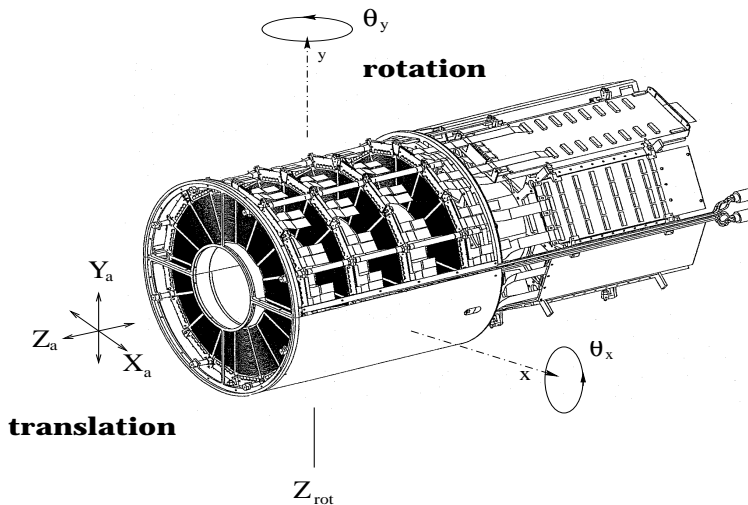


Figure 4.14: Sketch defining the global alignment parameters of the BST. The parameters  $Y_a$ ,  $X_a$  and  $Z_a$  stand for translation. A rotation of the BST is parameterized by the two Euler angles  $\theta_x$  and  $\theta_y$ . The third Euler angle is omitted due to  $\phi$  symmetry of the tracker.

### Beam Tilt Correction

The described alignment procedure of the backward silicon tracker has been performed in order to adopt its measurement of the polar angles of the tracks to the H1 coordinate system, where the  $Z$  direction is defined as the axis of the CJC. However, the beam axis does not coincide with the one of the H1 coordinate system due to beam inclination. This effect must be taken into account for the correct calculation of the polar angle of the scattered electron. The tilt of the beam axis can be determined experimentally because the  $z$  position of the interaction vertex varies up to about  $\pm 70$  cm.

The track reconstruction in the CJC [80] provides run averaged  $z$ -vertex positions. The beam tilt with respect to the H1 coordinate system is simply obtained from straight line fits to the dependences  $X_v = f_x(Z_v)$  and  $Y_v = f_y(Z_v)$ . In the analysis the beam tilt was corrected on a run by run basis with typical values of 1-2 mrad.

### 4.8.3 Alignment of SpaCal and BDC

The scattered electron cluster position in the  $x - y$  plane is defined by the weighted average over the positions of the calorimeter cells belonging to the cluster:

$$X_{cl} = \sum_{i=1}^N x_i w_i, \quad Y_{cl} = \sum_{i=1}^N y_i w_i, \quad (4.6)$$

where  $x_i$  and  $y_i$  are the geometrical centers of the cells and the weight of the cell  $i$  is defined as in [45]:

$$w_i = \frac{\max(0, w_{cut} + \ln(E_i/E_{cl}))}{\sum_{j=1}^N \max(0, w_{cut} + \ln(E_j/E_{cl}))}. \quad (4.7)$$

Here,  $E_i$  corresponds to the energy reconstructed in a cell  $i$ ,  $E_{cl}$  is the total energy deposited in a cluster and  $w_{cut} = 4.85$  defines a so-called logarithmic cut-off parameter. The  $z$  position of an electromagnetic energy cluster was parameterized depending on its energy  $E'_e$  using the Monte Carlo simulation.

The SpaCal calorimeter measures the scattered electron energy. The validation of an electron candidate cluster with a BST track link requires both detectors to be aligned with respect to each other and to the H1 coordinate system. As mentioned above, the azimuthal angle  $\phi$  of the scattered electron has been exploited in the external alignment of the BST.

In order to obtain a clean electron sample of events suitable for the alignment procedure the following cuts were applied:

1. The energy of the cluster reconstructed in SpaCal  $E'_e$  was required to exceed 20 GeV. This cut excludes photoproduction background;
2. The error of the central tracker vertex determination  $\delta Z_{vertex}$  had to be smaller than 0.3 cm;
3. The error of the track angle measured by the central trackers must be less than 2 mrad;
4. In order to reduce showering effects in front of the SpaCal, less than five tracks reconstructed in the backward drift chamber within 5 cm around the cluster center were required as suggested in [43].

The alignment of the backward calorimeter was performed using electron tracks with polar angle measured by both the central tracker and the SpaCal-Vertex combination. The alignment parameters for SpaCal were obtained by studying the difference between these two angles  $\Delta\theta = \theta_{CT} - \theta_{SpaCal-vertex}$ , as a function of azimuthal angle  $\phi_e$  measured by SpaCal (see Fig. 4.15,a)). They were calculated by fitting this dependence with a function of the following form:

$$\Delta\theta_e = P(1) \cdot \sin(\phi_e - P(2)) + P(3). \quad (4.8)$$

Here,  $P(1)$  is a radius and  $P(2)$  is an azimuthal angle shift of the SpaCal in the cylindrical coordinate system and  $P(3)$  measures the calorimeter displacement along the  $z$ -axis. The resulting parameters for correction of the SpaCal position are given in Table 4.2. Fig. 4.15,b) shows that after corrections the differences in the  $\theta$  measurements are removed. The differences between the  $\phi_e$  measurements performed with the CJC and with the SpaCal after alignment are shown in Fig. 4.15,c). It is seen, that

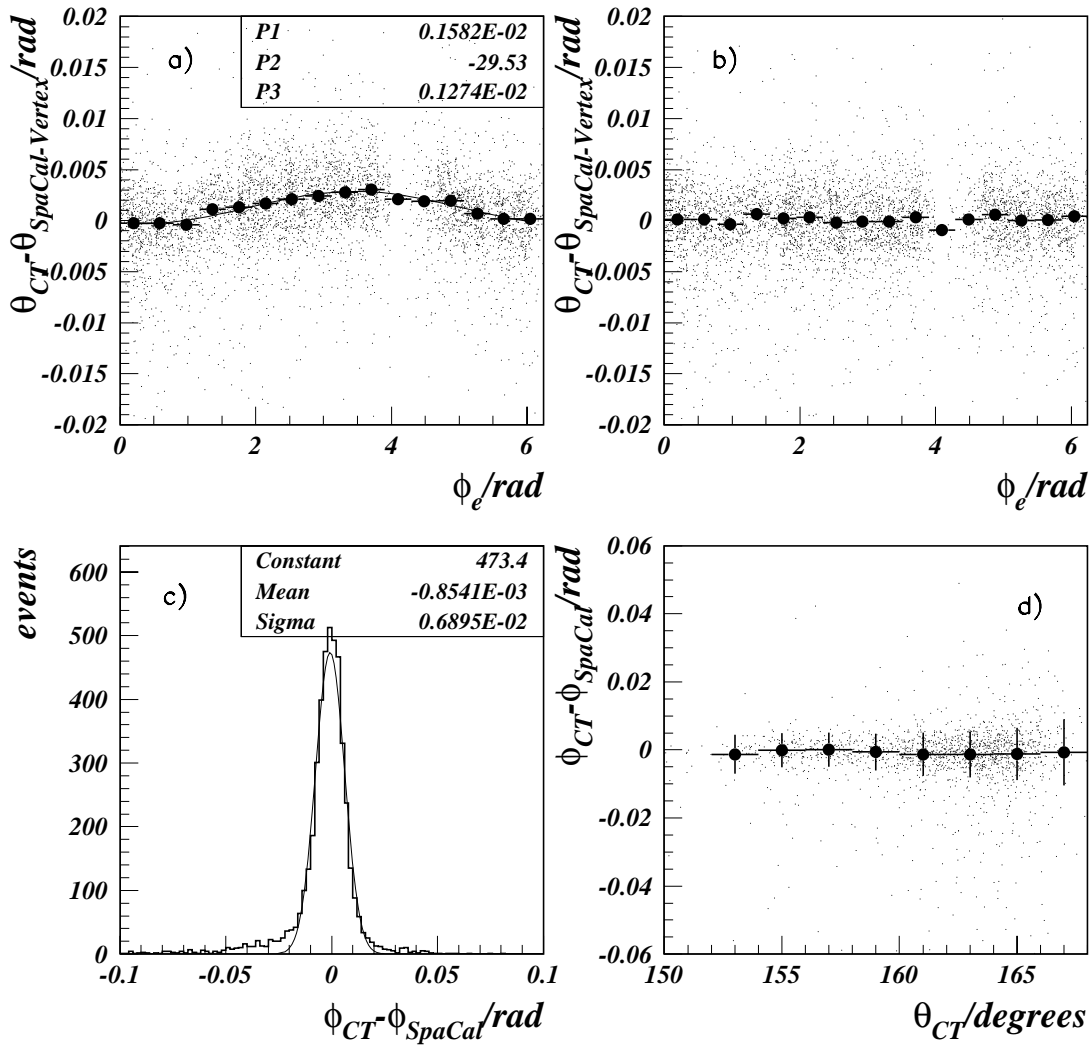


Figure 4.15: Difference of the scattered electron polar angle measured with the central trackers and SpaCal-vertex combination as a function of azimuthal angle  $\phi_e$  measured by SpaCal before alignment (a) and after alignment (b). Solid circles with error bars represent the mean values and their statistical errors of Gaussian fits performed in  $\phi_e$  slices. Plot c) displays the matching between the azimuthal angle  $\phi_e$  measured by central trackers and the backward electromagnetic calorimeter after alignment. Its dependence on the polar angle  $\theta_e$  is presented in plot d) where the solid circles with error bars represent the mean values and the spread of Gaussian fits performed in  $\theta_e$  slices.

	$\Delta X/\text{cm}$	$\Delta Y/\text{cm}$	$\Delta Z/\text{cm}$
SpaCal	+0.28	+0.07	-0.7
BDC	+0.27	+0.31	+1.5

Table 4.2: The alignment parameters for SpaCal and BDC with respect to the nominal positions for the special run period 1997.

the resulting SpaCal measurement of the azimuthal angle is unbiased over the whole calorimeter acceptance range (see Fig. 4.15,d)).

The backward drift chamber was not mounted on the SpaCal calorimeter in 1997. It thus had to be aligned independently. The BDC provides a cross check for the BST alignment with respect to the backward part of the H1 detector. The study of the residual dependence of  $\Delta\theta$  between the polar angle measured with BST and the one measured with BDC on the azimuthal angle  $\phi_e$  is used for estimating the systematic error of the polar angle measurement of the scattered electron. Since the  $\phi_e$  resolution of the BST and of the BDC is poor due to their small azimuthal granularity, the backward calorimeter was always used to measure this quantity.

The alignment of the backward drift chamber was performed by the same procedure as the one for SpaCal. In contrast to the backward calorimeter alignment, where the vertex position had to be required for the calculation of the polar angle of a track, the BDC can measure it itself.

Fig. 4.16,a) displays the measured  $\Delta\theta$  difference between the central trackers and the backward drift chamber as a function of  $\phi_e$  after applying the geometrical corrections given in Table 4.2. The distribution shows no evidence of the BDC displacement with respect to H1 coordinate system. The internal consistency between the SpaCal alignment and the one of the BDC is shown in Fig. 4.16,b).

Note, that the external alignment of the backward instrumentation has been performed with respect to the central trackers and not with respect to each other. Thus, consistent results in the polar angle measurements between the different subdetectors prove the correctly performed alignment procedure. Fig. 4.16,c) demonstrates very good agreement between the  $\theta_e$  measurement made with the BST and the one made with the BDC.

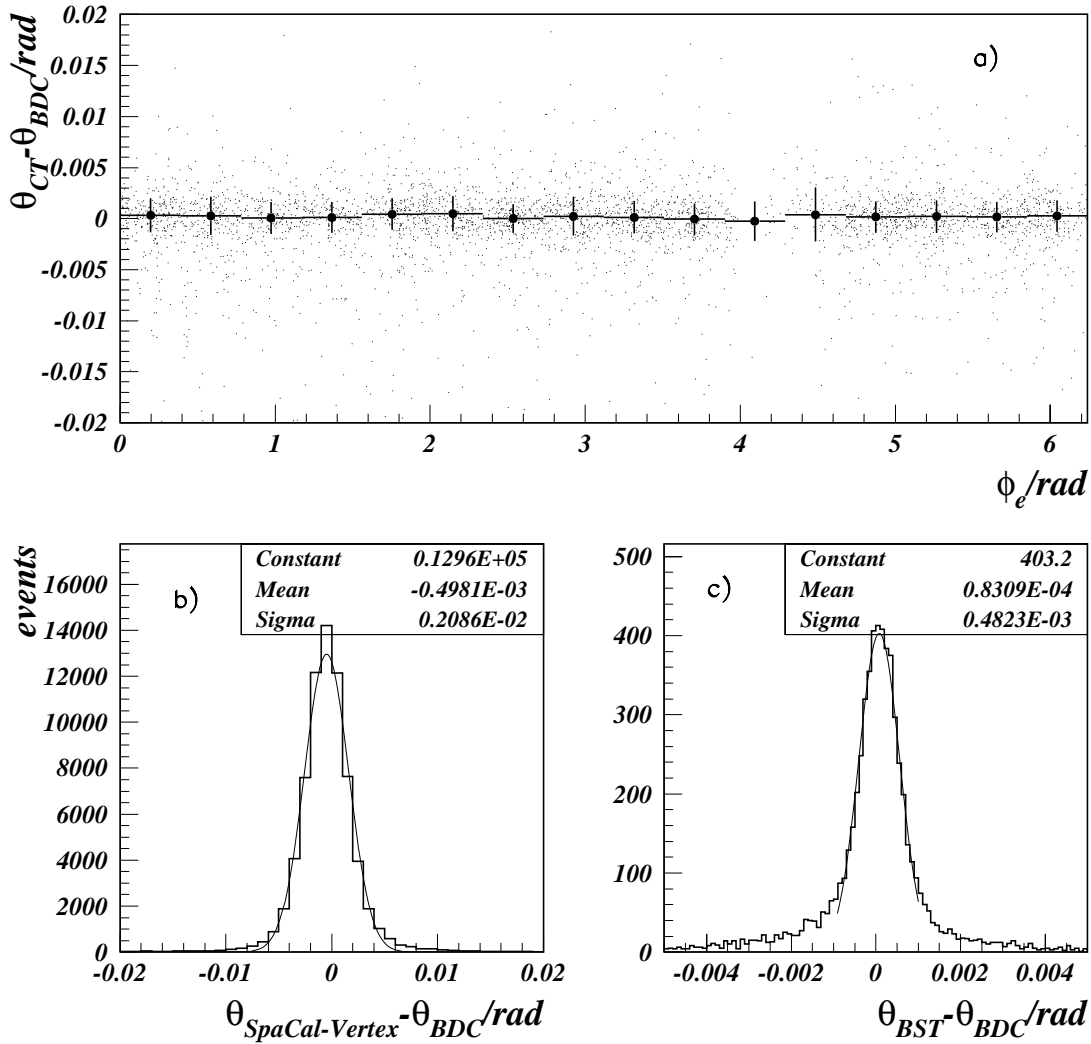


Figure 4.16: a) Difference of the scattered electron polar angle measured with the central trackers and with the BDC as a function of the azimuthal angle  $\phi_e$  after alignment. Solid circles with error bars on plot a) represent the mean values  $\Delta\theta$  with their statistical errors of the Gaussian fit performed in  $\phi_e$  slices. Matching of the scattered electron polar angles measured with the SpaCal-vertex combination and with the BDC is visible in Fig. b). Fig. c) illustrates the matching of the scattered electron angle measurements with the BST and the BDC for the case when a track in the BST was reconstructed from four hits. All three plots were made when no showering occurred in front of the BDC.

# Chapter 5

## Energy Calibration

The reconstruction of the kinematic variables is based on the use of both pure electromagnetic and pure hadronic variables  $y_e$  and  $y_h$  (see Section 3.3, Eqs. 3.8 and 3.10) which in the  $\Sigma$  method are combined to define  $y_\Sigma$  (Eq. 3.12). Thus, the measurement of the inclusive deep-inelastic scattering cross section depends on the reconstruction of the final state electron energy and of the energy of hadronic final state particles and, hence, demands a precise calibration of the H1 calorimeters. This concerns the calibration of the electromagnetic and hadronic energy scale of the SpaCal (Section 5.1) and of the LAr (Section 5.2) calorimeters.

For the LAr calorimeter, only the hadronic energy scale is covered in this chapter since the present analysis is devoted to the low  $Q^2$  kinematical region where the scattered electron energy is measured with the SpaCal. The extension of the kinematic range to large  $x$  due to the measurement of the scattered electron polar angle and the vertex reconstruction at low  $Q^2$  with the BST, allowed the forward part of the LAr calorimeter to be better calibrated than previously. Different methods have been exploited and compared in order to achieve a high accuracy of the hadronic energy reconstruction in the liquid argon calorimeter.

### 5.1 Backward Calorimeter (SpaCal) Calibration

Event kinematics reconstruction is based on measurement of the final state electron at  $y > 0.15$ . Resolution in the kinematic variables  $x, y$  and  $Q^2$  calculated with the electron method (see Section 3.3) depends largely on the energy measurement of the scattered electron. Thus, a calibration of the backward calorimeter is demanded as precise as possible.

#### Electromagnetic Energy Scale

The initial energy calibration of the SpaCal has been obtained by exploiting a special LED system [81, 82] which provides amplification gains for 1192 photomultiplier

tubes based on light signals collected in each calorimeter cell. The amplification gains are time dependent. They are used for the SpaCal energy reconstruction on level 5 of the H1 data reconstruction chain. Several independent methods were proposed to tune the SpaCal electromagnetic energy scale. These used cosmic muons [83], beam halo muons [84], the kinematic peak shape [85, 86] and “Double Angle” [52] calibrations. The kinematic peak shape cell-dependent calibration has been used to pre-calibrate the inner region of the SpaCal ( $R_{SpaCal} < 50$  cm) which has large statistics. The outer region was pre-calibrated with cosmic muons. The most accurate method for the calibration of the SpaCal electromagnetic energy scale is the double angle method which expresses  $E'_e$  by the two angles  $\theta_e$  and  $\theta_h$ . The double angle calibration has been finally applied to data and simulated events during the offline analysis. A comparison of the electromagnetic energy scale of data and simulations based on two different theoretical models (ARIADNE and LEPTO) did result in an estimate of the SpaCal electromagnetic scale uncertainty of 0.3% for energies above 17 GeV [87]. At lower energies the double angle method becomes less accurate and the event sample affected by background events. From studies of QED Compton events the energy scale was determined to  $\pm 2\%$  [88] at 2 GeV. The error was treated as a linear function of  $E'_e$  interpolating between the results at 2 GeV and 17 GeV.

### Hadronic Energy Scale

The SpaCal response on single particles was tested in test beam experiments and tuned in the framework of the H1 simulation [89]. The corrections to the SpaCal hadronic energy scale were initially estimated in a Monte Carlo study yielding values of 1.1 (1.3) for the electromagnetic (hadronic) SpaCal, respectively [90]. These correction factors were applied for both Monte Carlo simulation and data to the energy scale of all cells apart from those belonging to the electron candidate cluster. Further checks have been performed using  $ep$  data. Two independent analyses of the SpaCal response to the hadronic final state particles have been carried out in order to obtain its absolute hadronic energy scale. The first investigation, presented in [91], was based on the demand that the inelasticity  $y_h$  measured with the hadronic final state be in average balanced with  $y_e$  reconstructed with the final state electron, i.e.  $\langle y_h/y_e \rangle = 1$ . The second study presented in [37] was concentrated on a comparison of the hadronic energy description with the momentum measurement of charged particles using the central jet chambers. Both analyses yielded a correction factor of 1.5 to the energy of the hadronic final state measured in the SpaCal for both data and Monte Carlo simulation. An additional factor of 1.07 was applied to the hadronic energy deposited in electromagnetic and hadronic parts of the SpaCal calorimeter in the data as a result of an analysis performed with the bulk 1997 data [92]. That was the starting scale of the SpaCal hadronic energy in the data sample taken in the so-called minimum bias run in autumn 1997 which is analyzed in this work.

The SpaCal hadronic energy scale has been studied with  $ep$  DIS events having high values of the inelasticity  $y_h$ . The SpaCal contribution to the total hadronic energy is kinematically enriched for high  $y$  since the hadronic energy flow is directed to the backward part of the H1 detector. Thus, events with  $y_e > 0.3$  were selected. Here, it is important to notice that  $y_e$  does not depend on the hadronic energy scale. A

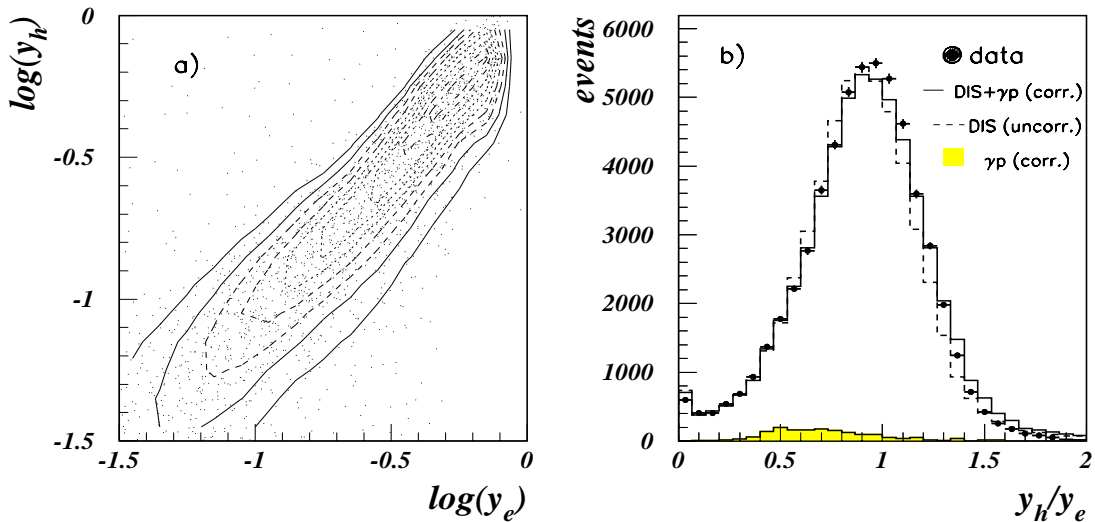


Figure 5.1: Contour lines in figure a) illustrate the correlation between  $y_h$  and  $y_e$  plotted for data. Figure b) shows the ratio  $y_h/y_e$  for data (closed circles) and for Monte Carlo simulation before (dashed line) and after (solid line) applying a correction factor of 1.06 (see text).

correlation between  $y_h$  and  $y_e$  is found as presented in Fig. 5.1,a) by the contour lines in the kinematical range  $0.03 < y_e < 0.8$ . It can be seen from this picture that the ratio  $y_h/y_e$  is constant independently of the imposed cut on the  $y$  region.

The absolute hadronic energy scale of the SpaCal is checked using the precisely calibrated electromagnetic one as a reference scale. The ratio  $y_h/y_e$  for  $y_e > 0.3$  is depicted in Fig. 5.1,b) before (dashed histogram) and after (solid histogram) correction. A correction factor of 1.06 had to be applied to the hadronic energy scale in Monte Carlo simulation as for the data. As can be seen, good agreement between data and simulation was obtained. This point is particularly important since the DIS events selection exploits the cut on  $E - P_z > 35$  GeV (see Section 6.3) and since the LAr calibration presented in the next section involved also the SpaCal hadronic final state measurement.

## 5.2 Calibration of the Liquid Argon Calorimeter

The reconstruction of the event kinematics at large  $x$  is based on the hadronic variables such as  $P_t^{had} = \sum_h E_h \sin \gamma_h$  and  $\Sigma = \sum_h E_h (1 - \cos \gamma_h)$  introduced in Section 3.3. The summation in these formulae is performed over all hadronic final state particles. In practice, the energies deposited by these particles in all cells of the H1 calorimeters are summed up, weighted with their angles.

The fluctuations of hadronic energy deposited in the LAr cells by low momentum particles are increasing as  $\sim 50\%/\sqrt{E}$  with decreasing energy. On the contrary, the momentum and thus energy resolution of the trackers improves due to a factor  $\sim E$ . This makes the use of tracking devices more preferable for low momentum particles rather than the calorimeters. A special procedure (FSCOMB) has been developed in order to divide the calculation of  $P_t^{had}$  and  $\Sigma$  between the LAr calorimeter and the central tracker detectors [93, 94]. Tracks were selected with reconstructed momenta less than 2 GeV. The selected tracks are extrapolated to the LAr surface and linked to a cluster<sup>1</sup>. If the energy in the LAr cluster behind the track is greater than that of the track momentum, the calorimetric information is used. If a track does not reach the calorimeter surface, the track momentum is also used. Cells of the LAr calorimeter belonging to a cluster, a track is linked to, are masked, i.e. they are not used in the hadronic summation thus excluding a double counting of energies. As a result, the low momentum charged particles are better treated and the hadronic energy scale is determined more accurately than in the case of the calorimetric measurement only. The reconstruction of the hadronic variables is then determined by non-linked high energetic LAr calorimeter cells, tracks and the hadronic energies measured in the SpaCal. The noise contribution to the hadronic measurement must be subtracted in order not to bias the reconstruction of kinematic variables. Thus one finds

$$\Sigma = \Sigma_{LAr} + \Sigma_{Track} + \Sigma_{SpaCal} - \Sigma_{Noise}, \quad (5.1)$$

$$P_t^{had} = P_t^{LAr} + P_t^{Track} + P_t^{SpaCal} - P_t^{Noise}. \quad (5.2)$$

The main systematic error of the DIS cross section measurement for  $y < 0.1$  comes from the uncertainty of the hadronic energy scale which has to be calibrated as good as possible. The DIS cross section measurement requires not to describe the absolute energy scale but its variation relative to the Monte Carlo simulation. Therefore, all relevant aspects of the H1 calorimetry and the hadronic final state must be well reproduced.

The hadronic energy scale of the LAr modules has been predetermined with experiments using pion beams with energy from 3 to 205 GeV [95]. The H1 LAr calorimeter is not compensating. Its response to hadrons is typically 30% smaller than that for electrons of the same incident energy. As a consequence, an additional correction known as “weighting technique” has to be applied to the electromagnetic scale in order to obtain a proper hadronic energy scale. The idea of this method is based on the fact that the highly granulated LAr calorimeter allows effectively to separate the cells with the absorbed energy of electromagnetic origin, characterized by the highly dense energy deposition, from those with energy of hadronic origin which is much more spread out. The weighting technique works well for hadronic energies above 10 GeV. For those clusters whose energy is below, simple multiplicative factors corresponding to effective  $e/\pi$  ratios have been applied [96].

---

<sup>1</sup>Energy in a cylinder with  $R = 25(50)$  cm around the track impact point in the electromagnetic (hadronic) sections.

As a result of these test beam experiments, the response of the LAr wheels to a single hadron has been described within 5% accuracy.

The input to the present analysis are the output parameters of the H1 event reconstruction program which performs the following procedures [97]:

1. Calibration of the absolute electromagnetic and hadronic energy scales with the calibration constants (one per stack type) obtained in the test beam runs.
2. Simulation of the electronic noise obtained from special runs without zero suppression and with a random trigger.
3. Clustering of the LAr cells which passed the online noise cut. Electromagnetic showers are most probably collected in one cluster whereas the hadronic ones are usually split into several clusters.
4. Further noise suppression by excluding cells which can not be associated to any cluster within a sphere with a radius of 50 cm from its gravicenter.
5. Correction for energy losses in dead material and in the calorimeter crack regions.

An additional suppression of the electronic noise and backscattering of forward particles (e.g. off the collimators) has been used on top of the standard procedure. The selected cells were checked on the energy deposited in a sphere with a radius 40 cm (central part) and 20 cm (forward part) around the beam tilt corrected cell position. If the total energy deposited in a sphere is less than 0.4 GeV for the central part and less than 0.8 GeV for the forward part, the cells were dropped.

### 5.2.1 LAr Calibration with the “Lagrangian” Method

The final fine tuning of the hadronic calibration constants has been performed with the real and simulated data. Contrary to the situation with the SpaCal, the hadronic energy flow in the LAr direction is rather collimated into jets. Yet, it is practically impossible to select well single hadrons for a precise check of the hadronic energy scale of the LAr calorimeter. Instead, the LAr response on the hadronic final state is studied using global event quantities, such as the transverse momentum of the hadronic final state ( $P_t^h$ ) and of the final state electron ( $P_t^e$ ). The calibration of the hadronic energy scale of the LAr calorimeter is based on the assumption of transverse momentum conservation:

$$P_t^h + P_t^e = \Sigma_h E_h \sin \gamma_h + E_e' \sin \theta_e = 0. \quad (5.3)$$

The  $P_t$  balance method is insensitive to particle losses in the extreme forward and backward directions connected with the proton remnant jet and photon radiation.

The final calibration was obtained using the least square method of minimizing the difference between the transverse momenta of the well calibrated final state electron and

of the final state hadrons projected on the electron direction. The following functional was minimized:

$$L = \sum_{i=1}^{N_{events}} \sigma_i^{-2} \left( P_t^e - [P_t^{Track} + P_t^{SpaCal} - P_t^{Noise}] - \sum_{j=1}^M P_t^j \alpha_j \right)^2. \quad (5.4)$$

Here,  $P_t^e$  is the transverse momentum of the electron,  $P_t^{Track}$  and  $P_t^{SpaCal}$  are the transverse momenta of the final state hadrons measured with CJC and SpaCal, respectively. The transverse momentum faked by the noisy cells is represented by the term  $P_t^{Noise}$ . Here, it is important to notice that the projection on the electron direction makes the method less sensitive to the noise since it is distributed isotropically over the azimuthal angle. Even if the noise suppression procedure removes some signal, the most important is that this must be described by the Monte Carlo simulation down to lowest possible  $y$  (see Fig. 5.2). The second summation in Eq. 5.4 is performed over certain

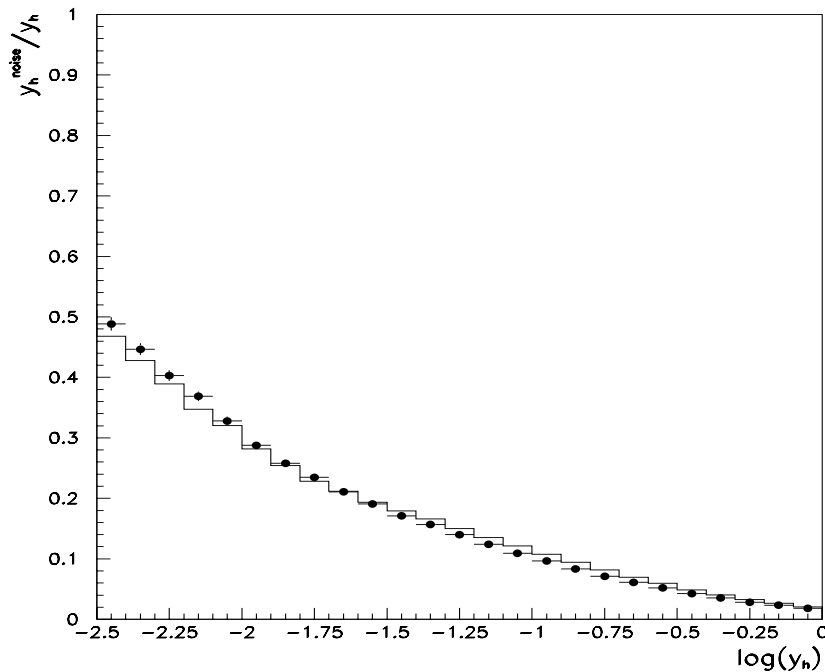


Figure 5.2: Contribution of the electronic noise of the LAr calorimeter to the reconstructed  $y_h$  as a function of  $y_h$ . Closed points present data and the histogram illustrates the Monte Carlo simulation.

modules of the LAr calorimeter introducing calibration constants  $\alpha_i$  to be determined by minimizing the functional. For the low  $Q^2$ , high statistics data, the summation in Eq. 5.4 extends over the 8 octants and 8 wheels of the LAr calorimeter. This is called *octant-wise* calibration. For high  $Q^2$  data suffering from lack of statistics the summation extends only over the 8 wheels determining only 8 constants  $\alpha$ . This is termed *wheel-wise* calibration.

For simplicity the resolutions  $\sigma_i$  were set constant. This was proposed by the observation that the calibration results did not depend on the  $P_t$  range [99].

The requirement

$$\frac{\partial L}{\partial \alpha_j} = 0 \quad (5.5)$$

defines a system of  $k = 1, \dots, M$  linear equations for  $M$  modules:

$$\sum_{i=1}^{N_{events}} P_{t,h}^{ik} \cdot \left( P_{t,e}^i - \alpha_k \cdot \sum_{j=1}^M P_{t,h}^{ij} \right) = 0, \quad (5.6)$$

where  $P_{t,e}^i = P_t^e - [P_t^{Track} + P_t^{SpaCal} - P_t^{Noise}]$  of event  $i$ . Using matrix techniques this equation can be solved to determine the energy scale factors  $\alpha_k$  for all modules  $k$ .

While the division of the hadronic variable calculation into “tracks+cells” is advantageous for the resolution, it removes almost half of the low energetic clusters produced in the central part of the calorimeter from the energy sum which is provided by the linked tracks. In this procedure the forward LAr is left “untouched” since it is out of the CJC acceptance. Because of the correlation between the weights of the energy scales of the LAr modules in the global minimization procedure, no tracks were considered in the calibration procedure, i.e. the hadronic measurement was made only with the LAr calorimeter. This provided a most accurate determination of the calibration constants for the central calorimeter part<sup>2</sup>. Indeed, once the LAr calorimeter is calibrated, one is free to choose a  $y_h$  composition scheme giving optimum results for kinematic reconstruction.

An unambiguous identification of the scattered electron is of prime importance for the calibration procedure. There are two possible cases leading to a misidentification of the scattered electron:

1. Photoproduction background. This source of electron misidentification has been suppressed by requiring the energy of the most energetic SpaCal cluster to be larger than 10 GeV and the  $E - P_Z$  to be above 35 GeV (for details see Section 6.4);
2. A high energetic hadron might be wrongly identified as a scattered electron. In order to exclude that case, the jet angle, reconstructed with the scattered electron measured in the SpaCal (see Eq. 3.7), had to be limited to the LAr calorimeter acceptance (see Fig 5.3,a).

Reconstruction of the scattered electron transverse momentum ( $P_t^e = E'_e \sin \theta_e$ ) has been performed by measuring its energy with the precisely calibrated SpaCal electromagnetic calorimeter and its polar angle with the backward drift chamber and the BST. The interaction vertex was reconstructed by the central trackers. A new important feature of this analysis is the extension of the kinematic range towards large  $x$

---

<sup>2</sup>A comparison of the relative change of the hadronic energy scale between data and simulation, described in Section 5.2.2, proves that both approaches give the results which are well within  $\pm 2\%$  of the systematic uncertainty (see Fig. 5.9). Comparison of the DIS cross sections obtained with the two calibrations supported this conclusion.

where the vertex was reconstructed with the BST. This point is especially important since that allowed to study the response of the forward part of the LAr calorimeter with improved reliability.

Special attention must be given to the forward part of the LAr calorimeter due to a number of effects distorting the hadronic measurement. The main problems here are due to losses of final state hadrons in the forward beam direction and to leakage of the hadronic shower developing close to the edges of the IF1 and IF2 calorimeter modules. A way to suppress such kind of losses is to apply a cut on the polar angle of the current jet calculated using the electron measurement only (see Eq. 3.7),  $\gamma_e > 5^\circ$ , corresponding to the lower limit of the LAr calorimeter acceptance. Furthermore, a  $P_t$  balance cut was imposed as shown in Fig. 5.3,a). A cut on  $\gamma_e < 150^\circ$  corresponds to the upper angular acceptance of the LAr calorimeter for the nominal  $z$ -vertex position.

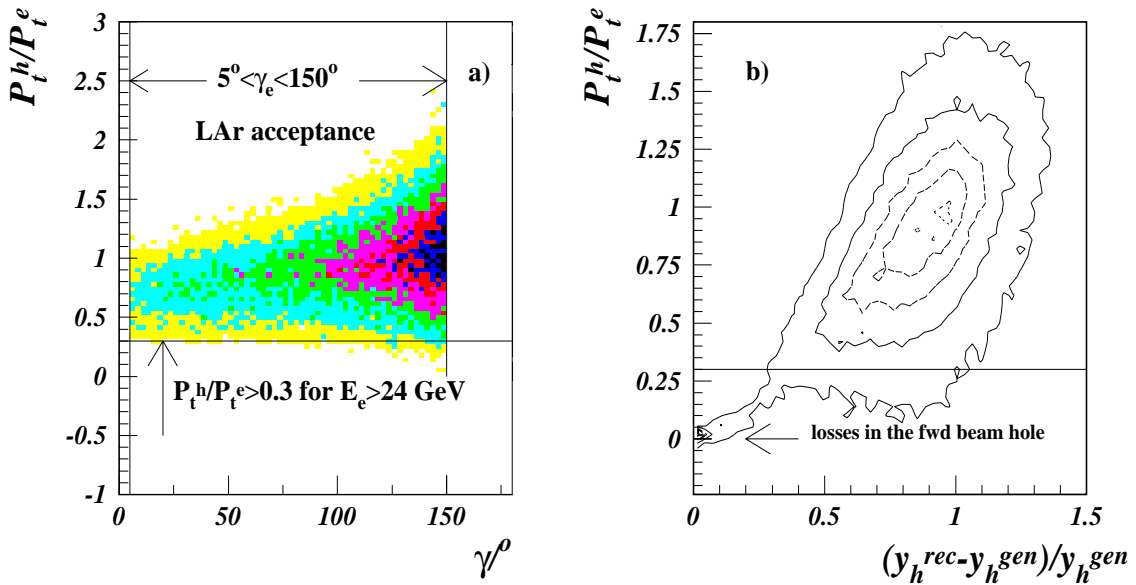


Figure 5.3: a) Some of the cuts imposed to select an event sample with minimized losses or leakage of hadronic energy due to limited acceptance of the LAr calorimeter. Contour lines in figure b) indicate the correlation between the  $P_t$  balance ( $P_t^h/P_t^e$ ) and the  $y_h$  reconstruction. The solid line represents the  $P_t$  balance cut which suppresses the energy losses in the forward beam direction.

The transverse momentum and the  $E - P_z$  of the hadronic final state can be expressed by the current jet energy and its polar angle via  $P_t^{had} = E_j \sin \theta_h$  and  $\Sigma = E_j(1 - \cos \theta_h)$ . It is obvious that both variables suffer from energy losses in a similar way. This can be seen in Fig. 5.3,b), where  $y_h$  is calculated as  $\Sigma/2E_e$ . The  $P_t$  balance cut is seen to effectively reject events with large energy losses in the forward direction. A detailed analysis of the  $P_t$  balance cut applicability at H1 is discussed in Section 6.3.

The calibration of the hadronic energy scale of the LAr calorimeter has been performed for all its 120 (64 electromagnetic and 56 hadronic) modules using the LAr

hadronic final state measurement only, i.e. without replacing central low energy depositions by their linked track momenta. Calibration constants obtained for data and Monte Carlo are presented in Fig. 5.4. Even after applying a fiducial cut preventing large energy losses in the forward part of the LAr calorimeter, the calibration constants for the IF2 module show a striking difference between data and Monte Carlo simulation (see Fig. 5.4,top). This indicates that the IF2 module response and possibly the hadronic shower development are not correctly described by the simulation. An attempt has been made [98] to solve this problem by treating IF2 and IF1 as one single module. Fig. 5.4,bottom shows that the agreement between data and Monte Carlo simulation became significantly better. Nevertheless, a difference still remains. For the electromagnetic part of the LAr calorimeter the calibration constants for the Monte Carlo simulation overshoot the ones for data by about 3% on average apart from the IF part where the calibration constants for data overshoot the ones for simulation by about 8%. The situation becomes opposite for the hadronic part of the LAr where the calibration constants for Monte Carlo are on average by 10-20% lower than those for data. Taking into account that the hadronic part of the LAr calorimeter contributes only 10-15% to the total hadronic energy, one gets a 1-3% influence on the hadronic energy scale uncertainty coming from the hadronic modules of the LAr calorimeter. The positive difference between data and Monte Carlo for the calibration constants in the hadronic part of the LAr compensates the negative one for the electromagnetic part. The relative variations in the hadronic energy scale between data and Monte Carlo remain basically within  $\pm 2\%$  as can be seen in Fig 5.5,a-d). The exception is the forward part of the LAr calorimeter where the difference between data and simulated hadronic energy scales rises up to 4% which is included in the systematic uncertainty of the DIS cross section calculation.

The Lagrangian method for the LAr hadronic energy scale calibration gives a solution for calibration constants which forces the total  $P_t$  balance to be at unity (see Fig. 5.5,e) ) but it does not enforce the unity for every part of the LAr calorimeter. The  $P_t$  balance dependence on the hadronic angle for data and for Monte Carlo is presented in Fig. 5.5,a) which shows that the peak positions of the  $P_t$  balance deviates from unity along the hadronic angle but this behavior is described by Monte Carlo simulation. However, a mean value of the  $P_t$  balance of about 0.98 is obtained. It shows no dependence on the transverse momentum of the final state electron, see Fig. 5.5,c). The  $P_t$  balance dependence is well described by the Monte Carlo simulation within  $\pm 2\%$ . This can be seen in Fig. 5.5,d).

The final state electron transverse momentum  $P_t^e$  serves as a reference scale for the hadronic final state kinematic parameters. However, the event kinematic reconstruction for  $y < 0.15$  proceeds with the hadronic  $E - P_z$  which has no direct reference scale since the  $E - P_z$  resolution of the scattered electron worsens with decreasing  $y$  drastically due to a factor  $\sim 1/y$ . A study of the event reconstruction quality, thus, solely relies on the Monte Carlo simulation. This is the reason why careful attention has been drawn to a correct description by the Monte Carlo simulation not only of the peak positions of  $P_t$  balance but also its shape in the whole kinematical region the present analysis has been carried out. In this sense, the  $P_t$  balance description plays a role of a reference

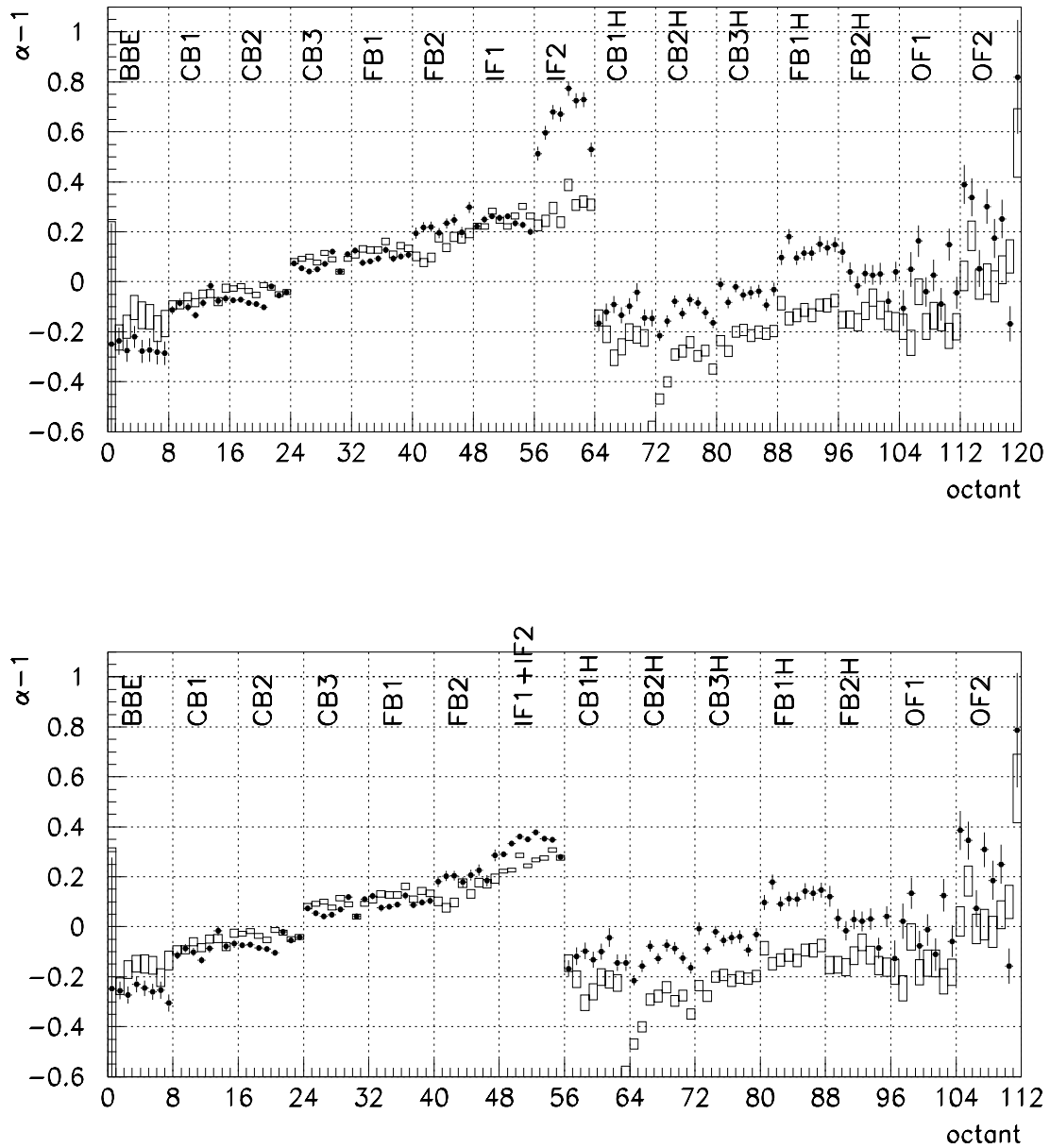


Figure 5.4: Top: calibration constants for the LAr hadronic energy scale (see Eq. 5.6). Significant difference between the constants in data (closed circles) and Monte Carlo simulation (open boxes) for the IF2 wheel has been reduced by combining it with the IF1 wheel situated in front of IF2 (Bottom). The rising behavior of the  $(\alpha-1)$  constants versus octant number is due to an auxiliary weighting function.

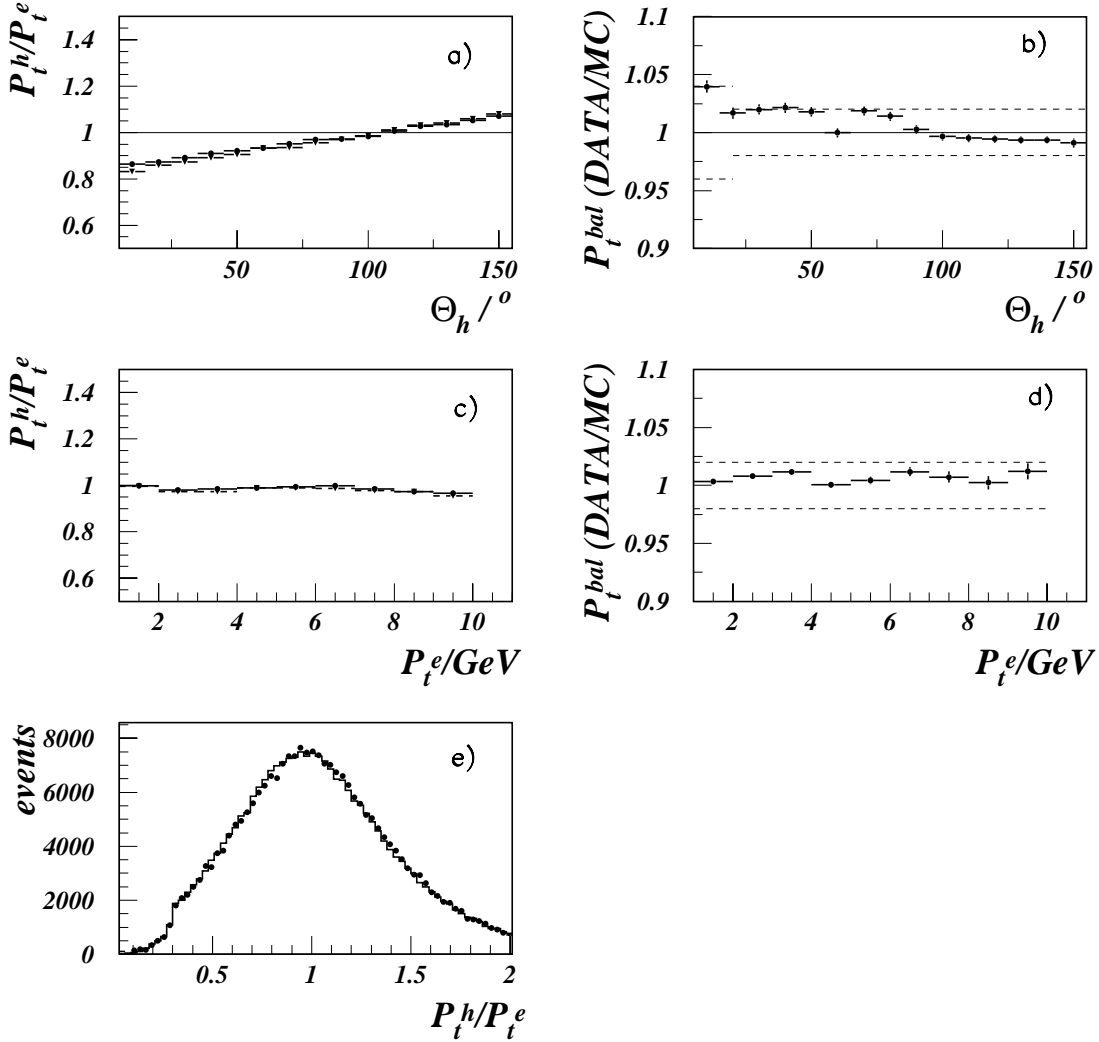


Figure 5.5: Control plots for the LAr calibration with the Lagrangian method. Mean values of the  $P_t$  balance as a function of  $\theta_h$  (a) and  $P_t^e$  (c) for data (closed circles) and Monte Carlo (closed triangles). The corresponding ratios of the mean values between data and Monte Carlo are presented in figures b) and d). Dashed lines in figure b) represent the suggested systematical uncertainty of 2% for backward and central parts of the LAr calorimeter and of 4% for the forward one. The dashed lines in figure d) show that the mean data to Monte Carlo  $P_t$  balance ratio is well within 2% variations independently of the transverse momentum of the final state electron. Figure e) represents the shape of the  $P_t$  balance which is very well described by Monte Carlo simulation, and both distributions are peaked at unity.

check to ensure the simulation of the LAr calorimeter response on the hadronic final state particles corresponds to the data.

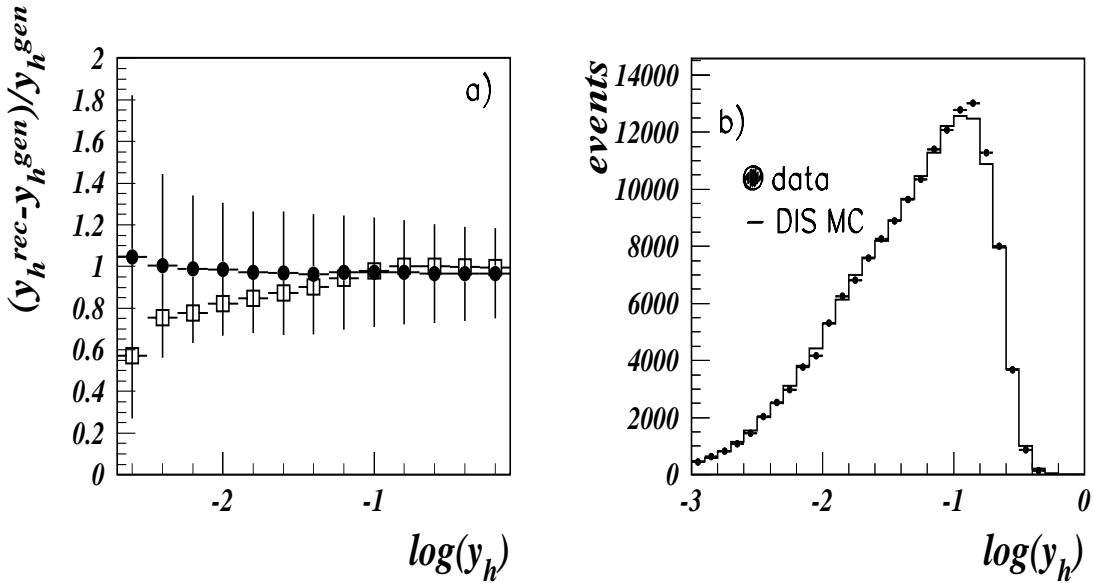


Figure 5.6: a) Comparison of  $y_h$  reconstruction before (open boxes) and after (closed circles) LAr calibration. The error bars represent the mean values and their statistical error (spread) obtained from Gaussian fits performed to the quantity  $(y_h - y_{gen})/y_{gen}$  in slices of  $y_{gen}$  for uncalibrated (calibrated) case. The  $y_h$  resolution is seen to degrade to unacceptably large values at  $\log(y_h) < -2.5$  with a fixed  $\log(y_h)$  bin width. b)  $y_h$  distribution for data (closed points) and Monte Carlo (histogram) after performing the calibration of the LAr hadronic energy scale and imposing the  $P_t$  balance cut (see in the text).

A comparison of the  $y_h$  reconstruction between the cases before and after calibration of the LAr calorimeter is shown in Fig. 5.6,a). Major improvements have been achieved in the low  $y$  kinematical region where the original hadronic energy scale calibration (open boxes) was leading to up to 20-40% deviations of the reconstructed  $y_h$  from the generated one. The situation has been improved after the  $P_t$  balance calibration described above (closed circles). The reconstructed  $y_h$  shows no significant deviation from its true, i.e. generated value in a wide kinematical range. However, the  $y_h$  resolution which is about 25-30% down to  $y \approx 0.01$  starts to worsen rapidly towards lower values, reaching more than 80% at  $y = 0.002$  for the chosen bin size. The degradation of the  $y_h$  resolution at low  $y$  is caused by more prominent hadronic energy fluctuations and increased sensitivity to electronic noise. Due to this fact, an analysis cut has been made on  $\log(y_h) = -2.5$ . This represents an extension from the previous minimum  $y$  value of 0.01 to 0.003. Still, a special study of *purity* and *stability* (see Section 6.2) of the event kinematic reconstruction is required to define bin sizes in the  $(x, Q^2)$  kinematical plane for the double differential cross section measurement in order to adapt the bin widths to the  $x$  resolution.

The resulting  $\log(y_h)$  distribution is presented in Fig. 5.6,b) showing no systematic

trend in deviations between data and simulation down to very low values of  $y_h$ . The shape of the distribution is well reproduced by the simulation.

## 5.2.2 Cross Check with the Iterative Method

Another method of the  $P_t$  balance calibration of the LAr calorimeter hadronic energy scale has been used for cross checking purposes. This method is based on the iterative adjustment of the calibration constants determined for each module<sup>3</sup> of the LAr calorimeter. The adjustment proceeds with evaluating the calibration factor for each module exploiting the ratio  $P_t^h/P_t^e$  of each event weighted with the fraction of  $P_t^h$  carried by the module  $k$ :

$$w_k^{ev} = \frac{P_{t,h}^k (1 + \alpha_k^{it})}{\sum_k P_{t,h}^k (1 + \alpha_k^{it})}. \quad (5.7)$$

Here,  $it$  denotes the number of the iteration. The calibration constants  $\alpha_k^{it}$  are obtained from the Gaussian fit to the distribution of the  $P_t$  balance as a function of the LAr calorimeter modules. A ‘‘miscalibration’’ for each module was defined as the deviation from unity of the  $P_t$  balance mean value. The calibration constants for a next iteration are obtained from the following relation:

$$\alpha_k^{it+1} = \alpha_k^{it} + \left( 1 - w_k^{ev} \cdot \frac{\sum_k P_{t,h}^k (1 + \alpha_k^{it})}{P_t^e} \right). \quad (5.8)$$

For the first iteration the constants  $\alpha_k^0$  were set to zero. The iteration procedure stops when  $\sum_k (\alpha_k^{it+1} - \alpha_k^{it})^2 < 0.002$ . The calibration procedure normally requires 5 (8) iterations for Monte Carlo simulation (data) until the mean value of the  $P_t$  balance reaches unity in all regions of the detector.

The high statistics at low  $Q^2$  allows in principle to perform an octant-wise iterative calibration of the LAr calorimeter. Yet in this case, the calibration procedure failed to converge due to some  $\phi$  peculiarities in the IF2 octants whose perturbation is spread over the whole LAr calorimeter due to correlation between the octants mediated by their weights. Therefore, a coarser LAr granularity, namely wheel-wise, has been used to perform the iterative calibration of the LAr hadronic energy scale.

A comparison of the  $P_t$  balances between data and Monte Carlo simulation before and after calibration is presented in Fig. 5.7. The open boxes and the open triangles correspond to the mean values of the average  $P_t$  balance before calibration for data and for simulation, respectively. A dependence of the  $P_t$  balance mean values on the wheels is caused by a mistakenly applied function during Ntuple production. The discrepancy between data and Monte Carlo before performing the  $P_t$  balance calibration, i.e. with the standard HIREC hadronic energy calibration, reached a maximum of about 6% for the IF module. The closed circles and the closed stars in Fig. 5.7 represent the

---

<sup>3</sup>a module here means either an octant or a wheel with or without division on electromagnetic and hadronic parts. It depends on available statistics and convergence of the method.

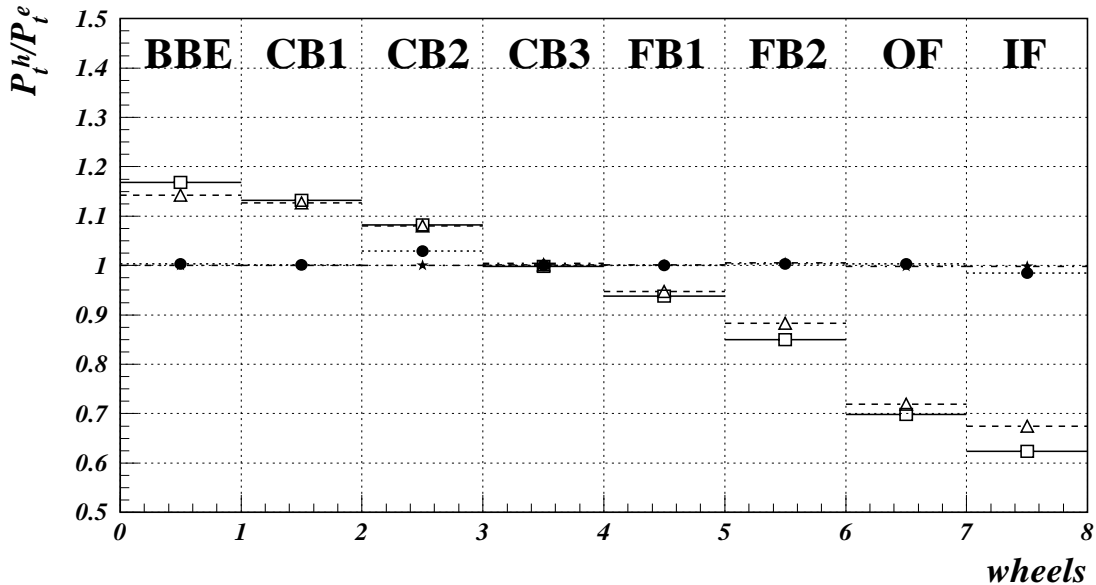


Figure 5.7: Comparison of the mean values of the  $P_t$  balance obtained from Gaussian fits performed to the ratio  $P_t^h/P_t^e$  for 8 wheels of the LAr calorimeter. The open boxes (triangles) represent the situation for data (Monte Carlo) before calibration and the closed boxes (stars) after 8 iterations.

mean values of the ratio  $P_t^h/P_t^e$  after calibration for data and simulation, respectively. These values are very close to unity (by construction) and the discrepancy between data and simulation does not exceed the 2% level. A detailed study of the dependence of  $P_t$  balance on  $\theta_h$  (see Fig. 5.8,a)) and  $P_t^e$  (see Fig. 5.8,c)) supports the quoted 2% accuracy (see Fig. 5.8,b) and Fig. 5.8,d)). Not only mean values of the ratio  $P_t^h/P_t^e$  are correctly described by the simulation but also its shape is well reproduced as can be seen in Fig. 5.8,e).

The iterative calibration procedure has been performed using the same data and Monte Carlo samples as for the Lagrangian method. The applied cuts were also identical with the exception of the  $P_t^e$  cut which was set to  $P_t^e > 3$  GeV in order to cross check the calibration constants with the hadronic energy scale calibration performed by the MPI-ITEP analysis group. The same reason explains the choice of the wheel-wise calibration. Since the original hadronic energy scale was different for two groups, only the ratio between the calibration coefficients for data and for simulation can be compared. This is presented in Table 5.1. The values in the Table exhibit a 1-3% variation in the relative change of the hadronic energy scale for the backward and the central parts of the LAr calorimeter between two groups. The values for the forward part are much more different due to a different treatment of the forward part of the LAr in the Ntuple production chains between the two groups.

In order to check the precision of the hadronic energy scale calibration for the forward part of the LAr calorimeter and to justify the uncertainty of the hadronic energy scale of its backward and central part at the level of 2%, more complex checks

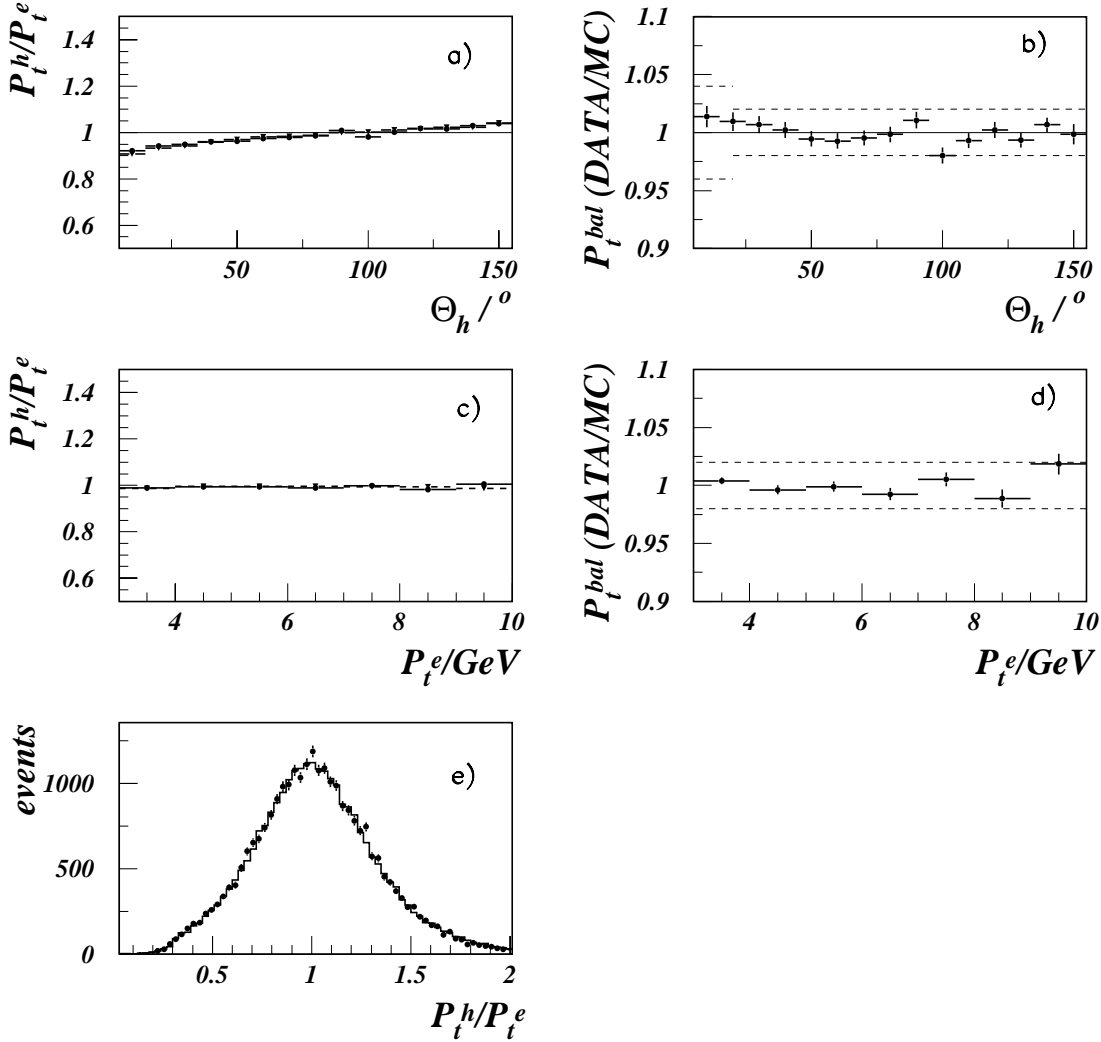


Figure 5.8: Control plots for the LAr calibration with the iterative method. Mean values of the  $P_t$  balance as a function of  $\theta_h$  (a) and  $P_t^e$  (c) for data (closed circles) and Monte Carlo (closed triangles). The corresponding ratios of the mean values between data and Monte Carlo are presented in figures b) and d). Dashed lines in figure b) represent the suggested systematical uncertainty of 2% for backward and central parts of the LAr calorimeter and of 4% for the forward one. The dashed lines in figure d) show that the data to Monte Carlo ratio of  $P_t$  balance mean values are well within 2% variations independently on the transverse momentum of the final state electron. Figure e) represents general shape of the  $P_t$  balance which is very good described by Monte Carlo simulation and both distributions are peaked at unity by construction.

	BBE	CB1	CB2	CB3	FB1	FB2	OF	IF
Data/MC (Zeuthen)	0.91	1.01	0.96	1.03	1.02	1.07	0.99	1.17
Data/MC (MPI-ITEP)	0.93	1.03	0.99	1.	1.	1.06	1.12	1.

Table 5.1: The ratio of the calibration coefficients between data and Monte Carlo simulation obtained from iterative hadronic calibration of the LAr calorimeter in two analyses. Note that the treatment of the OF and IF parts are different (see text).

between the two groups had to be performed. An appropriate check of the hadronic energy scale is a comparison between two analyses of the absolute change of the  $P_t^h$  in the  $(x, Q^2)$  bins in data and in Monte Carlo simulation after performing the calibration. Here, the ratio  $P_{t,cal}^h/P_{t,H1REC}^h$  is considered as the absolute change of the hadronic energy scale after calibration where  $P_{t,cal}^h$  and  $P_{t,H1REC}^h$  correspond to the transverse momenta of the hadronic final state particles after and before calibration, respectively. Since the original hadronic energy scales did not coincide for MPI-ITEP and Zeuthen analyses, only the relative change between data and the simulation had a meaning for the comparison. Remember that only the relative variations between data and the simulation affect the results of the measurement. The uncertainty of the hadronic energy scale has been obtained by comparing the following quantities:

$$DATA/MC_{scale\ change} = \frac{(P_{t,cal}^h/P_{t,H1REC}^h)^{DATA}}{(P_{t,cal}^h/P_{t,H1REC}^h)^{MC}}. \quad (5.9)$$

The relative scale changes expressed by Eq. 5.9 were compared between the two groups with the final event sample which satisfied the DIS event selection criteria described in Section 6.3. The comparison is presented in Fig. 5.9 for the low  $Q^2$  kinematic domain. It depicts the relative hadronic energy scale variations in  $(x, Q^2)$  bins as a result of three different calibrations. The comparison of relative hadronic energy scale changes between the calibrations performed with Lagrangian method without division of “cells+tracks” (open boxes) and with (open crosses) as well as between them and the independently carried out iterative calibration (closed circles) justifies to quote a systematic uncertainty of 2% for the low and middle  $x$  regions. However, this rises up to 4% at high  $x$  because of the forward part uncertainties. These results were taken into account calculating systematic errors of the DIS cross section calculation.

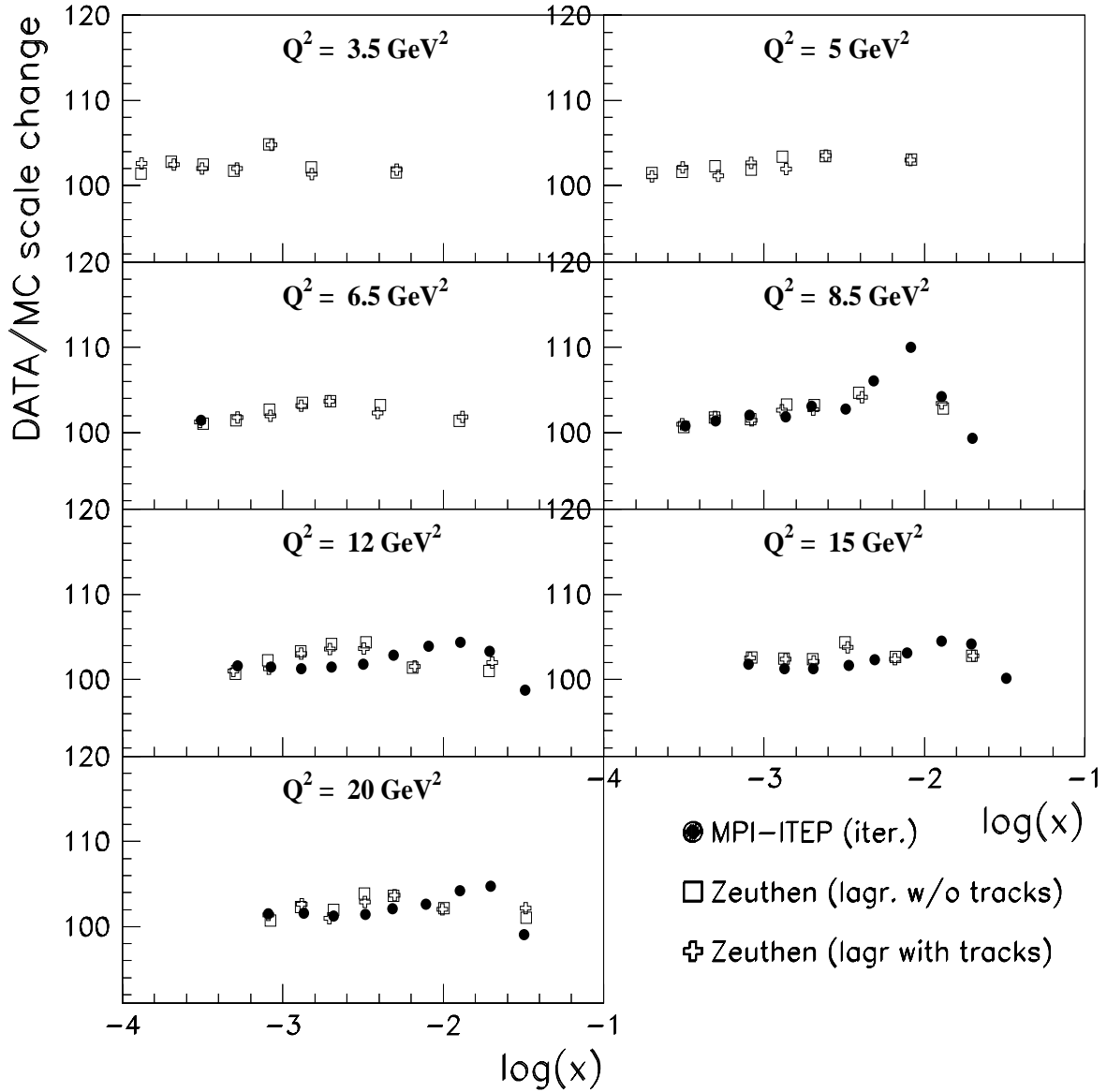


Figure 5.9: Comparison of the relative change of the hadronic energy scale (see Eq. 5.6) between three different calibrations as a function of  $\log(x)$  represented in seven low  $Q^2$  bins. The variations of the points are normally within  $\pm 2\%$  ( $4\%$ ) from the average change of the hadronic energy scale for low and middle (high)  $x$ . Note that at low  $y$ , binning in  $x$  is different for two analyses.

# Chapter 6

## Measurement of the DIS Cross Section

### 6.1 Cross Section Determination

The DIS Born cross section measured in a kinematical bin is determined as follows:

$$\sigma_{\square} = \frac{N_{\square}^{data} - N_{\square}^{bg}}{L} \cdot \frac{C_{\square}}{A \cdot \varepsilon \cdot (1 + \delta_{\square}^{RC})}. \quad (6.1)$$

where:

- $N_{\square}^{data}$  is the number of events accumulated in a bin which passed the DIS selection cuts (see Section 6.3);
- $N_{\square}^{bg}$  is the number of non-DIS (background) events which satisfied the DIS selection criteria. These were estimated using the Monte Carlo simulation. A dedicated study is presented in Section 6.4;
- $L$  is the H1 satellite bunch corrected luminosity corresponding to the selected runs;
- $A$  denotes the detector acceptance calculated using the Monte Carlo simulation. Here, the detector acceptance is defined as the ratio of the total number of reconstructed events to the total number of originally generated events in the bin:  $A = N_{\square}^{MC} / N_{\square}^{gen}$ ;
- $\varepsilon$  are additional detector efficiency corrections obtained from data which were not included or not correctly described in the Monte Carlo simulation;
- $\delta_{\square}^{RC} = \sigma_{\square}^{full} / \sigma_{\square}^{Born} - 1$  are the radiative corrections Here  $\sigma_{\square}^{full}$  and  $\sigma_{\square}^{Born}$  denote the full and Born cross sections integrated in the bin, respectively. These corrections are essential for the extraction of the proton structure functions since the latter are defined with respect to the DIS Born cross section;

- $C_{\square}$  denotes the bin center corrections which have to be applied in order to obtain the cross section at the chosen bin central values  $(x_c, Q_c^2)$  from a bin integrated value of the cross section. The bin center corrections are calculated using Monte Carlo simulation via the following relation:

$$C_{\square} = \frac{d^2\sigma_{Born}(x_c, Q_c^2)/dx dQ^2}{\sigma_{\square}^{Born}}. \quad (6.2)$$

A detailed Monte Carlo simulation is used to perform the acceptance corrections, the bin center corrections and the radiative corrections. Deep-inelastic  $ep$  scattering events are simulated using the DJANGO Monte Carlo generator which includes first order QED radiative corrections <sup>1</sup> (see Section 3.4). In this case Eq. 6.1 for DIS cross section determination can be simplified using the following relation for generated events

$$N_{\square}^{gen} = L^{MC} \sigma_{\square}^{full}, \quad (6.3)$$

and one obtains the cross section definition of the so-called *Monte Carlo method*:

$$\sigma_{\square} = \frac{N_{\square}^{data} - N_{\square}^{bg}}{N_{\square}^{MC}} \cdot \frac{L^{MC}}{L} \cdot \frac{1}{\varepsilon} \cdot \sigma_{\square}^{MC}. \quad (6.4)$$

Here, it should be noticed that the use of the Monte Carlo method is justified only if all relevant aspects of the experiment, like detector acceptance and its submodule efficiencies are correctly reproduced by the Monte Carlo simulation. The detailed study and a thorough comparison of the used quantities between data and the Monte Carlo simulation is therefore necessary. The precision of the DIS cross section measurement presented in this analysis comes from minimizing the discrepancies between data and Monte Carlo simulation by understanding the underlying reasons where possible. Discrepancies which could not be understood were assigned to systematic errors.

The cross section  $\sigma_{\square}^{MC}$  in Eq. 6.4 requires an assumption on  $F_2$  and  $F_L$  structure functions. The behavior of the structure function  $F_2$  was obtained with parton density functions using GRV-94 LO parameterization [57]. The  $F_L$  structure function was initially assumed to be equal to zero. An iteration on these assumptions is required with a DIS cross section model which is closer to the measurement because the structure function dependence enters the result via smearing effects. In this analysis a next-to-leading order QCD fit to the data was used for reweighting the simulated events [102]. The  $F_L$  structure function being essential at high values of the inelasticity  $y$ , has been obtained from the NLO QCD fit. One iteration was found to be sufficient to produce a stable result for the double differential cross section.

---

<sup>1</sup>The higher order QED radiative corrections after all event selection cuts were estimated to be 0.2-0.5% using the program HECTOR [101]. They are not included in the analysis.

## 6.2 Bin Selection

The definition of the binning type ( $x, Q^2$  or  $y, Q^2$ ) and the sizes of the bins in which the double differential cross section is to be measured must be optimized. The binning optimization follows certain criteria listed below which should be satisfied:

- The choice of the kinematical variables  $x$  or  $y$  is based on the corresponding resolutions. Most preferable is the  $(x, Q^2)$  binning since the  $F_2$  evolution is given in terms of these variables. However, the  $y$  resolution at low  $x$  becomes better than that of  $x$ . The contribution of the longitudinal structure function  $F_L$  to the DIS cross section at high  $y$  is  $y^2$  dependent (see Eq. 2.37). The photoproduction rises with  $y$ . These reasons make the  $(y, Q^2)$  binning more preferable at large  $y$ ;
- The size of the bins should be small enough in order to be able to measure the double differential cross section but big enough in order to accumulate reasonable statistics. The statistical errors in the bins should be smaller than the systematic ones;
- The correlation between adjacent bins should be minimized since the Monte Carlo method utilizes the diagonal elements of the acceptance matrix. This criterion is satisfied choosing bin sizes bigger than the kinematical variables resolutions. This restricts the migrations in and out of the bins.

The  $(x, Q^2)$  binning used in the present analysis is depicted in Fig. 6.1 which shows the  $(x, Q^2)$  kinematical plane in a logarithmic scale. The  $(x, Q^2)$  bin boundaries and the bin central values for  $y$  greater than about 0.05 have been taken as in previous analyses of the H1 collaboration. The grid illustrates the boundaries of the analysis bins while the full (open) circles correspond to their central values where the event kinematics has been reconstructed using the electron ( $\Sigma$ ) method. Due to the reasons explained in Section 3.3, the cross section measurement at  $y > 0.15$  has been performed by exploiting the electron method while for lower  $y$  values the  $\Sigma$  method is chosen. The dashed lines of constant polar angles represent the kinematical acceptance limits of this analysis set by the angular acceptance of the backward silicon tracker. It is worth to notice that the BST acceptance lines are roughly parallel to the constant  $Q^2$  lines at  $y < 0.15$  while at higher values of  $y$  the lines turn and at  $y > 0.6$  these are about to follow the lines of constant  $y$ . This is an additional reason to use the  $(y, Q^2)$  binning for  $y > 0.6$ . Two bins 0.6 - 0.75 and 0.75 - 0.9 with the central values of 0.68 and 0.82, respectively, were chosen for the high  $y$  binning.

The very low  $y$  ( $y < 0.01$ ) kinematic region at low  $Q^2$  was so far not accessed by H1 due to a dramatic decrease of the vertex reconstruction efficiency as can be seen in Fig. 6.2, left. The rapid decrease of the vertex reconstruction efficiency towards very low  $y$  values is caused by the fact that the polar angle of the current jet, which can be approximately expressed as  $\theta_h \approx 4 \cdot y_e / \sin(\theta_e)$ , moves out of the central tracker detector acceptance. The angular acceptance of the CT detectors is illustrated in

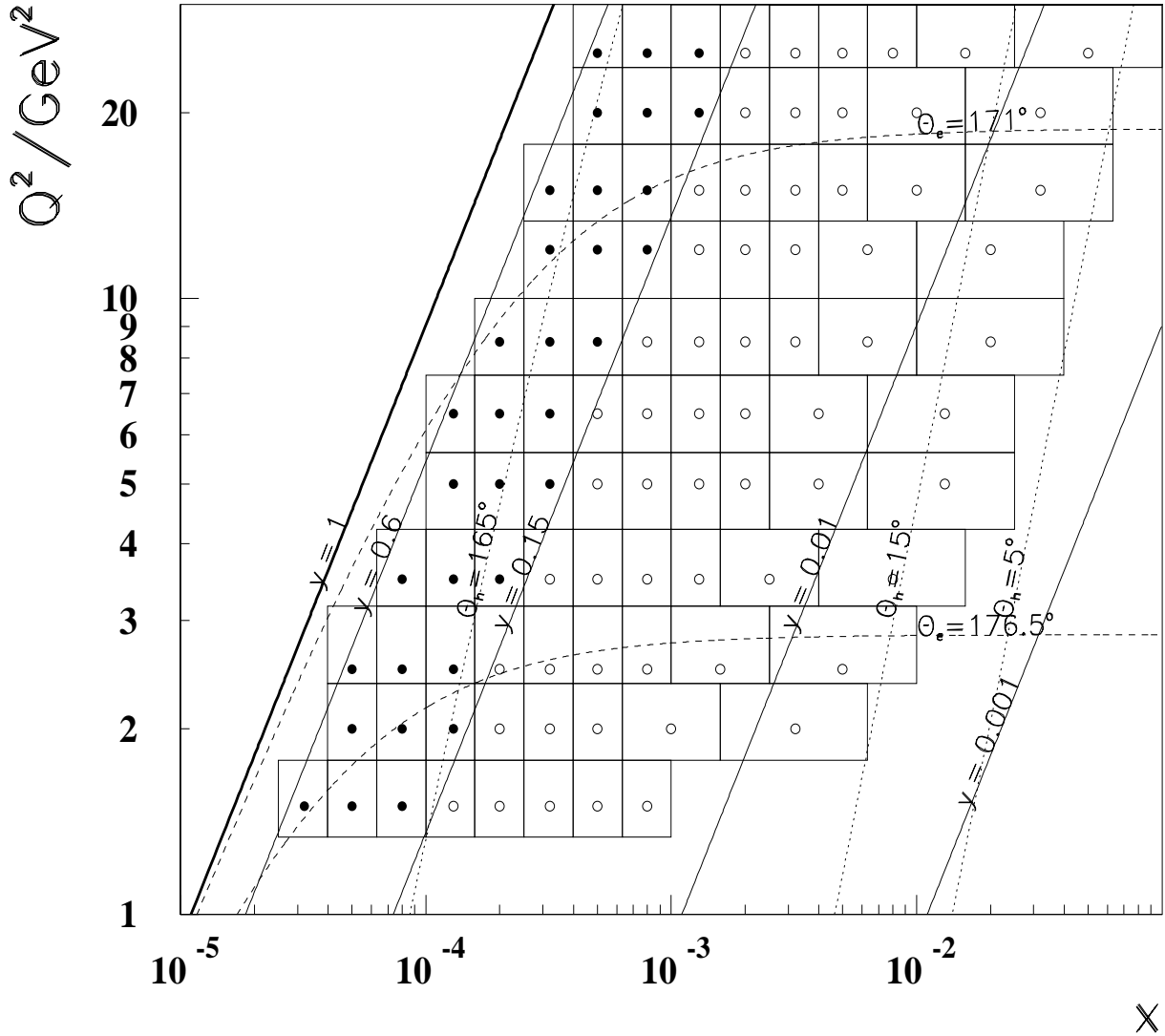


Figure 6.1: Kinematic plane of  $x$  and  $Q^2$ . The grid represents the  $(x, Q^2)$  binning used in the analysis for  $y < 0.6$ . The size of the bins is adapted to the resolution of the kinematic variables (see text). Closed (open) points indicate the bins where the electron ( $\Sigma$  method) is used to measure the cross section, respectively. The dashed curves of constant polar angle  $\theta_e$  of the scattered electron denote the angular acceptance limits of the BST, whereas the dotted curves represent the approximate angular acceptance of the CJC at constant jet angles  $\theta_h = 165^\circ$  and  $\theta_h = 15^\circ$ . The dotted curve at  $\theta_h = 5^\circ$  depicts the lowermost acceptance of the LAr calorimeter. Also shown are lines of constant inelasticity  $y$ .

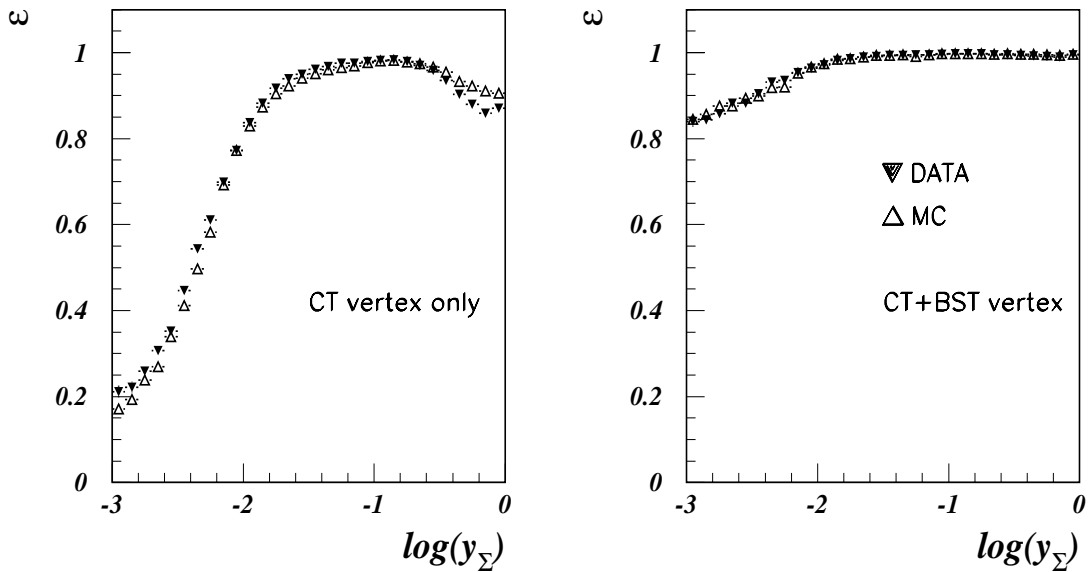


Figure 6.2: Vertex reconstruction efficiency as a function of  $y_{\Sigma}$  within the BST acceptance. The left picture represents the situation where only the central tracker vertices are used. The right picture is based on the reconstruction of the event vertex supplemented by the measurement of the scattered electron with the BST.

Fig. 6.1 by the dotted lines corresponding to jet angles at  $165^{\circ}$  and  $15^{\circ}$ , respectively. The uppermost angular acceptance of the CT detectors corresponds to the inelasticity values greater than about 0.3 where a decrease of the vertex reconstruction efficiency is also visible (see Fig. 6.2,left), but not so drastic as for low  $y$ . The reason for such a different behavior of the vertex reconstruction efficiency on the opposite edges of the central tracker detectors acceptance is the different final state topology. At low  $y$ , the hadronic final state particles are strongly boosted into forward direction and, thus, are well collimated. At high  $y$ , the final state is broader due to the much smaller electron boost and the particle multiplicity is small. As a consequence, there is a good probability for the hadronic final state particles to be scattered in the CT detectors acceptance. Curing the vertex reconstruction efficiency drop at low  $y$  and at high  $y$  had been one of the major reasons to build the BST [72].

The vertex reconstruction becomes straightforward when the vertex is defined with the scattered electron itself. The backward silicon tracker realizes this possibility at  $Q^2$  below  $20 \text{ GeV}^2$ . A study of the event vertex reconstruction is performed here using the normal case in the H1 analysis when the vertex definition at low  $Q^2$  is supplemented by the BST measurement. The resulting vertex reconstruction efficiency in this case is presented in Fig. 6.2,right. A small residual decrease of the efficiency for  $\log(y_{\Sigma}) < -1.7$ , corresponding to  $y_{\Sigma} < 0.03$ , is caused by the multiplication of the BST efficiency with its acceptance and summation with the CT vertex reconstruction efficiency itself. It is also noticeable on this figure that a very good agreement for the vertex reconstruction efficiency between data and Monte Carlo simulation has been obtained after the supplementation of the CT vertex measurement by the BST.

This significant improvement of the event vertex reconstruction permits to extend the range of the DIS cross section measurement towards the very low  $y$  values, approaching the LAr calorimeter limit at  $\theta_h = 5^\circ$ , corresponding to  $y \sim 0.002$  at low  $Q^2$  (see Fig. 6.1). The gain of statistics with the low angle jets allows to understand better the systematic effects in the forward part of the LAr calorimeter as well as to improve the global calibration of the hadronic energy scale, as described in Chapter 5.

Still, the bin sizes in the low  $y$  kinematic region should be adjusted according to the degrading resolution of the inelasticity which is due to the more pronounced fluctuations of the hadronic energy. The adjustment of the bin sizes has been done by utilizing so-called “purity” and “stability” criteria which quantify the magnitude of the migrations of events between different bins. This procedure has been performed using a Monte Carlo simulation of non-radiative DIS events.

The **Purity** of a bin is defined for events passing the final DIS selection criteria (see Section 6.3) as the ratio of the number of events generated and reconstructed in a bin to the number of events reconstructed in this bin:

$$Purity = \frac{N^{gen.\&rec.}}{N^{rec.}}. \quad (6.5)$$

The **Stability** of a bin is defined also for events passing the final DIS selection as the ratio of the number of events generated and reconstructed in a bin to the number of events which were actually generated in this bin:

$$Stability = \frac{N^{gen.\&rec.}}{N^{gen.}}. \quad (6.6)$$

The purity indicates how many of the events measured in a bin are contaminated by event migration from adjacent bins, whereas the stability controls the migration out of the bin, the event actually belongs to. Both quantities take values between 0 and 1 by definition and they are sensitive to resolution and systematic shifts in the reconstruction of  $x$  and  $Q^2$ . A remarkable outcome of the improved event vertex reconstruction with the BST is the improved reconstruction of  $Q^2$  which is independent of the inelasticity. Thus, one can use a fine  $Q^2$  binning down to very low values of  $Q^2$ .

The purity and stability of the event kinematics reconstruction corresponding to the electron method are depicted in Fig. 6.3, top for the  $(x, Q^2)$  binning used in the analysis. The values of both quantities are about 70% for  $y > 0.1$  as a consequence of the high resolution of the kinematic variables based on the precisely measured final state electron energy and polar angle. However, the  $y_e$  resolution rapidly degrades towards low  $y$  due to the factor  $1/y$  (see Section 3.3). That causes a drop of purity and stability to unacceptably low values below  $y \approx 0.05$ . The applicability of the electron method is consequently limited to about this value although one may reach even lower  $y$  with very wide bins.

The second method ( $\Sigma$ ) used in the analysis is less preferable for  $y > 0.1$  than the electron method due to its worse resolution originating from the usage of the hadronic

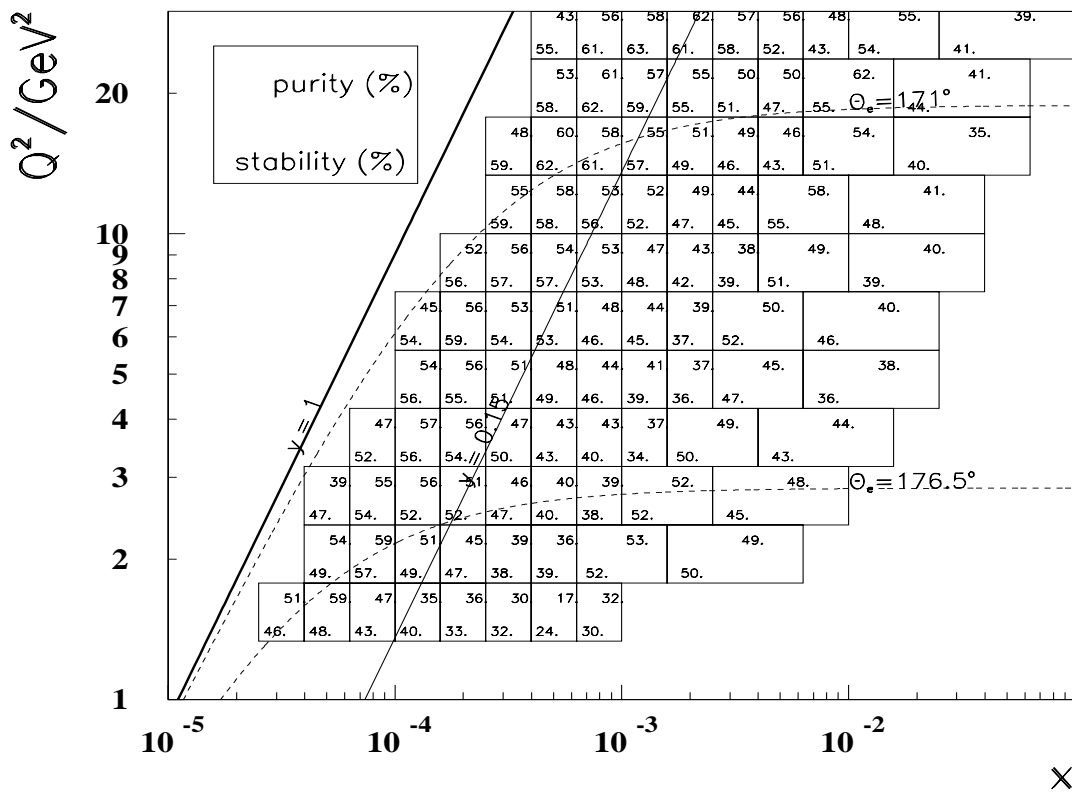
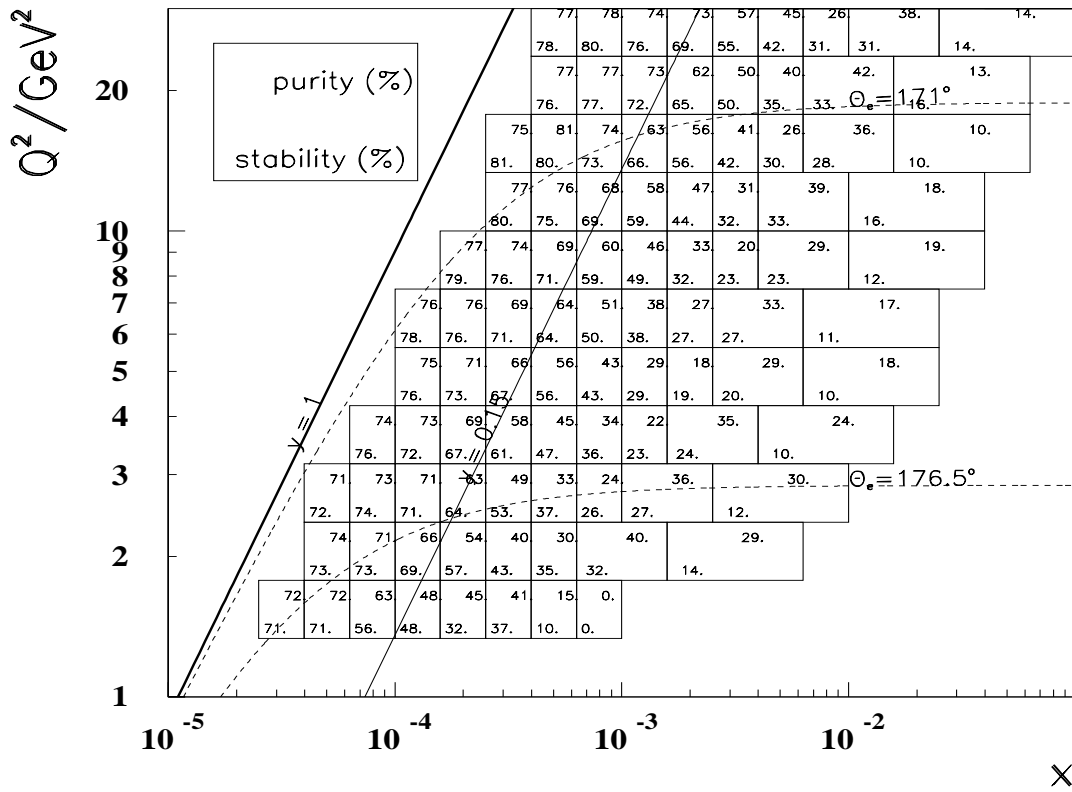


Figure 6.3: The values of *purity* and *stability* for different bins of the  $(x, Q^2)$  kinematic plane. The picture on the top (bottom) stands for electron ( $\Sigma$  method), respectively. The solid lines show the constant inelasticity. For  $y > 0.15$  ( $y < 0.15$ ) the electron ( $\Sigma$ ) method has been used. Also shown are the lines of constant polar angle of the scattered electron illustrating the BST acceptance.

measurement. This fact makes the  $\Sigma$  method also sensitive to the acceptance edges of the analysis. On the other hand, the resolution in  $y_{\Sigma}$  is less dependent on  $y$  than for its counterpart  $y_e$ . Therefore, the values of the purity and stability for  $\Sigma$  method presented in Fig. 6.3, bottom show a much less significant variation within the inelasticity range. Still, at  $y \approx 0.02$  both quantities approach the critical value of 30% for the  $\Sigma$ -method. A way to keep the purity and the stability of the bins significantly above 30% is to re-adjust their sizes according to the degrading  $x$  resolution as shown in the figures. Having re-adjusted the bin sizes, the kinematic region of the analysis has been extended down to  $y \approx 0.003$  which was not accessible so far by H1.

## 6.3 Event Selection

An attempt has been made to keep the number of event selection cuts as low as possible. According to the definitions of the method described in Section 6.1, it is essential that each of the imposed selection cuts would cause the same action in data and in Monte Carlo simulation in terms of selected and rejected events. An overview of the cuts is given in Table 6.1.

A cluster with maximum deposited energy has been considered to be the electron candidate since for  $y < 0.5$  the electron energy is greater than that of the hadronic jet. Even for higher inelasticity values the maximum cluster energy remains a reliable criterion since the hadronic jet scattered backward is usually badly collimated depositing various distinguishable clusters from the hadronic final state particles. A second electron identification criterion used in this work was a so-called *maximum  $P_t$  ordering*. This criterion exploits the  $P_t$  balance in the event (see Eq. 3.3) which states that the transverse momentum of the electron is balanced by the sum of  $P_t$  of the hadronic final state particles. Therefore, in most of the cases the particle with the largest transverse momentum is the electron. Due to energy fluctuations deposited by the hadronic final state which are more pronounced at low  $Q^2$ , the *maximum  $P_t$  ordering* was used only in order to estimate systematic effects<sup>2</sup>. The DIS cross section measured with the maximum transverse momentum criterion was found to agree within 1% systematic uncertainty with that measured with the maximum energy criterion.

### 6.3.1 Cluster Radius Cut

The difference in the transverse size between clusters of electromagnetic and of hadronic origin has been utilized in order to suppress hadronic background. This background rejection is based on the fact that the clusters produced by hadrons are broader than those produced by electrons in electromagnetic calorimeters.

Energy deposited in clusters is usually spread over many cells of the calorimeter which has a cell size of  $4 \times 4$  cm and a Moliere radius of about 0.26 cm. It allows to

---

<sup>2</sup>A comprehensive study of the electron identification in the backward part of the H1 detector can be found in [37].

cut #	name	definition	action
1	Cluster radius	$R_{cl} < 4$ cm	electron ID
2	Hadr. fraction	$E_{had}/E_{em} < 0.15$	same as cut 1
3	$E - P_z$ cut	$E - P_z > 35$ GeV	suppression of ISR and $\gamma p$ background
4	Vertex	$\exists$ vertex for $y > 0.5$	suppression of QED Compton
5	Z-vertex position	$\text{abs}(Z_v) < 20$ cm	beam background rejection
6	acceptance	BST acceptance	safe region on BST
7	BST validation	$ \Delta R_{BST-SPC}  < 2.$ cm	$\gamma p$ suppression
8	$P_t$ balance	$P_t^h/P_t^e > 0.3$ for $E'_e > 24$ GeV	suppression of losses at low $y$

Table 6.1: The DIS event selection criteria used in the present analysis.

use different approaches for estimation of the cluster radius. In this analysis, the cluster radius definition exploits a method, originally proposed in [103], which introduces weights of the cluster cells depending logarithmically on their energies and also defining a suitable *cutoff weight* ( $w_{cut}$ ):

$$w_i^{log} = \frac{W_i^{log}}{\sum_{j=1}^N W_j^{log}}, \quad W_i^{log} = \max\left(0, w_{cut} + \ln \frac{E_i}{E_{cluster}}\right). \quad (6.7)$$

The cluster radius is then calculated as a quadratical sum of logarithmically weighted distances  $R_i$  between the center of the cluster as defined in Section 4.8.3 and the geometrical center of cell  $i$ :

$$R_{cl} = \sqrt{\sum_i (R_i w_i^{log})^2}. \quad (6.8)$$

For data  $w_{cut}^{data} = 4.85$ . The best adjustment of the simulated radius distribution to the data was obtained with  $w_{cut}^{MC} = 5.05$ .

The cluster radius estimator with logarithmic weighting has been proven to have much better resolving power between the clusters with deposited energy of electromagnetic and hadronic origin [37]. This selection criterion plays an essential role for the identification of the electron candidate cluster with low energy (high  $y$ ) by separating them from the usually broader clusters originating from the hadronic final state particles. The radius cluster shape in the Monte Carlo simulation is slightly shifted to larger  $R_{cl}$  than the data as can be seen in Fig. 6.4, left. The radius cluster cut had to be imposed in such a way as to provide a good description of the rejected events. A cut on  $R_{cl} > 4$  cm was chosen. As the Monte Carlo simulation illustrates, the bulk of the rejected events belongs to photoproduction background. Some part of the rejected ‘‘DIS events’’ is due to the electromagnetic clusters from  $\pi^0$  decays when two gammas produce a broad electromagnetic cluster.

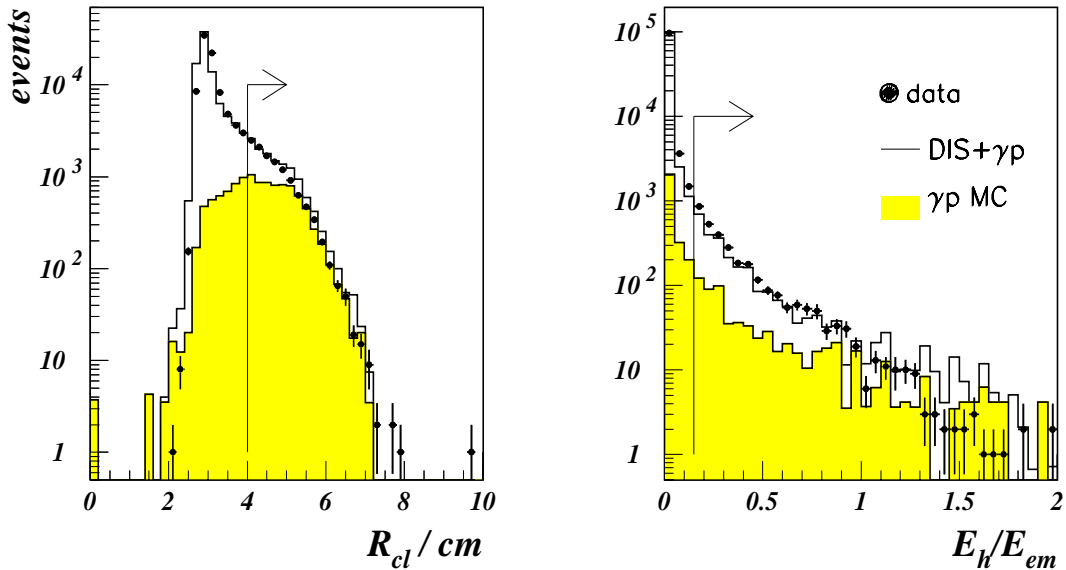


Figure 6.4: Left: cluster radius distribution with logarithmic weighting (see text) presented with energy selection  $E'_e < 20$  GeV. Also shown is the  $R_{cl} < 4$  cm cut. Bulk of the rejected events are clearly related to the  $\gamma p$  background. Right: distribution of the  $E_{had}/E_{em}$  ratio corresponding to the longitudinal size of the electron candidate cluster. The applied cut on  $E_{had}/E_{em} < 0.15$  is also shown and, as one can see, it rejects mostly hadronic clusters. Closed points correspond to the data, the shaded histograms present the  $\gamma p$  background and the open histograms are a sum of a DIS Monte Carlo simulation and the  $\gamma p$  background for both pictures.

### 6.3.2 Hadronic Energy Fraction Cut

The hadronic energy fraction cut, illustrated in Fig. 6.4, right exploits the difference of the shower development in longitudinal direction with electromagnetic and hadronic origins. The electromagnetic clusters are mostly entirely contained inside the  $27X_0$  thick SpaCal electromagnetic section whereas for final state hadrons it is seen only as a  $1\lambda$  thick device and thus can be considered as a “hadronic pre-shower” detector. The hadronic section of SpaCal calorimeter is mounted behind the electromagnetic one (see Section 3.2.4) and supplements the energy measurement. It was used to sum up the energy deposited behind the most energetic cluster in a cylinder of 15 cm radius. If the fraction of energy reconstructed in this cylinder was greater than 15% of the energy deposited in the hottest cluster of the electromagnetic section, the latter is identified to be hadronic.

### 6.3.3 $E - P_z$ Cut

The quantity  $E - P_z = \sum_h E_h(1 - \cos \theta_h) + E_e'(1 - \cos \theta_e)$  denotes the difference between the deposited energy and the  $z$ -component of the momentum summed over all particles, neglecting their masses and excluding the energy deposited in the electron and photon taggers (see Section 3.2.1).  $E - P_z$  is a measure for the momentum conservation and must be equal to  $2E_e = 55.2$  GeV. Departures from this value beyond resolution effects may have the following reasons:

- energy loss caused by undetected ( $\nu$ ) or minimum ionizing particles ( $\mu$  and some part of  $\pi^\pm$  in the  $2\lambda$ -thick SpaCal);
- initial state radiation when the photon, radiated off the incoming electron, escapes the detection along the beam pipe and thus decreases the  $E - P_z$  by value equal to twice of its own energy;
- photoproduction background, when the final state electron scatters with a polar angle out of the backward calorimeters acceptance.

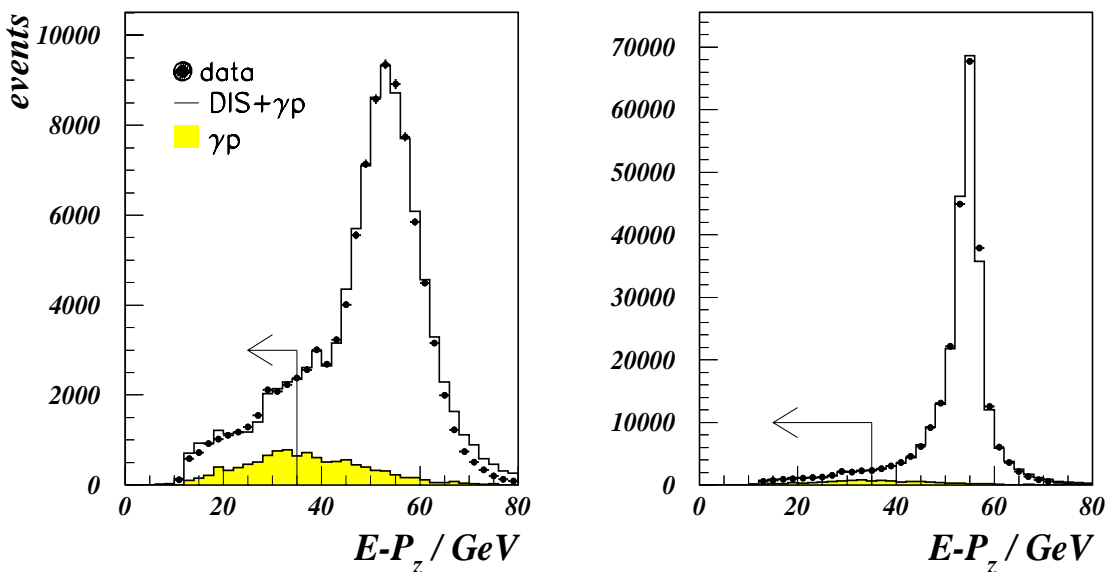


Figure 6.5: Distribution of the quantity  $E - P_z$  for energies  $5.5 < E_e' < 20$  GeV (left picture) and for  $E_e' > 5.5$  GeV (right picture). Closed points present data. The shaded histograms illustrate the simulated  $\gamma p$  background. The open histogram is a sum of the DIS Monte Carlo simulation and this background. Both distributions correspond to events with all DIS selection criteria being satisfied, excluding the  $E - P_z$  cut itself. The applied cut on  $E - P_z > 35$  GeV is shown on both pictures. The rejected events are well described by the simulation. A drop at  $E - P_z = 27.6$  GeV corresponds to the central vertex requirement for  $y > 0.5$  in order to suppress the QED Compton events (see text).

Thus, the quantity  $E - P_z$  can be used against the  $\gamma p$  background and the radiative corrections to DIS process. The  $E - P_z$  distribution for energies  $5.5 < E'_e < 20$  GeV and the imposed cut on 35 GeV are presented in Fig. 6.5, left. All selection cuts are applied except the  $E - P_z$  itself. A tail of the distribution to be cut (corresponds basically to ISR and photoproduction events) is well described by simulation. A drop at  $E - P_z$  value of 27.6 GeV relates to a central vertex requirement for  $y > 0.5$  in order to suppress the QED Compton events. The  $E - P_z$  distribution has a pronounced peak at  $E - P_z$  value a bit lower than the nominal one. This is related to not complete hadronic shower containment in the SpaCal. However, as can be seen, this fact is well reproduced by Monte Carlo simulation. For comparison, the  $E - P_z$  distribution for all energies of the scattered electrons is depicted in Fig. 6.5, right showing the peak at nominal value of about 55 GeV.

### 6.3.4 $P_t$ Balance Cut

As the result of the global LAr calibration (see Section 5.2), based on transverse momentum conservation, the ratio  $P_t^h/P_t^e$  is distributed with a mean position at unity as can be seen in Fig. 5.5, e). Its dispersion is defined by fluctuations of the energy deposited by hadronic final state particles.

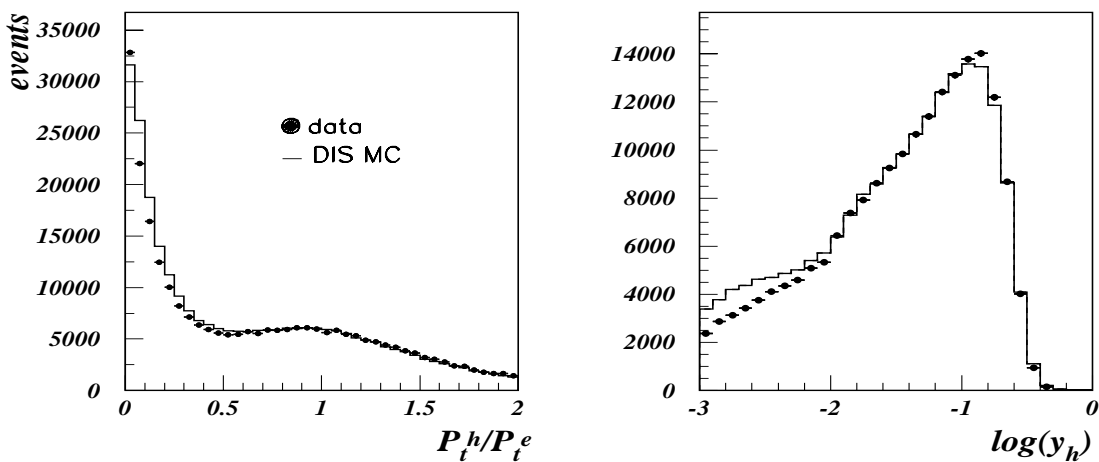


Figure 6.6: Left:  $P_t$  balance distribution for energies  $E'_e > 20$  GeV. Right: The  $y_h$  distribution for  $E'_e > 20$ . Closed points represent data. The histogram represents the simulated event sample with *double counting* of events with  $5 < W_{gen} < 10$  GeV (see text).

Due to the forward and backward beam pipe holes, the acceptance of the H1 detector is limited. The acceptance limitation leads to energy loss because of final state particles escaping detection. In the low  $Q^2$  kinematic region, where the present analysis has been performed, the losses become especially pronounced at high  $x$  as  $F_2(x, Q^2)$  vanishes in the limit of  $x \rightarrow 1$  and the photon-proton system mass squared

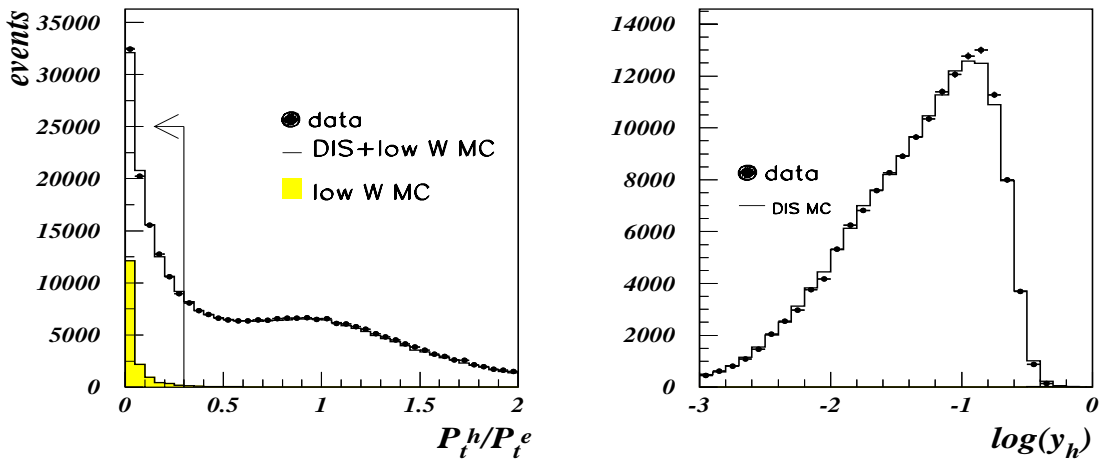


Figure 6.7: Left:  $P_t$  balance distribution for energies  $E'_e > 20$  GeV. Closed points represent data. The shaded histogram illustrates DIS events with  $W_{gen} < 5$  GeV simulated with the HERWIG generator. The open histogram represents the sum of two simulated event samples with  $W_{gen} < 5$  GeV (HERWIG) and  $W_{gen} > 5$  GeV (DJANGO). The peak at zero corresponds to DIS events with a large fraction of hadronic final state particles scattered below the forward modules of the LAr calorimeter. Events with  $P_t^h/P_t^e < 0.3$  for  $E'_e > 24$  GeV were rejected (see text). Right: The  $y_h$  distribution for energies  $E'_e > 20$  GeV with applied  $P_t$  balance cut. Closed points represent data. The histogram illustrates the DIS Monte Carlo simulation. Less than 1% of the low  $W$  events pass the  $P_t$  balance cut, therefore, they were not added to the final Monte Carlo simulation.

$W^2 = Q^2 \cdot (1 - x)/x + M_p^2$  runs into the resonance region. The hadronic final state scatters below the forward calorimeter acceptance. This leads to substantial imbalance between the measured transverse momentum of the hadronic system and that of the scattered electron which is depicted in Fig. 6.6, left by a large peak at zero of the  $P_t$  balance distribution in data. That peak is not described in Monte Carlo simulation. The reason is that the DJANGO simulation program does not generate events below  $W_{gen} < 5$  GeV (see Section 3.4) and, thus, the resonance events remain undescribed. In an earlier analysis [91] the DIS events generated in the kinematical region  $5 < W_{gen} < 10$  GeV were double counted, i.e their weight was increased by a factor of 2. This approach gave an average description of the low  $W$  region although the  $P_t$ -imbalance remained undescribed. The double counting of the DIS events for  $5 < W_{gen} < 10$  GeV leads also to a significant disagreement between data and the simulation for  $y_h < 0.01$  as can be seen in Fig. 6.6, right. Thus, double counting of events must be considered as a poor solution for a formal description of the resonance events.

An attempt has been made to overcome this problem and, thus, to extend the analysis towards the kinematical region below  $y = 0.01$  in order to cover the gap to the kinematic region of the fixed target experiments. The simulation program HERWIG

was used to generate the DIS events with the  $W_{gen} < 5$  GeV (see Section 3.4). These were added to the DIS events generated in the DJANGO program with  $W_{gen} > 5$  GeV and normalized to luminosity for data. A good description of the hadronic energy loss have been achieved afterwards as illustrated in Fig. 6.7,left. In order to minimize the influence of hadronic energy loss on the kinematics reconstruction, a cut on  $P_t^h/P_t^e > 0.3$  for  $E_e' > 24$  GeV was applied. Fig. 6.7,right illustrates the good description of the region below  $y = 0.01$  with the applied  $P_t$  balance cut.

### 6.3.5 BST Related Cuts

The Backward Silicon Tracker has been used in this analysis for the first time to measure the inclusive  $ep$  DIS cross section. A special electron identification program, called “BST electron finder” as described in Appendix A, has been developed for validation of an electron candidate cluster in the SpaCal calorimeter and reconstruction of the electron candidate track. The validation means that the BST becomes automatically a “master” of the cross section measurement. In this section, both BST efficiency and its acceptance will be investigated separately although only their superposition counts in the final result.

The acceptance of the tracker is defined in the “BST electron finder” by the requirement of at least two possible hits in the active BST volume for track reconstruction (see Section A.4). In other words, a track is supposed to be in the acceptance if it crosses the tracker below the outer sensor radius from the second plane and above the inner radius of the third plane (see Eq. A.2).

In the physics analysis, the BST acceptance had to be recalculated taking into account the beam tilt. The tilt corrected acceptance has been defined in the beam coordinate system by a concentric cut around the beam center position in the middle of the active volume of the BST which is calculated in the H1 coordinate system as follows:

$$\begin{aligned} x_{beam}^{BST} &= x_{beam} + \tan(\theta_x^{tilt}) \cdot z_{center}^{BST} = 0.45 \text{ cm}, \\ y_{beam}^{BST} &= y_{beam} + \tan(\theta_y^{tilt}) \cdot z_{center}^{BST} = 0.29 \text{ cm}. \end{aligned} \tag{6.9}$$

The average beam center position is the same for data and Monte Carlo simulation. The following set of relations transforms the acceptance definition from the H1 coordinate system to the one of the beam:

$$\begin{aligned} R_3^{BST} &= \tan(\theta_e) (z_3 - z_v), \\ R_2^{BST} &= \tan(\theta_e) (z_2 - z_v). \end{aligned} \tag{6.10}$$

Here,  $\theta_e$  is the beam tilt corrected polar angle of the scattered electron and  $z_2$  and  $z_3$  are the  $z$ -positions of the second and third planes of the tracker, respectively. The

correct radial positions of a track which crosses the second and third planes of the tracker in the beam system are obtained from the following relations:

$$\begin{aligned} R_{3,BST}^{beam} &= (R_3^{BST} \cos \phi_e + x_{beam}^{BST}) \oplus (R_3^{BST} \sin \phi_e + y_{beam}^{BST}) > R_{min}, \\ R_{2,BST}^{beam} &= (R_2^{BST} \cos \phi_e + x_{beam}^{BST}) \oplus (R_2^{BST} \sin \phi_e + y_{beam}^{BST}) < R_{max}, \end{aligned} \quad (6.11)$$

where  $R_{min}$  and  $R_{max}$  define the inner and outer radial acceptance cuts, respectively. Here, symbol  $\oplus$  stands for quadratic summation. The full acceptance corresponds to  $R_{min} = 5.9$  cm and  $R_{max} = 12.04$  cm.

In Fig. 6.8,a) the full BST acceptance is shown as a function of the polar angle in the data (closed triangles) and in the Monte Carlo simulation (open triangles). All DIS selection cuts are applied except the acceptance cut itself. An agreement well within 1% is seen in Fig. 6.8,b) which shows the ratio of the acceptance between simulated and measured data.

Within the acceptance still the reconstruction efficiency varies as a function of the polar angle because a varying number of planes (2 to 4) is crossed. The efficiency of the tracker has been studied for high energy electrons ( $E'_e > 20$  GeV) in order to exclude a possible bias due to high energetic  $\pi^0$  originating from the photoproduction background (see Section 6.4). In Fig. 6.8,c) and e) the BST efficiency in the BST acceptance region is presented as a function of the polar and azimuthal angles of the scattered electron, respectively. Also shown is the comparison with the Monte Carlo simulation. The simulated efficiency was based on the studies of the internal efficiencies of the 64 sensors presented in Section 4.5 and of the coherent readout losses as described in Section 4.6. An additional fine tuning of efficiencies was performed due to some dead preamplifier chips (APC's). This resulted in a few per cent corrections for particular sectors. As a result, the BST efficiency is described from  $\theta_e = 176.5^\circ$  down to  $\theta_e \approx 171^\circ$  within 1% systematic uncertainty as shown in Fig. 6.8,d) and f).

The influence of the tracker acceptance on the measured structure function  $F_2(x, Q^2)$  has been systematically studied by sequential restriction of the inner and outer acceptance cuts within a one millimeter step. A five per cent effect has been found for  $F_2$  points in the high  $y$  region at  $Q^2 < 6.5$  GeV<sup>2</sup>. The radial BST acceptance limits were narrowed to a region where  $F_2$  points were stabilized using  $R_{max} < 11.5$  cm and  $R_{min} > 6.5$  cm. In Fig. 6.9,a) this narrowed BST acceptance is shown as a function of the polar angle for measured and simulated data. The corresponding ratio of the acceptance between Monte Carlo simulation and the data is presented in Fig. 6.9,b) showing an understanding of the acceptance within 1% systematic accuracy apart from the edges where also the fluctuations become more pronounced. This holds also for the efficiency shown in Fig. 6.9,c) for the narrowed acceptance range. The ratio of the efficiency between simulated and measured data presented in Fig. 6.9,d) shows that the BST efficiency is described with about 1% systematic uncertainty. Note that it anti-correlates with the ratio of the acceptance (see Fig. 6.9,c)). An overestimation of the acceptance leads to an underestimation of the efficiency and vice versa. This is a nice feature for the BST track validation which is a superposition of acceptance and

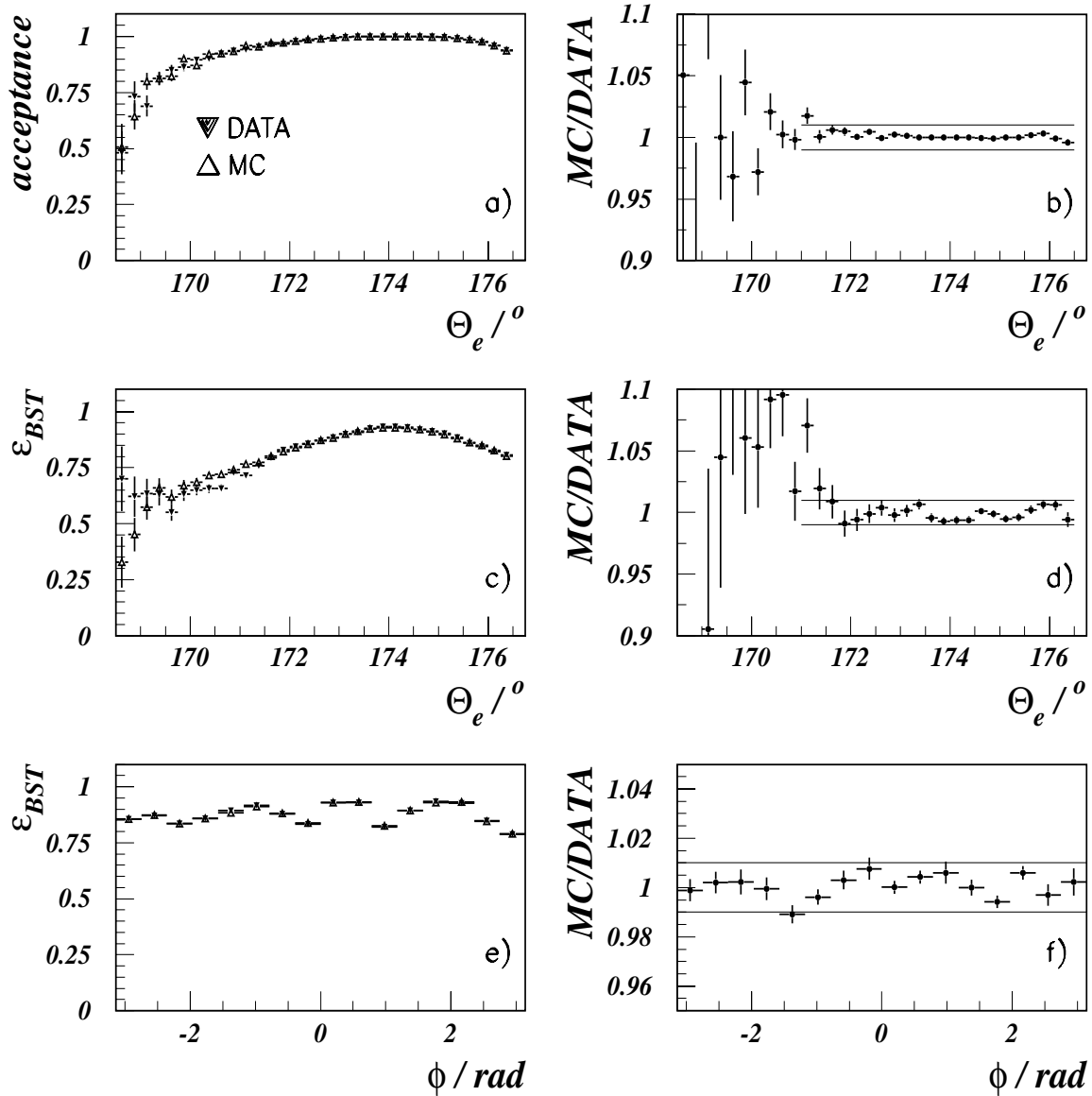


Figure 6.8: a) BST acceptance as a function of the polar angle and b) the corresponding ratio between simulation and data. c) BST efficiency within the acceptance as a function of the polar angle. The corresponding ratio between simulation and data is shown in d). e) BST efficiency within the acceptance as a function of the azimuthal angle. The corresponding ratio between simulation and data is shown in f). The 16  $\phi$  bins correspond to the 16 fold azimuthal subdivision of the detector.

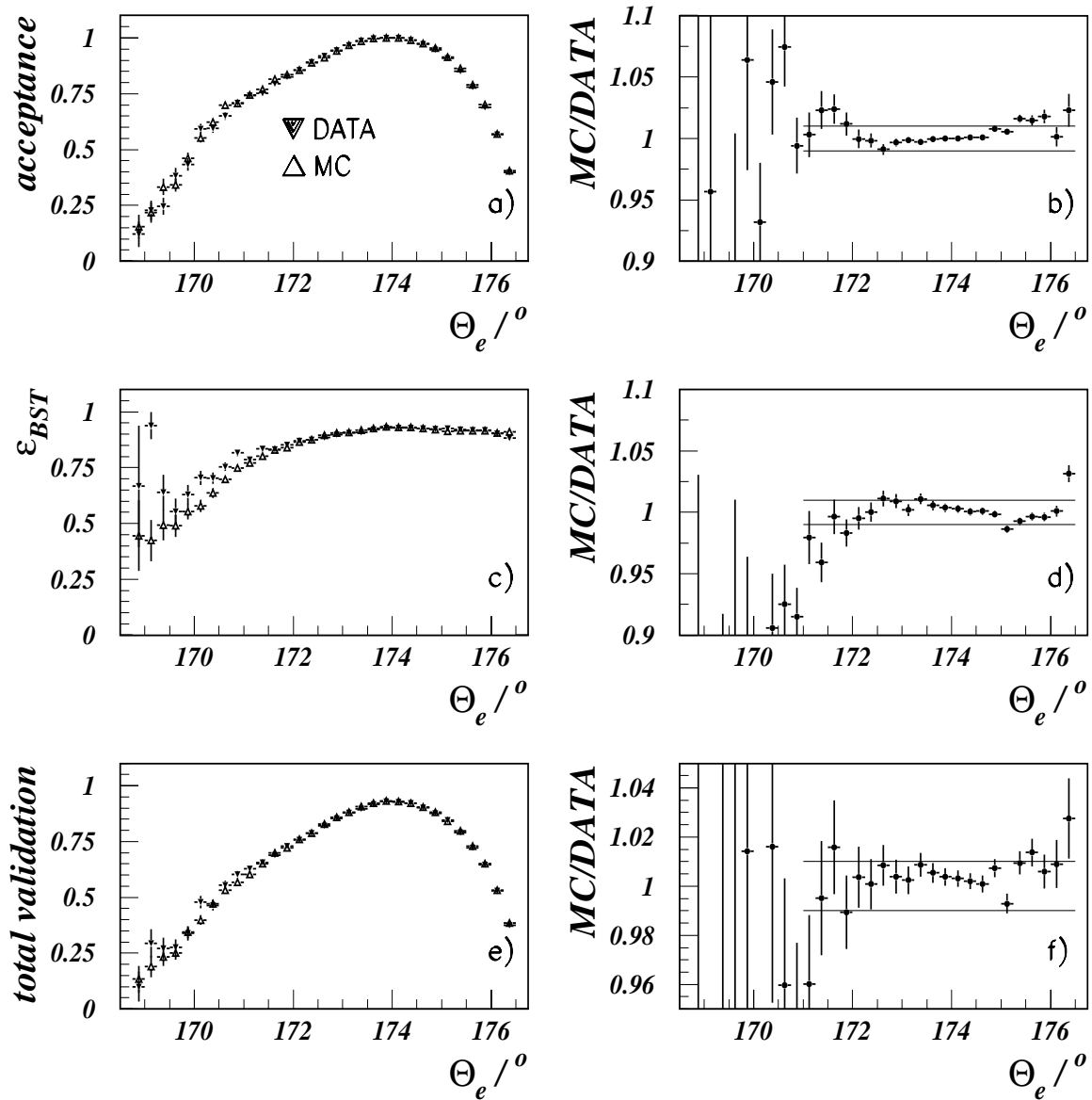


Figure 6.9: a) BST acceptance with  $R_{max} = 11.5$  cm and  $R_{min} = 6.5$  cm (see text) as a function of the polar angle and b) the corresponding ratio between simulation and data. c) BST efficiency within the acceptance as a function of the polar angle. The corresponding ratio between simulation and data is shown in d). e) Superposition of the BST acceptance and efficiency which represents the total validation as a function of polar angle. The corresponding ratio between simulation and data is shown in f). All quantities are described within 1% of systematic uncertainty apart from the edges of the BST acceptance.

efficiency. In Fig. 6.9,e) the BST validation of the electron candidate clusters is shown as a function of the polar angle of the scattered electron. The overall effect on the cross section measurement due to BST validation is described within 1% systematic uncertainty as is represented in Fig. 6.9,f) showing the corresponding ratio between Monte Carlo simulation and data. Yet, an additional study of the BST acceptance, defined with two systematically different methods, showed up to 3% difference for the polar angle of the scattered electron below  $172^\circ$  (see Section A.6) affecting essentially the high  $y$  kinematic domain at low  $Q^2$ .

### 6.3.6 Vertex Position Cut

The  $z$ -position of the interaction vertex is measured using the final state electron scattered in the BST acceptance range. The central trackers are used to measure the run dependent  $x$  and  $y$  positions of the event vertex. These are needed in order to correctly reconstruct the  $z$ -position of the vertex in the “BST electron finder” described in Appendix A.

Events with  $z$ -position of the event vertex within 20 cm range around its nominal position were used for further analysis (cut #5 in Table 6.1).

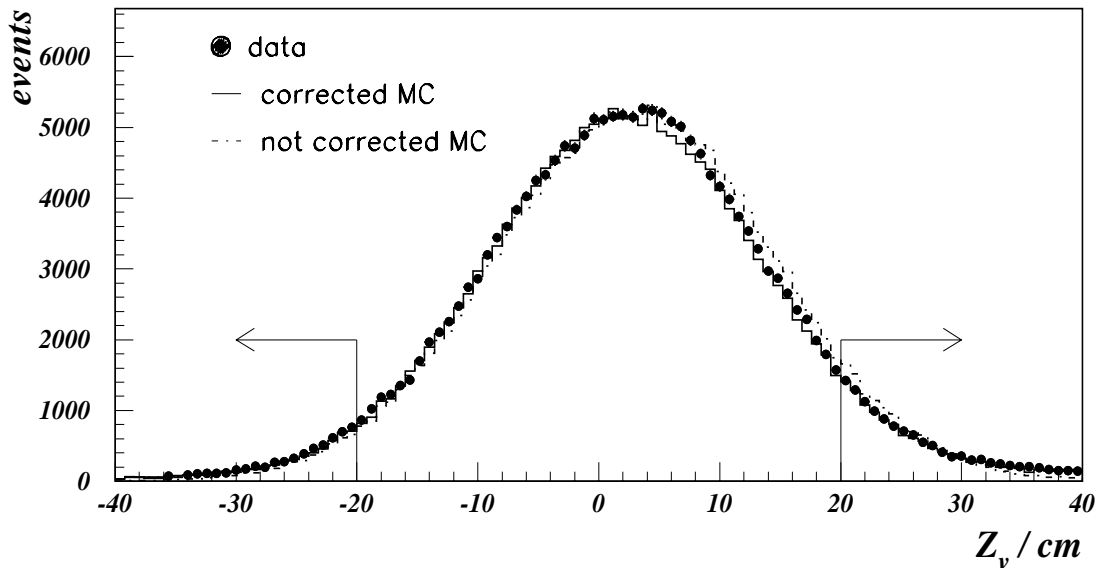


Figure 6.10: Distribution of the  $z$ -position of the interaction vertex in the data (closed circles) and in the  $z_v$ -reweighted Monte Carlo simulation (solid line). The hatched-dotted line represents the  $z$ -vertex distribution of the original Monte Carlo simulation. Also shown is the  $z$ -vertex cut when events outside  $\pm 20$  cm are rejected.

In Fig. 6.10 the distributions of the  $z$ -position of the event vertices measured with the BST are shown for the data and the Monte Carlo simulation. Its distribution was simulated with some initial parameters (hatched-dotted curve in the figure) which had

to be adjusted to the distribution in the real data. The tuning of the  $z$ -position of the interaction vertices has been performed by a  $z$ -dependent weighting of the simulated events assuming a Gaussian shape of the  $z$ -vertex distribution.

Application of the  $z$ -vertex cut requires so-called *satellite bunch corrections* due to the longitudinal structure of the HERA proton beam [104]. Besides the main bunch, corresponding to the interaction region, the proton beam has *early (backward)* and *late (forward)* satellite bunches, resulting in additional peaks of the  $z$ -vertex distribution shifted by  $\pm 70$  cm on average. The H1 luminosity system can not determine whether the Bethe-Heitler photon originated from the main or a satellite interaction region. Thus, the integrated luminosity had to be corrected on a fraction of the satellite bunches by  $5.4\%(\pm 1.5\%)$  [70]. This correction introduces the main normalization uncertainty of the measurement.

The DIS event generator DJANGO, used in the analysis, does not include simulation of elastic QED Compton events which can be considered as a background to DIS events. These events are characterized at low  $Q^2$  by no hadronic final state particles and no tracks in the CTD. Unfortunately, often the final state electron or the photon are lost in the backward beam hole, giving no possibility to clearly identify them in the data. These events were removed from the data by the requirement of the vertex measured with the central tracker detectors for  $y_e > 0.5$ , where the QED Compton background is located.

## 6.4 Estimation of the Photoproduction Background

“Photoproduction” are the processes of the electron-proton interaction by the exchange of a quasi-real ( $Q^2 < 0.01 \text{ GeV}^2$ ) photon. As a consequence of the extremely low  $Q^2$ , the final state electron is scattered with polar angle close to the incident one and thus usually lost in the beam pipe. The hadronic final state particles produced in a  $\gamma p$  process may, however, fake a low energetic DIS electron because of the high rate of photoproduction and the extended radial range of a true electron signal in SpaCal at low energies. A large part of the background is due to photons originating mainly from  $\pi^0 \rightarrow \gamma\gamma$  decays. Charged hadrons may also fake a low energetic electromagnetic cluster because of sometimes significant fluctuations in the development of the hadronic shower and/or overlap with a final state photon. The photoproduction background to DIS events becomes pronounced at energies of the electron cluster below about 12 GeV and then sharply rises towards lower energies corresponding to the high  $y$  kinematical domain.

For acceptance reasons only a small part (typically 10%) of the photoproduction events can be identified with the electron tagger (ET) calorimeter (see Section 3.2.1) which is located at -33 m behind the interaction point. Due to the magnetic field, only electrons with a certain energy (inelasticity) spectrum corresponding roughly to 10-20 GeV (0.2-0.7) can be measured in the electron tagger. Its acceptance as a function

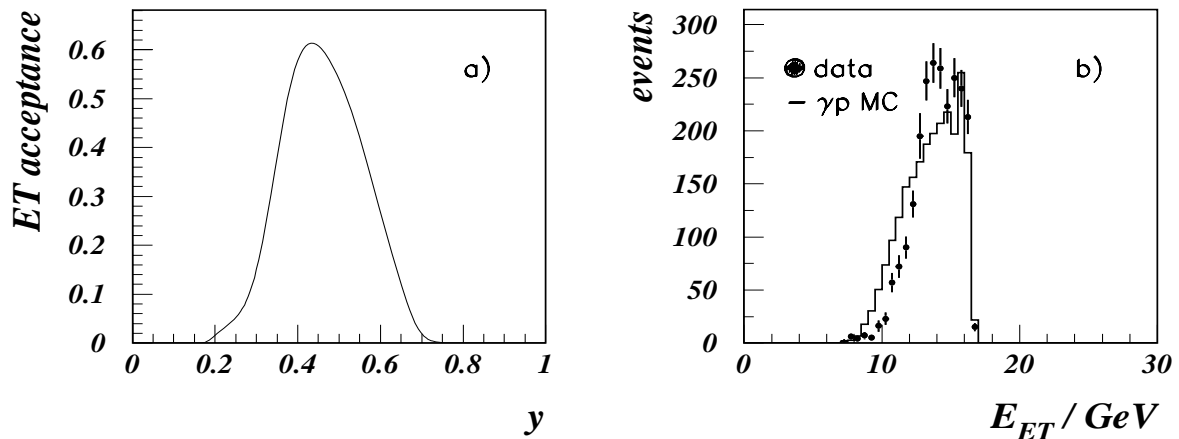


Figure 6.11: a) Acceptance of the electron tagger as a function of inelasticity. b) Energy distribution of the electrons measured with the electron tagger after all  $\gamma p$  selection cuts being applied (see text).

of  $y$  is shown in Fig. 6.11,a) which has a maximum at  $y \approx 0.45$ . The ET acceptance is calculated on a run dependent basis.

The photoproduction Monte Carlo program PHOJET has been used for the estimation of the remaining  $\gamma p$  events. Their contribution is then statistically subtracted from the data. A good description of the background by the Monte Carlo simulation is important since it directly affects the cross section measurement at high  $y$ . A sample of so-called tagged events was used to cross check the photoproduction event simulation.

In order to keep the background study as close to the DIS analysis as possible, all cuts listed in Table 6.1, besides the  $E - P_z$  cut, were applied. An event was considered to be tagged if the energy deposited in the electron tagger was greater than 7 GeV within the region of good containment of the electromagnetic shower. Additionally, the total  $(E - P_z)_{tag}$  was required to be greater than 45 GeV and the energy deposited in the photon detector to be less than 2 GeV. Here, the total  $(E - P_z)_{tag}$  represents the sum of the value of  $E - P_z$  measured in the central detector and the ones measured in the electron and photon detectors:

$$(E - P_z)_{tag} = (E - P_z) + 2(E_{ET} + E_{PD}). \quad (6.12)$$

The photoproduction event sample has a background represented by Bethe-Heitler DIS events which are characterized by  $(E - P_z)_{tag}$  values greater than 70 GeV. Therefore, an additional requirement on  $(E - P_z)_{tag}$  to be less than 70 GeV was applied.

In the framework of the H1SIM simulation program the electron tagger response was not simulated. Instead, the generated inelasticity has been used to reproduce the energy deposited by the final state electron. The electron tagger acceptance was simulated by weighting each of the generated photoproduction events with the function shown in Fig. 6.11,a). In Fig. 6.11,b) the comparison of the energy distributions of the final

state electron in the data and the photoproduction Monte Carlo shows an acceptable agreement.

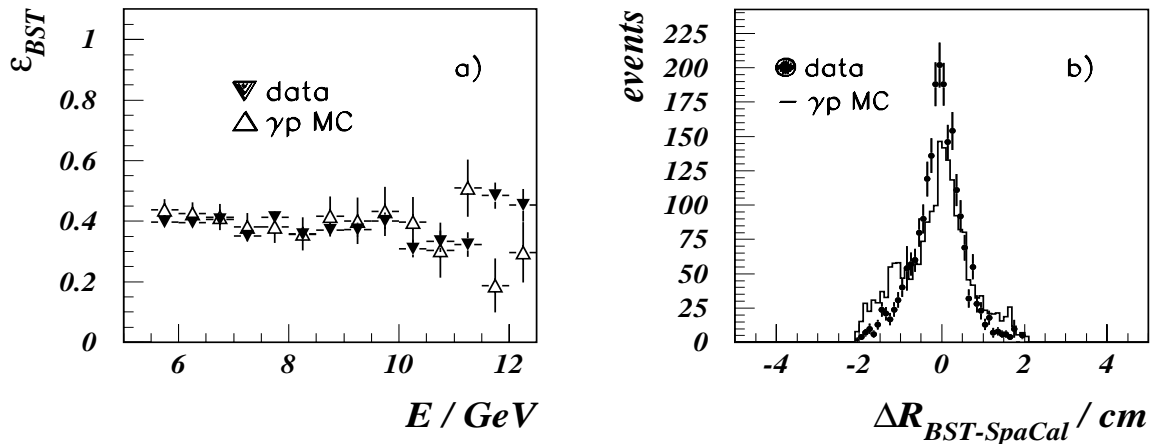


Figure 6.12: a) BST validation efficiency for the photoproduction background. The inefficiency represents the rejection power. Photoproduction background is reduced by a factor of about 2.5 in addition to the conventional DIS selection criteria. b) Matching between BST and SpaCal shown on the SpaCal plane. Poor agreement between photoproduction data and simulation made to open the matching criteria up to 2 cm to avoid possible bias in the cross section measurement.

The backward silicon tracker was used in addition to the standard DIS selection cuts to suppress the photoproduction background. The advantage of the BST is its insensitivity to neutral particles which form the main background to the electrons energy deposition. About 20% of the photons produced in  $\pi^0$  decays convert into  $e^+e^-$  pairs since the amount of dead material in front of the BST is small and defined mostly by the beam pipe<sup>3</sup>. Part of the electromagnetic clusters produced by  $\pi^0$  decays can be rejected by the radius cluster cut since the opening angle between the decay photons is increasing with decreasing energy of the original  $\pi^0$ . To a large extent not converted photons are rejected by requiring a track in the BST linked to the SpaCal cluster.

The rejection power of the BST was investigated by studying its efficiency for tagged events. In Fig. 6.12,a) the comparison of the BST efficiency between tagged data and the photoproduction Monte Carlo simulation is presented as a function of cluster energy. All selection cuts except the BST validation were applied. The study has been performed in the 4-out-of-4 geometrical region of the BST where a 95% external efficiency was obtained for high energetic electrons (see Section 4.6). A low BST efficiency corresponds to certain amount of background reduction. Both efficiencies agree well and show a rejection of 60% of the photoproduction background which passed through the standard DIS selection criteria. In other words, the BST suppresses the  $\gamma p$  background by an additional factor of about 2.5.

<sup>3</sup>In 1997/98 the Aluminum beam pipe ( $1.9\%X_0$ ) of the H1 experiment was replaced by a carbon fiber pipe of only  $0.6\%X_0$  which further reduced the conversion probability.

In principle, matching of a BST track with a SpaCal cluster allows also to reject part of the background due to charged hadrons. Since the fluctuations of the energy deposited in the electromagnetic section (which represents one interaction length, see Section 3.2.4) by the hadrons is large, it may lead to significant miscalculations of the cluster position. This feature may be utilized for an additional suppression of the photoproduction background using the precise angular measurement of the BST. Fig. 6.12,b) presents the radial matching of the cluster position in SpaCal with the measurements based on the BST track reconstruction for the data and the photoproduction simulation. While the matching in the data is rather symmetric around  $\Delta R_{BST-SpaCal} = 0$ , the simulated distribution is biased towards negative values. This tendency has been confirmed using the BDC angular measurement for the matching and comparing with the SpaCal cluster position reconstruction. It seems that the mismatching comes not from the BST measurement but can be related to some problems with the simulation and/or reconstruction of the hadronic clusters in the SpaCal. Up to now this question remains open. A loose cut on the matching with SpaCal of  $\pm 2$  cm has been applied in order to avoid a possible bias in the cross section measurement.

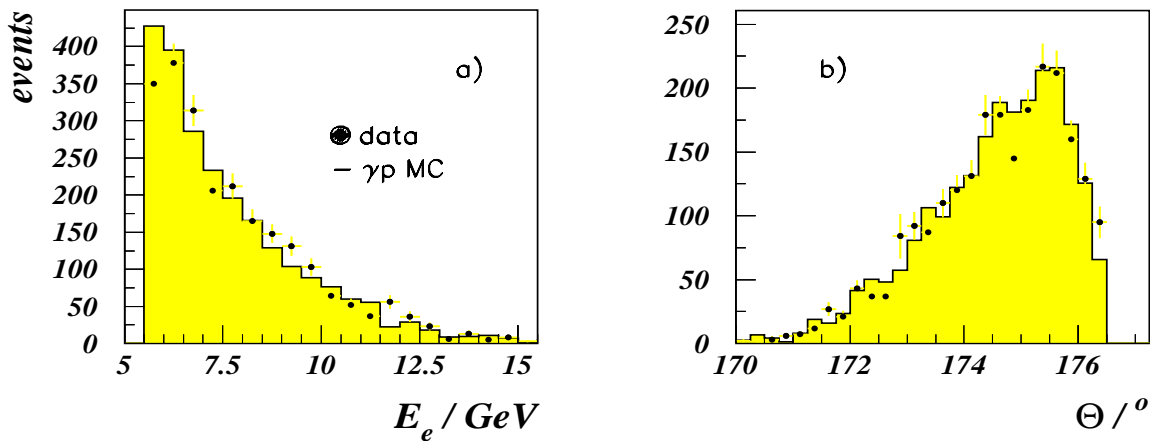


Figure 6.13: Energy (a) and polar angle (b) distributions for the tagged photoproduction events measured with the SpaCal and the BST, respectively, (closed circles), compared with the photoproduction simulation (histogram).

The sample of tagged events has been used to normalize the photoproduction background which passed the DIS selection criteria in the Monte Carlo simulation to the data. A normalization of  $0.9(\pm 2\%)$  was obtained. A systematic uncertainty of 30% was assigned to this value as a result of comparisons made with other analyses [105]. The energy and polar angle distributions for the photoproduction background measured with the SpaCal and the BST are depicted in Fig. 6.13,a) and b), respectively. The  $\gamma p$  distributions in data are well reproduced by the simulation.

Understanding of the high  $y$  kinematical domain at  $1.75 < Q^2 < 5.5 \text{ GeV}^2$  is demonstrated with some control distributions presented in Fig. 6.14. The distributions of the polar angle and energy of the scattered electron for  $y > 0.5$  are well described by the Monte Carlo simulation.

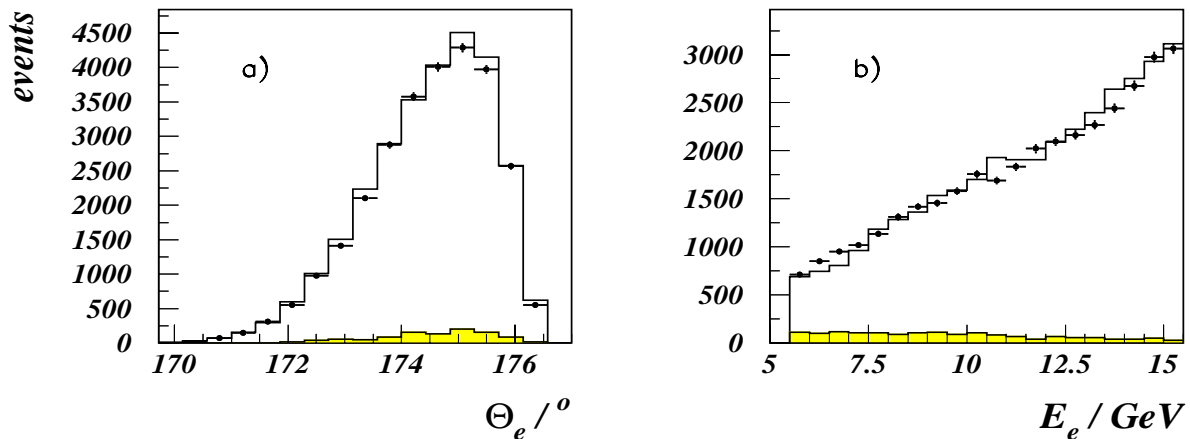


Figure 6.14: Control distributions for the high  $y$  kinematical domain ( $y > 0.5$ ). a) Polar angle and b) energy distributions for the scattered electron measured with the BST and the SpaCal.

## 6.5 Kinematic Distributions

Corrections based on detailed studies of the data were applied to the Monte Carlo simulation as described in the thesis. These corrections regard the BST efficiency (Sections 4.5 and 4.6), the electromagnetic and the hadronic energy scales of the SpaCal and the hadronic energy scale of the liquid argon calorimeter (Chapter 5) as well as the  $z$ -vertex reweighting. The cross section reweighting technique was used for the Monte Carlo adjustment in order to avoid a reprocessing of the DIS event sample comprising millions of events. It should be noticed here that the Monte Carlo reweighting has only very little influence on the DIS cross section measurement since the cross section assumptions largely cancel in the acceptance calculation (see Section 6.1). Yet, it is useful for cross checking purposes and controls whether the detector response is properly described in the Monte Carlo simulation.

Distributions of the main variables used for the cross section measurement and the extraction of  $F_2$  are shown in Fig. 6.15. The Monte Carlo distributions are normalized to the integrated luminosity of the data. All cuts listed in Table 6.1 are applied for the distributions shown.

In Fig. 6.15,b) the distribution of the inelasticity reconstructed with the  $\Sigma$  method is shown. The  $\Sigma$  method has been used for kinematics reconstruction for  $y < 0.15$  ( $\log(y) < -0.82$ ). Very good agreement between experimental and simulated distributions can be seen for this kinematical region. A discrepancy between data and Monte Carlo simulation for  $\log y > -0.8$  is related to edge effects of the analysis. Fig. 6.15,a) represents the composition of the  $y_h$  reconstruction according to the detector components. A correct description of the  $y_h$  fractions carried by different detector components is important for the estimation of the systematic uncertainty of the measured cross section. The sum of the fractions of  $y_h$  contributed by the *Tracks*, the *LAr* and the *SpaCal*

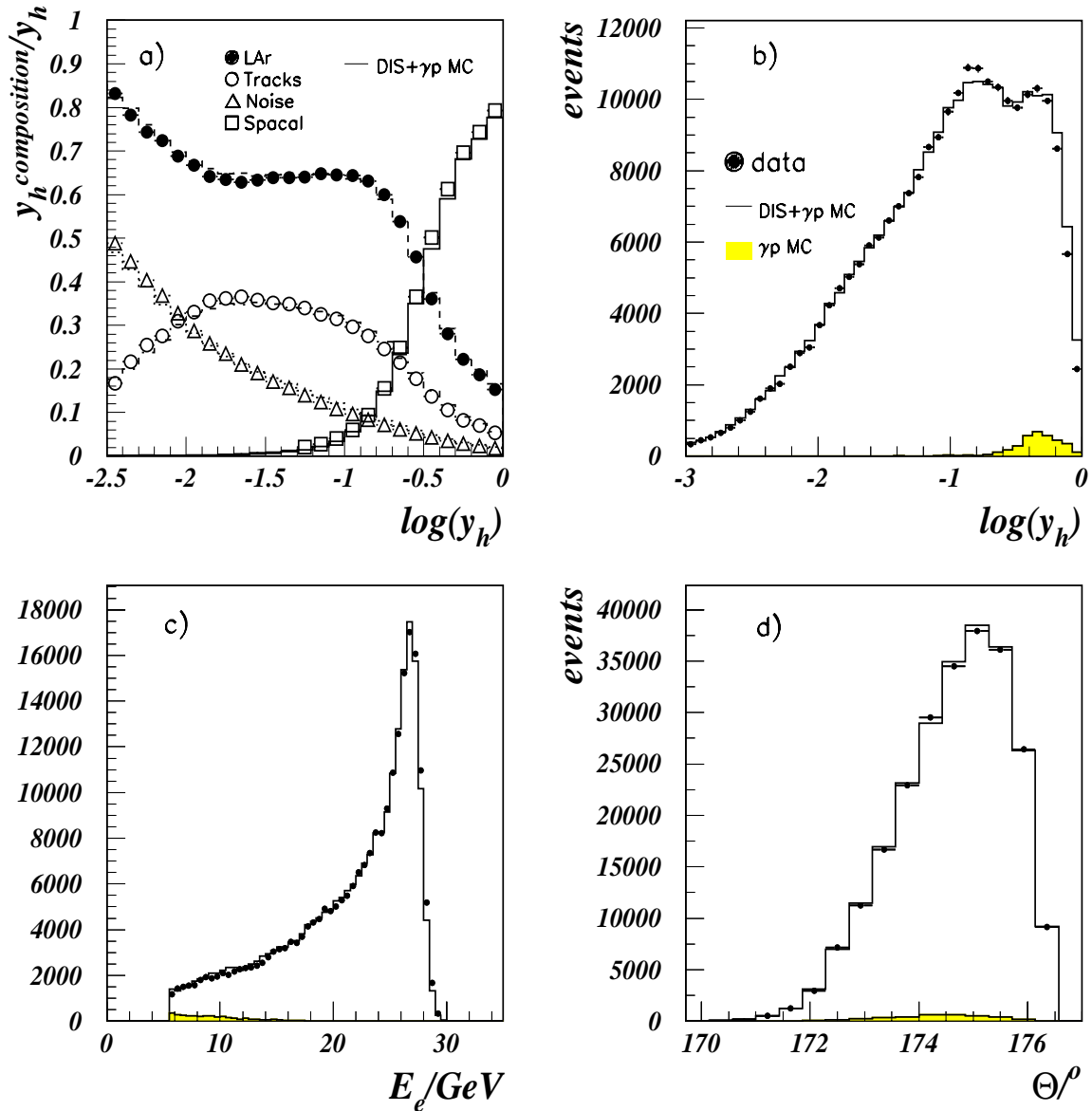


Figure 6.15: Control distributions of the most important quantities used in the analysis compared with the Monte Carlo simulation. a) Distributions of  $y_h$  components: LAr calorimeter, Tracks, SpaCal calorimeter and electronic noise. b) Distribution of inelasticity as reconstructed using the  $\Sigma$  method. c) and d), respectively, are the energy and polar angle distributions of the scattered electron.

is equal to unity. The three components are well described by the simulation. The fraction of  $y_h$  identified as calorimetric noise (open triangles) is also well reproduced in the Monte Carlo simulation. The noise simulation uses files taken from the data.

The distributions related to the kinematics reconstruction with the electron method are depicted in Fig. 6.15,c) and d) which show the energy and polar angle distributions of the final state electron, respectively. These two quantities are used for reconstruction of  $y_e$  and  $Q_e^2$ . Their experimental and simulated distributions agree well in the whole kinematical range within the BST acceptance. The energy distribution of the scattered electron in Fig. 6.15,c) is rather smooth although different thresholds are passed. A first threshold at  $E'_e = 24$  GeV is caused by the imposed  $P_t$  balance cut (see Section 6.3.4), a second one at  $E'_e = 17$  GeV is due to the  $E - P_z$  cut (see Section 6.3.3) and a third one at  $E'_e = 13.6$  GeV is the result of the QED Compton event suppression by the central vertex requirement for  $y_e > 0.5$  (see Section 6.3.6). The electron method has been used for the cross section measurement for  $y > 0.15$  corresponding to a scattered electron energy below 23.6 GeV.

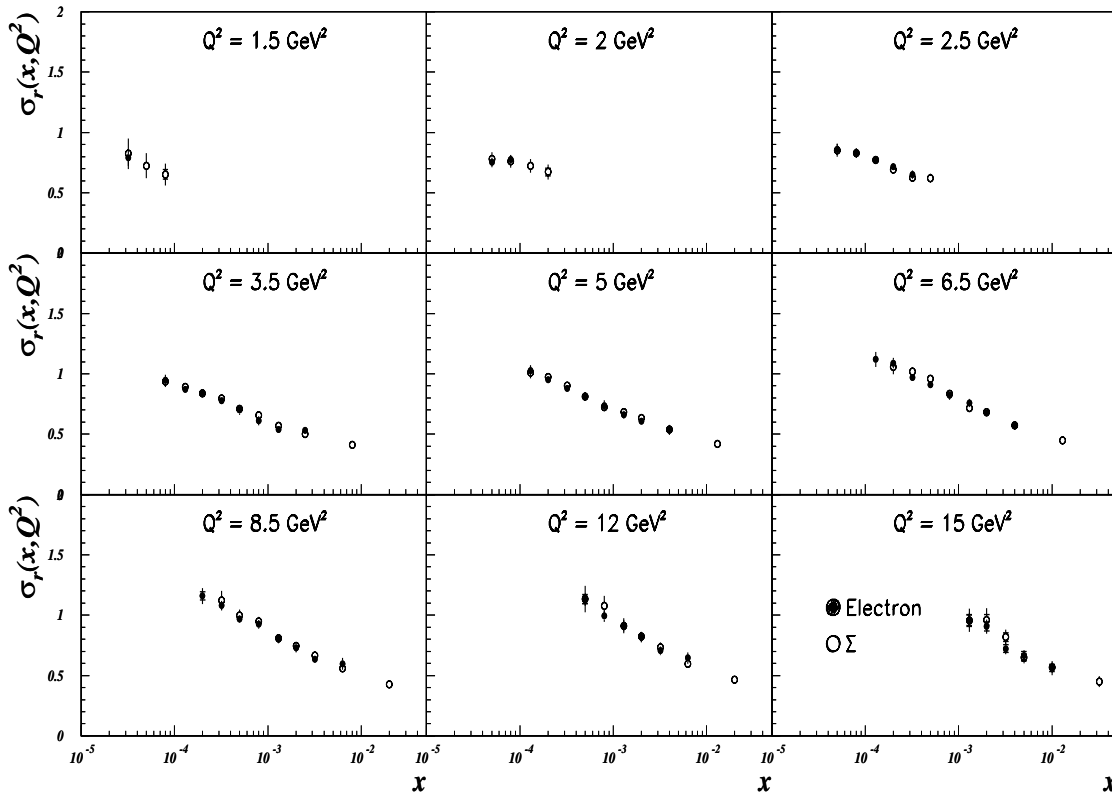


Figure 6.16: Reduced DIS cross section measured with the electron (closed circles) and  $\Sigma$  (open circles) methods shown for  $y < 0.6$ . The inner error bars denote the statistical uncertainty, the full error bars correspond to the systematic and the statistical errors added in quadrature.

The cross section determination has been performed using the two different methods (electron and  $\Sigma$ ). This allows not only to cross check the central values of the measured cross section but also to estimate part of the systematic errors. In Fig. 6.16

the comparison of the DIS cross sections determined by the electron and  $\Sigma$  methods are presented. Both results are in good agreement and some small deviations are within the quoted systematic errors. The fact that both cross sections agree so well, despite degrading resolutions at the edges of the  $y$  range, confirms the correct calibrations of the electromagnetic and hadronic energy scales.

## 6.6 Systematic Errors

The high statistics of the data allowed thorough studies of systematic effects described earlier in the thesis. Their influence on the cross section measurement was estimated using the Monte Carlo simulation. The systematic effects were separated into three error sources: global normalization uncertainties, kinematically correlated errors and local systematic errors being treated as uncorrelated errors. The following uncertainties were assigned:

- Global normalization uncertainties:
  1. An uncertainty of the integrated luminosity measurement of 1.5%;
  2. A 0.5% uncertainty of the 99% trigger efficiency;
  3. Part of the events rejected in the L4 filter farm was checked. A corresponding analysis is presented in [87]. The efficiency of the farm was found to be 99% with an uncertainty of 0.5%;
  4. The uncertainty coming from the imperfect description of the BST efficiency defined an additional global systematic error of 1% of the cross section measurement.
- Correlated errors:
  1. The uncertainties of 0.3% at  $E'_e$  above 17 GeV and 2% at 2 GeV were assigned to the electron energy scale for the SpaCal calorimeter. The uncertainty was treated as a linear function of  $E'_e$  interpolating between the results at 3 GeV and 17 GeV. This miscalibration leads to an about 1-2% uncertainty of the cross section measured with the electron method at  $y > 0.15$ . At lower values of the inelasticity the uncertainty rises up to 5%. Note that at  $y < 0.15$  the  $\Sigma$  method is used for the cross section measurement. The resulting uncertainty of the DIS cross section measurement with the  $\Sigma$  method is about 1-2%;
  2. The uncertainty of the hadronic energy scale comprises four sources of systematic errors corresponding to the  $y_h$  decomposition. These are: 1) the uncertainty of the LAr hadronic energy scale calibration of 2%(4%) for the central (forward) part of the calorimeter, 2) an uncertainty of 3% for the  $y_h$  fraction carried by tracks, 3) a 5% uncertainty of the SpaCal hadronic energy scale, 4) an uncertainty of 25% for the contribution of the electronic

noise from the special LAr noise suppression procedure. The resulting systematic error coming from the hadronic energy scale uncertainty takes into account the relative contribution of each source to the total hadronic final state energy. The quoted uncertainty of the hadronic energy scale leads to variations of the cross section, calculated by the  $\Sigma$ -method, of 1-2% in the  $y$  range 0.3-0.02. The uncertainty rises at the edge of the  $y$  acceptance up to 3-4%;

3. An uncertainty of 0.3 mrad for the polar angle reconstruction of the scattered electron was estimated from the residual dependence of  $\Delta\theta_{BST-BDC}$  on the azimuthal angle and the uncertainties of the alignment. This uncertainty has a small effect on the cross section measurement, basically within  $\pm 0.5-1\%$ . For  $Q^2 < 2.5$  GeV, this uncertainty rises up to 2-4%;
  4. An uncertainty of the electron identification with the maximum cluster energy criterion was estimated by replacing it with a maximum cluster transverse momentum criterion. The resulting cross sections were found to agree within 1% apart from at most 2% difference found at lowest  $Q^2$  and large  $y$ . The quoted numbers for the electron identification uncertainty were included into the final systematic error calculation;
  5. The beam induced background in the final event sample was negligible.
- Uncorrelated errors:
    1. The behavior of the BST acceptance is reproduced in the Monte Carlo simulation to better than 1% for  $Q^2 > 3.5$  GeV<sup>2</sup>. At lowest  $Q^2$  and large  $y$  the description of the acceptance worsens to 3% accuracy;
    2. The theoretical uncertainty on the amount of QED radiative corrections is estimated to be 1.5% up to maximum  $y$  values considered;
    3. The uncertainty of the photoproduction background subtraction procedure was estimated with the PHOJET simulation program. A comparison with independent analyses suggested the uncertainty of 30% for normalization of the remaining  $\gamma p$  background in the analysis bins. Some bins at high  $y$  contain up to 15% of the events which originated from photoproduction processes. This leads up to about 4.5% systematic error.

The total systematic error is obtained from the quadratic summation over each source of the uncorrelated systematic uncertainty added quadratically to the correlated ones and to the global normalization uncertainty. The total systematic error of the DIS cross section measurement is about 2-4%. At the edges of BST acceptance it rises up to about 5%. At high  $y$  the total systematic error reaches 7.5% mainly due to photoproduction background.

## 6.7 Results for the DIS Cross Section

### 6.7.1 Main Kinematic Region

The results of the cross section measurement presented in this thesis are given in Fig. 6.17,top and compared with the cross sections measured by H1 in the combined analysis of data collected in the years 1996-1997 [106]. The cross sections are compared for the electron and  $\Sigma$  methods within the acceptance of the presented analysis ( $1.5 \leq Q^2 \leq 15 \text{ GeV}^2$ ) for the inelasticity range  $0.6 \geq y \geq 0.003$ . The error bars represent the full error of the measurements calculated as quadratic sum over the statistical and systematic errors. The solid curves in the figure show the global NLO QCD fit to the reduced cross section of the H1 1996-1997 analysis. The dotted and the hatched lines represent the reduced cross sections calculated with assumption on  $F_L = 0$  and  $F_L = F_2$ , respectively.

The experimental precision of the results is defined by the high statistics of the measured and simulated events resulting in typically of 1-2% uncertainty and by the total systematic uncertainty of 2-5%. The rather small systematic error is mainly due to a precise SpaCal energy calibration, a reduced uncertainty of the angular measurement achieved with the BST and due to the improved calibration of the LAr hadronic energy scale. In comparison with previous H1 results of the inclusive  $ep$  DIS cross section measurements [107], limited to  $y > 0.01$ , the analysis presented in the thesis has been extended towards lower inelasticity values. The extension was made possible by the improved vertex reconstruction with the scattered electron measured in the BST. The non-equidistant sequence of points in the figure at low  $y$  corresponds to the binning which was re-adjusted to resolution (see Section 6.2). The lowest inelasticity value of the measured cross section is about  $y \approx 0.004$ .

Small differences between the reduced cross section measurements made by H1 based on the data collected in the years 1996-1997 and those obtained in the present analysis are demonstrated in Fig. 6.17,bottom. The closed circles depict the difference of the two results. The error bars in the figure correspond to the full errors obtained by adding the statistical and the systematic errors of the presented analysis in quadrature. As can be seen, discrepancies between both results are within 2-3% except for some local deviations.

### 6.7.2 Cross Section at high $y$

One of the prime tasks, the construction of the BST was devoted to, has been the measurement of the DIS cross section at high values  $y$  at low  $Q^2$ . According to Eq. 2.37, at high  $y$  the cross section becomes sensitive to the structure function  $F_L(x, Q^2)$ . The DIS cross section at high  $y$  has been measured by H1 with constantly increasing precision for  $8.5 \leq Q^2 \leq 35 \text{ GeV}^2$  since 1994 [108, 37, 71]. Results for lower  $Q^2$  beyond  $y = 0.6$  are obtained for the first time. In Fig. 6.18, the DIS cross section measured at  $y = 0.68$

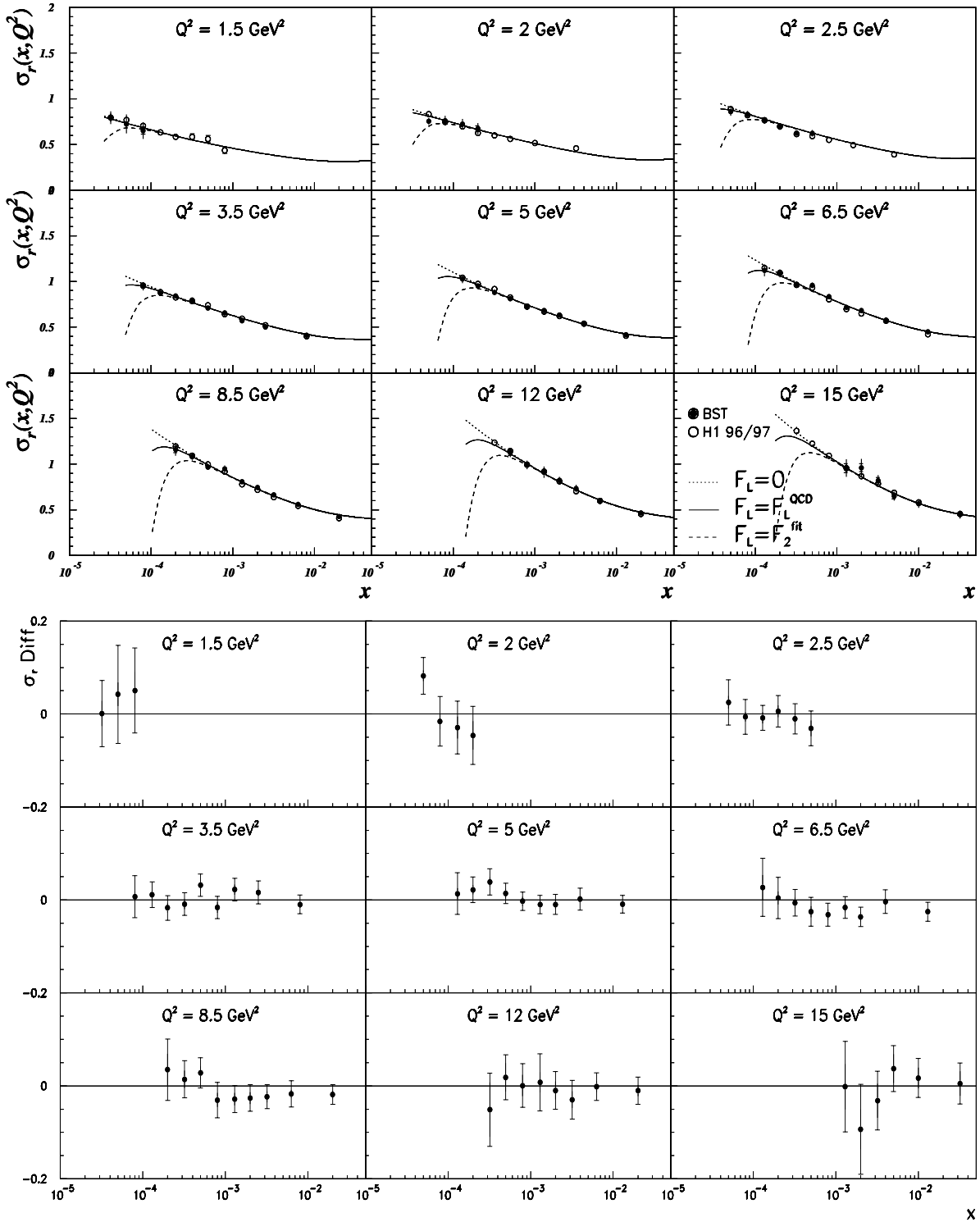


Figure 6.17: Top: *Reduced* DIS cross section ( $\sigma_r = \sigma/\kappa$ ) presented for  $y < 0.6$  as a function of  $x$  in different  $Q^2$  bins. The results obtained in this BST analysis are compared with the  $\sigma_r$  data measured by H1. The inner error bars denote, where visible, the statistical uncertainty and the full error bars represent the statistical and systematic uncertainties added in quadrature. Also shown are the curves corresponding to NLO QCD predictions for the reduced cross section with different assumptions on the structure function  $F_L$ . Bottom: Difference between these two data on reduced DIS cross section. The error bars represent the statistical and the systematic uncertainties of the presented analysis added in quadrature.

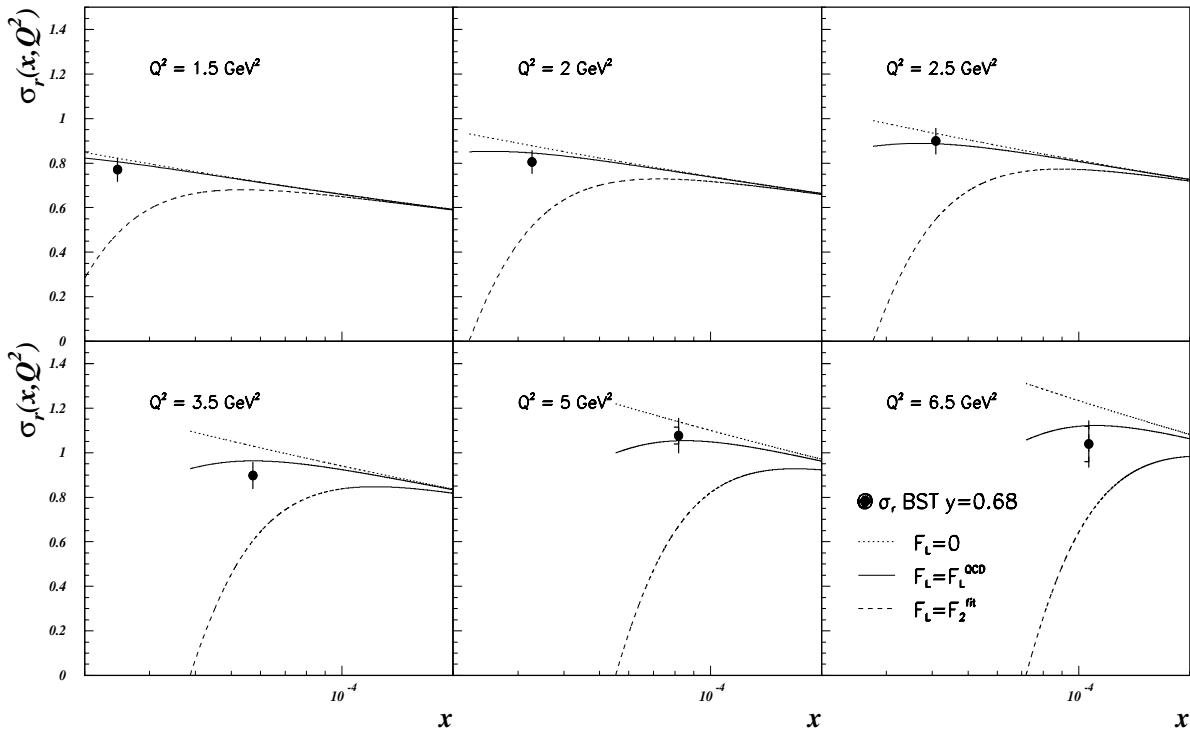


Figure 6.18: Reduced DIS cross section for  $y = 0.68$  presented in six  $Q^2$  bins. The inner error bars denote the statistical uncertainty and the full error bars represent the systematic and statistical uncertainties added in quadrature. Also shown are the curves corresponding to different assumptions on the structure function  $F_L$ .

is presented in six  $Q^2$  bins corresponding to the kinematical range of  $1.5 \leq Q^2 \leq 6.5$   $\text{GeV}^2$ . The solid curve in the figure shows the result for the reduced cross section obtained from the global NLO QCD fit. The dotted and the hatched lines represent the reduced cross sections with assumptions  $F_L = 0$  and  $F_L = F_2$ , respectively. The full error bars represent the quadratic sum of the statistical and the systematic errors. The systematic error is dominated by the uncertainty of the photoproduction background and the BST acceptance at large polar angles of the scattered electron.

The measured DIS cross section shown in the figure agrees within the quoted errors with the NLO QCD expectation. This measurement implies that the structure function  $F_L(x, Q^2)$  differs from its extreme limits. Its behavior is consistent with the NLO QCD. The reduced cross section tends to approach its limit for  $F_L = 0$  with decreasing  $Q^2$ . This reflects the fact that  $F_L$  should vanish like  $Q^4$  in the limit  $Q^2 \rightarrow 0$ , i.e. faster than  $F_2$ .

The result of this analysis for  $Q^2 = 2, 2.5$  and  $3.5$   $\text{GeV}^2$  were used for an extraction of the structure function  $F_L(x, Q^2)$  which was found to agree with the NLO QCD calculation [71] (for details see also [62]).

## 6.8 Extraction of $F_2$

A well established technique for extracting the structure function  $F_2(x, Q^2)$  from the measured DIS cross section is based on some assumption on the function  $R(x, Q^2)$  introduced in Section 2.2.1 or the structure function  $F_L(x, Q^2)$ . The choice of  $R$  or  $F_L$  is equivalent since:

$$F_2(x, Q^2) = \sigma_r(x, Q^2) + \frac{y^2}{Y_+} F_L(x, Q^2) = \sigma_r(x, Q^2) \left( 1 - \frac{y^2}{Y_+} \cdot \frac{R(x, Q^2)}{1 + R(x, Q^2)} \right)^{-1}. \quad (6.13)$$

In this analysis, the extraction of the structure function  $F_2(x, Q^2)$  was performed with an assumption on  $R(x, Q^2)$ <sup>4</sup> based on NLO QCD predictions obtained from the global fit of the H1 1996-1997 data and the ones of NMC [109].

In Fig. 6.19 the result for the  $F_2(x, Q^2)$  structure function obtained from this analysis (closed circles) is shown together with the result of the standard H1 1996-1997 analysis (open circles). Both results are in good agreement as expected from the comparison of the two cross section results presented in Fig. 6.17, bottom. The function  $R(x, Q^2)$  used for the  $F_2$  extraction was the same for both analyses. The curve in the figure is the structure function  $F_2(x, Q^2)$  evaluated from the NLO QCD fit to the cross section. The results are well described by the NLO QCD curve.

The results of the structure function  $F_2(x, Q^2)$  measurement are given in Tables 6.2 and 6.3 together with the reduced cross section  $\sigma_r(x, Q^2)$  they were extracted from. Also listed are the values of the function  $R(x, Q^2)$  used. The errors of the measurement are represented by their statistical and systematic components. The full errors are calculated by adding the statistical and systematic errors in quadrature.

---

<sup>4</sup>The structure function  $F_L(x, Q^2)$  has not been measured so far directly at HERA. This requires to run HERA with different proton energies [110, 111]. A separation between the  $F_2$  and  $F_L$  contributions to the DIS cross section is then possible, when comparing the data with fixed  $(x_c, Q_c^2)$  but different  $y = Q^2/(4xE_e E_p)$ .

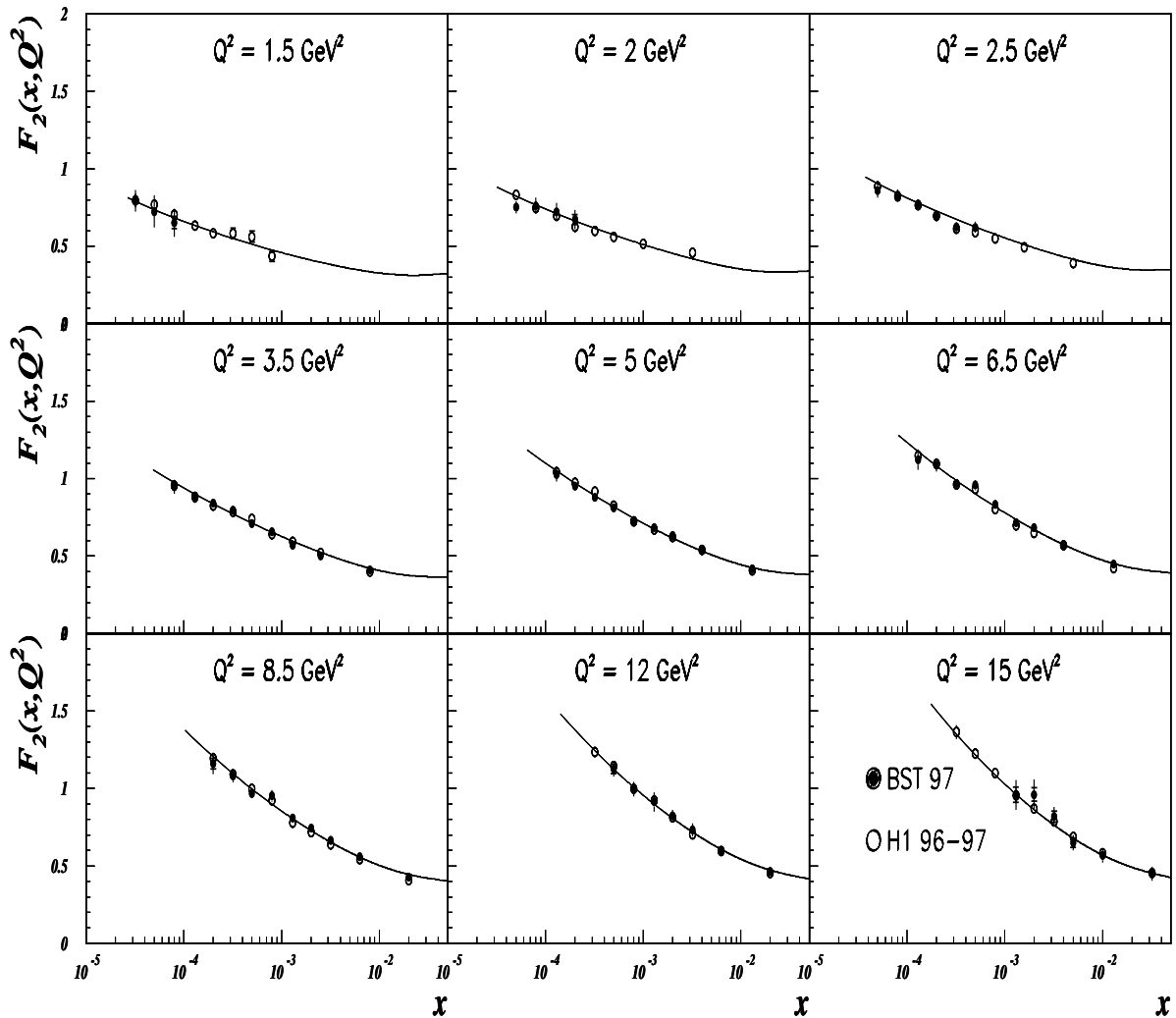


Figure 6.19: The proton structure function  $F_2$  presented as a function of  $x$  in different  $Q^2$  bins. The result of the analysis (closed circles) is compared with standard H1 analysis (open circles) based on the data collected in the years 1996 and 1997 [71]. Where visible, the inner error bars denote the statistical uncertainty and the full error bars represent the systematic and the statistical uncertainties added in quadrature.

$Q^2$	$x$	$y$	$\sigma_r$	$F_2$	$R$	$\delta_{stat}$ [%]	$\delta_{unc}$ [%]	$\delta_{cor}$ [%]	$\delta_{syst}$ [%]	$\delta_{tot}$ [%]
1.5	0.000025	0.6750	0.770	0.786	0.05	1.7	5.4	5.1	7.4	7.6
1.5	0.000032	0.5178	0.785	0.793	0.05	3.4	5.1	4.6	6.9	7.7
1.5	0.000130	0.1275	0.730	0.731	0.06	9.4	8.4	10.7	13.6	16.6
1.5	0.000200	0.0828	0.461	0.461	0.07	12.9	12.1	10.2	15.8	20.4
2.0	0.000033	0.6750	0.805	0.835	0.10	1.5	5.1	4.8	7.0	7.1
2.0	0.000050	0.4419	0.742	0.752	0.10	1.5	3.4	2.2	4.0	4.3
2.0	0.000080	0.2762	0.770	0.774	0.11	2.8	3.2	2.2	3.8	4.8
2.0	0.000130	0.1699	0.762	0.764	0.11	7.5	4.2	3.6	5.5	9.3
2.0	0.000200	0.1105	0.672	0.672	0.12	4.6	4.1	7.8	8.8	9.9
2.5	0.000041	0.6750	0.899	0.945	0.14	1.6	4.9	4.7	6.8	7.0
2.5	0.000050	0.5523	0.835	0.861	0.14	1.6	3.4	2.1	4.0	4.3
2.5	0.000080	0.3452	0.820	0.829	0.14	1.2	3.1	2.1	3.7	3.9
2.5	0.000130	0.2124	0.771	0.774	0.15	1.5	2.5	1.8	3.0	3.4
2.5	0.000200	0.1381	0.690	0.691	0.16	1.8	2.6	4.1	4.9	5.2
2.5	0.000320	0.0863	0.623	0.624	0.17	2.3	2.8	3.5	4.5	5.0
2.5	0.000500	0.0552	0.623	0.623	0.18	2.8	3.0	4.6	5.4	6.1
3.5	0.000057	0.6750	0.898	0.959	0.19	2.1	4.9	3.7	6.1	6.5
3.5	0.000080	0.4833	0.921	0.948	0.19	1.2	3.0	2.0	3.6	3.8
3.5	0.000130	0.2974	0.865	0.873	0.19	1.1	2.2	2.0	3.0	3.2
3.5	0.000200	0.1933	0.839	0.843	0.20	1.2	2.3	1.9	2.9	3.2
3.5	0.000320	0.1208	0.794	0.795	0.21	1.3	2.3	1.6	2.8	3.1
3.5	0.000500	0.0773	0.709	0.709	0.22	1.5	2.4	2.3	3.3	3.6
3.5	0.000800	0.0483	0.658	0.658	0.23	1.7	2.4	2.1	3.3	3.7
3.5	0.001300	0.0297	0.569	0.569	0.24	1.9	3.9	2.4	4.6	5.0
3.5	0.002510	0.0154	0.503	0.503	0.26	1.5	4.8	2.0	5.3	5.5
3.5	0.008000	0.0048	0.409	0.409	0.30	1.7	4.9	2.3	5.4	5.7
5.0	0.000082	0.6750	1.077	1.165	0.22	3.2	5.0	3.2	6.0	6.8
5.0	0.000130	0.4249	1.001	1.027	0.23	1.2	3.0	2.0	3.6	3.8
5.0	0.000200	0.2762	0.943	0.952	0.23	1.1	2.2	1.6	2.7	2.9
5.0	0.000320	0.1726	0.874	0.877	0.24	1.1	2.2	2.1	3.0	3.2
5.0	0.000500	0.1105	0.811	0.812	0.24	1.2	2.2	0.8	2.4	2.7
5.0	0.000800	0.0690	0.726	0.726	0.25	1.3	2.3	0.7	2.4	2.7
5.0	0.001300	0.0425	0.683	0.683	0.26	1.5	2.3	1.1	2.5	2.9
5.0	0.002000	0.0276	0.633	0.633	0.26	1.5	3.8	1.1	3.9	4.2
5.0	0.003980	0.0139	0.538	0.538	0.28	1.3	4.8	1.1	4.9	5.1
5.0	0.013000	0.0042	0.418	0.418	0.28	1.5	4.8	2.5	5.4	5.6

Table 6.2: Results of the DIS cross section measurement represented by its *reduced* quantity  $\sigma_r = \sigma/\kappa$ . Also given are the values of the extracted structure function  $F_2$ . The experimental error  $\delta_{tot}$  is split into the statistical error  $\delta_{stat}$  and the systematic error  $\delta_{syst}$ . The systematic error incorporates two main components: the uncorrelated error  $\delta_{cor}$  and the correlated error  $\delta_{unc}$  which are added in quadrature.  $R$  represents values of  $R(x, Q^2)$  used for the extraction of the structure function  $F_2$ .

$Q^2$	$x$	$y$	$\sigma_r$	$F_2$	$R$	$\delta_{stat}$ [%]	$\delta_{unc}$ [%]	$\delta_{cor}$ [%]	$\delta_{syst}$ [%]	$\delta_{tot}$ [%]
6.5	0.000106	0.6750	1.039	1.130	0.24	7.0	5.5	1.8	5.8	9.1
6.5	0.000130	0.5523	1.064	1.119	0.24	2.4	3.2	2.3	4.0	4.6
6.5	0.000200	0.3590	1.069	1.089	0.25	1.3	3.0	1.6	3.4	3.6
6.5	0.000320	0.2244	0.963	0.969	0.25	1.2	2.2	1.7	2.8	3.0
6.5	0.000500	0.1436	0.955	0.957	0.25	1.3	2.2	1.9	2.9	3.2
6.5	0.000800	0.0898	0.834	0.835	0.26	1.3	2.2	1.4	2.6	3.0
6.5	0.001300	0.0552	0.715	0.715	0.26	1.4	2.3	1.8	2.9	3.2
6.5	0.002000	0.0359	0.683	0.683	0.27	1.5	2.3	1.1	2.6	3.0
6.5	0.003980	0.0180	0.573	0.573	0.27	1.2	4.8	1.3	4.9	5.1
6.5	0.013000	0.0055	0.448	0.448	0.26	1.5	4.8	2.7	5.5	5.7
8.5	0.000200	0.4695	1.118	1.159	0.26	2.9	3.3	2.3	4.0	5.0
8.5	0.000320	0.2934	1.066	1.079	0.26	1.7	2.3	1.1	2.5	3.1
8.5	0.000500	0.1878	0.965	0.969	0.26	1.5	2.3	2.0	3.0	3.4
8.5	0.000800	0.1174	0.950	0.951	0.26	1.6	2.3	2.9	3.7	4.0
8.5	0.001300	0.0722	0.808	0.808	0.26	1.6	2.3	2.2	3.2	3.6
8.5	0.002000	0.0469	0.745	0.745	0.26	1.7	2.5	2.3	3.3	3.8
8.5	0.003200	0.0293	0.663	0.663	0.27	1.8	3.8	1.7	4.2	4.6
8.5	0.006310	0.0149	0.559	0.559	0.26	1.5	4.8	2.3	5.3	5.5
8.5	0.020000	0.0047	0.428	0.428	0.22	2.0	4.9	3.2	5.8	6.2
12.0	0.000320	0.4142	1.254	1.288	0.26	4.6	3.7	2.1	4.3	6.2
12.0	0.000500	0.2651	1.116	1.127	0.26	2.7	2.6	0.8	2.8	3.9
12.0	0.000800	0.1657	0.992	0.996	0.26	2.3	2.5	2.5	3.5	4.2
12.0	0.001300	0.1020	0.912	0.913	0.26	2.4	2.6	5.1	5.7	6.2
12.0	0.002000	0.0663	0.822	0.822	0.26	2.4	2.5	2.6	3.6	4.3
12.0	0.003200	0.0414	0.731	0.731	0.26	2.5	2.6	4.0	4.8	5.4
12.0	0.006310	0.0210	0.599	0.599	0.25	2.0	3.8	2.9	4.8	5.2
12.0	0.020000	0.0066	0.464	0.464	0.21	2.6	5.0	3.8	6.3	6.8
15.0	0.001300	0.1275	0.957	0.959	0.26	5.1	3.4	8.2	8.8	10.2
15.0	0.002000	0.0828	0.960	0.961	0.26	4.5	3.4	8.4	9.0	10.1
15.0	0.003200	0.0518	0.818	0.818	0.25	4.5	3.3	5.6	6.5	7.9
15.0	0.005000	0.0331	0.649	0.649	0.25	4.8	3.4	4.2	5.4	7.2
15.0	0.010000	0.0166	0.565	0.565	0.23	4.0	5.2	4.6	6.9	8.0
15.0	0.032000	0.0052	0.449	0.449	0.16	5.9	5.7	5.2	7.8	9.7

Table 6.3: Results of the DIS cross section measurement represented by its *reduced* quantity  $\sigma_r = \sigma/\kappa$ . Also given are the values of the extracted structure function  $F_2$ . The experimental error  $\delta_{tot}$  is split into the statistical error  $\delta_{stat}$  and the systematic error  $\delta_{syst}$ . The systematic error incorporates two main components: the uncorrelated error  $\delta_{cor}$  and the correlated error  $\delta_{unc}$  which are added in quadrature.  $R$  represents values of  $R(x, Q^2)$  used for the extraction of the structure function  $F_2$ . For further details we refer to the text.

## 6.9 Concluding Remarks

The installation of the backward silicon tracker has successfully completed the upgrade of the backward part of the H1 detector. A complete study of the BST was performed in this work comprising track reconstruction, alignment, efficiency investigation and electron finding. The results described in this thesis have been used by H1 in the standard analysis of the minimum bias run taken in the fall 1997. Together with the significantly improved statistical precision of the cross section measurement (typically 1-2%) they helped to decrease the systematic uncertainty down to 2-3% which is roughly by a factor of 2 better than the earlier published results [107].

Use of the BST gave a further suppression of the photoproduction background by a factor of 2.5 as compared to standard DIS selection criteria. This permitted to decrease the systematic error on the remaining  $\gamma p$  background down to about 4% in the high  $y$  domain.

Improved calibration of the forward part of the LAr calorimeter using DIS events with a single electron track and vertex reconstructed in the BST has permitted to measure the structure function  $F_2$  down to  $y \approx 0.004$ . It, thus, overlaps with fixed target experiment results. The proton structure function data measured by H1 and NMC agree very well with each other and also with the NLO QCD fit. The CCFR data derived from neutrino-iron scattering are larger by about 15% [106]. This led to a reanalysis of the CCFR data. With a new treatment of the charm contribution the new CCFR result agrees better with NMC and H1 [112].

Completion of the H1 cross section measurement at low  $Q^2$  will be based on the following improvements:

- An upgrade of the backward silicon tracker was made. Additional four planes with silicon strip sensors were mounted in front of the ones described in this thesis. The acceptance of the upgraded, so-called BST2, tracker now overlaps with the central tracker detectors and the dependence on fiducial cut problems at the edges of the  $\theta$  acceptance is less important;
- One eight plane sector of the BST2 was equipped with strip sensors which permit to measure the charge of low momentum tracks. This allows to extend the *charge subtraction* method used for estimation of the photoproduction background in the CJC acceptance towards the low  $Q^2$  region. The *charge subtraction* method is preferable in comparison with the one used in this work, since it depends less on the Monte Carlo simulation of the photoproduction processes. This advantage is believed to help in reaching the highest  $y$  kinematic domain at low  $Q^2$  which has not been accessed so far. This is of particular interest since the sensitivity to  $F_L$  improves proportional to  $y^2$ ;
- The possible discovery of a *saturation* of the structure function  $F_2$  at low  $x$  demands a precise knowledge about the structure function  $F_L$  which has not been directly measured so far in H1. Its measurement requires running HERA with different proton energies;

- A new minimum bias run was taken in December 1999 with the upgraded backward silicon tracker and integrated luminosity of about  $3.8 \text{ pb}^{-1}$ . This is about a factor of 2 more than the data presented here. The increased statistical precision will allow to perform a more precise study of the systematics which should permit to further reduce the uncertainty in the high  $y$  kinematic region.

# Chapter 7

## Summary

A measurement of the inclusive  $ep$  DIS cross section is presented in the  $1.5 \leq Q^2 \leq 15$  GeV<sup>2</sup> kinematic domain covered by the Backward Silicon Tracker (BST) of the H1 experiment at HERA. In the presented thesis the BST has been used for the first time in the analysis of inclusive cross section data collected during a short run taken in the fall of 1997. The integrated luminosity of the data is 1.85 pb<sup>-1</sup> resulting in typically 1-2% statistical precision of the results. A description of this new detector is given in the first part of the thesis following an overview of the H1 apparatus.

A special DIS electron finding algorithm was developed and has been used by H1 in the standard analysis of the combined data taken during the 1996-1997 HERA run periods. This algorithm is based on the validation of an electron cluster candidate in the SpaCal calorimeter with tracks reconstructed in the BST which are linked to the cluster. The algorithm comprises two independent approaches. This allowed to cross check the reconstruction and linking procedures utilized. Systematic studies gave an about 1% accuracy of the algorithm performance. A detailed description of the “BST electron finder” is given in Appendix A.

The developed electron finder was used in studies of the alignment of the BST and its efficiency. The alignment of the BST was utilized for systematic studies of the BDC alignment. This confirmed a precision of 0.3 mrad of the polar angle measurement based on the Backward Drift Chamber BDC and the interaction vertex.

The hadronic energy scale calibration of the LAr calorimeter is described in detail. The calibration was performed with two independent methods making use of the BST by reconstructing the event vertex from the scattered electron at low  $Q^2$ . This has been essential for the determination of the hadronic energy scale at low transverse momenta as well as for calibrating the forward part of the LAr calorimeter. A comparison of the hadronic energy scale obtained with two different methods between two independent analyses justified a systematic error of 2% of the hadronic energy measurement made by the LAr calorimeter.

The event selection criteria used for the measurement of the inclusive  $ep$  DIS cross section were presented. Each of the applied cuts was investigated in detail and compared with Monte Carlo simulations. Special emphasis was put to the investigation of

the remaining photoproduction background which complicates the cross section measurement at high  $y$ . It has been shown that the use of the BST permits to reduce the  $\gamma p$  background in the analysis by a factor of 2.5 additionally to standard DIS selection cuts. The uncertainty of the remaining background is estimated to be 30% resulting in an about 4% systematic error for the cross section measurement.

It was found that former discrepancies between measured and simulated data in the low  $y$  kinematical domain are related to *double counting* of events simulated with  $5 < W_{gen} < 10$  GeV due to a DJANGO limitation ( $W_{gen} > 5$  GeV). The problem was solved by using the HERWIG event generator for average treatment of the resonance region with  $W_{gen} < 5$  GeV.

The inclusive  $ep$  DIS cross section was measured using two different methods, namely the electron and the  $\Sigma$  method, for reconstruction of the kinematic variables  $x$  and  $Q^2$ . Both results are in agreement with each other within the quoted systematic errors. Finally, the structure function  $F_2$  was extracted.

The comparison of the cross section analyses presented in this thesis and the ones obtained in the standard H1 analysis of the 1996-1997 data confirms the 2-3% precision of the latter. The measured cross sections are in good agreement with a NLO QCD fit. The results of the cross section measured at  $y = 0.68$  for low  $Q^2$  presented in this thesis have been used in the determination of the structure function  $F_L$ . The results for  $F_L$  are found to be consistent with the NLO QCD expectation.

Altogether it has been demonstrated that the BST, used as a stand-alone tracker, together with the SpaCal calorimeter permitted a precise measurement of the cross section. It was of considerable use in the angular measurement, electron identification and even for the LAr calibration in the very low  $y$  region. Extension of the BST from 4 to 8 planes and two dimensional  $(r, \phi)$  track reconstruction will be of much use for the further analyses.

# Appendix A

## BST Electron Finder

### A.1 Introduction

This Appendix is devoted to a DIS electron finding procedure using the BST measurement of final state charged particles scattered within its angular acceptance. Clear identification of the final state DIS electron as well as substantial suppression of the photoproduction background are the crucial tasks for a precise measurement of the inclusive  $ep$  DIS cross section. The electron finding algorithm described here has been used by the H1 collaboration in the standard low  $Q^2$  analysis of the data collected in the years 1996 and 1997 [71]. An improvement of the systematic uncertainty by a factor of two has been obtained in comparison with previous results of the H1 collaboration.

### A.2 Objectives of the procedure

The standard BST track reconstruction BSTREC implemented in the H1 reconstruction code (H1REC) is solely based on the measurement of the charge induced in its active volume by traversing charged particles. In 1997 the BST consisted of silicon sensors with concentric  $r$ -strips allowing for the polar angle measurement only (see Section 4.2). Since the BST axis does not coincide with the beam axis which defines the physical coordinate system, excentricity corrections to the BST angular measurement must be applied. As will be shown later in the text, these corrections, however, require knowledge on the azimuthal angle of a track whose measurement could not be provided by the BST itself and must be taken from SpaCal.

BSTREC gives a comprehensive information about every track reconstructed in the entire silicon telescope. In practice, the measurement of the DIS cross section requires a clear identification of the scattered electron in the BST acceptance and a measurement of its kinematic parameters. This demands an accurate alignment of the tracker. The cross section measurement requires that the angular resolution, efficiency and acceptance of the BST are correctly described in the simulation. Therefore, a

compact and fast code is needed for the electron track reconstruction. Also this permits systematic studies to be easily performed on the analysis level.

Two independent methods for the BST track reconstruction and linking to a SpaCal electron candidate cluster were developed in this analysis. Comparison of the results obtained with these methods allows to cross check both algorithms and gives additional information about the electron finding procedure. The first method is based on a so-called *corridor approach* and is applicable only if an event vertex exists well measured with the central trackers. The second method uses a *semi-combinatorial approach* with backward error propagation. It has no limitations arising from the event kinematics. Both methods will be described in detail in the following sections.

### A.3 General Description of the Routine

The BST electron finder was developed for the validation of an electron candidate cluster in the SpaCal calorimeter. The validation proceeds with a search for a track in the BST unambiguously linked to the SpaCal cluster.

The electron finder can be implemented into the H1PHAN standard physics analysis program and might be called on DST level and in an Ntuple based analysis. In order to run the BST electron finder on Ntuples, the user should store a selected number of BST hits from the bank BRSE. The choice of the number is up to the user and depends on the facilities he has. In this analysis up to 70 hits were stored preselected in a  $\pm\pi/4$  azimuthal angle range around a SpaCal cluster.

The electron finder routine BSTELF is called with the following syntax:

```
CALL BSTELF(XV, YV, ZV, DZV, XS, YS, ZS, ES, IVTX,
+ THB, THVB, NDF, ZOEL, DZOEL, ZOBS, ZOVB, RSP, LVAL)
```

where the first string contains the input variables and the second one represents the output parameters of the routine. These are defined as follows:

- **input variables:**

- XV, YV and ZV are the  $x$ ,  $y$  and  $z$  positions of the central tracker vertex, respectively, and DZV is the uncertainty of the  $z$ -vertex measurement. IVTX is a vertex type which has to be provided by user. IVTX is unity for a well measured central vertex and zero otherwise;
- XS, YS and ZS correspond to the  $x$ ,  $y$  and  $z$  positions of an electron candidate cluster in SpaCal and ES is its reconstructed energy.

- **output parameters:**

- LVAL is a validation flag which has three possible values: 9 means the SpaCal cluster is out of the BST acceptance, 0 means the cluster is not validated and 1 corresponds to a validated cluster;
- For every validated cluster the corresponding track information from the BST is given by the polar angle of the linked track (THB) in the H1 coordinate system, the number of degrees of freedom <sup>1</sup> (NDF) and the reconstructed  $z$ -position of the event vertex (Z0EL). The uncertainty of the  $z$  vertex reconstruction is represented by DZ0EL;
- An additional useful information is represented by the polar angle of the track obtained from a combined fit of the BST hits with the central vertex (THVB), the  $z$ -position of the event vertex obtained from a combined fit of the BST hits with the SpaCal cluster position (Z0BS) or with the central vertex itself (Z0VB);
- The parameter RSP represents a matching of the cluster position between the BST angular measurement and the SpaCal reconstruction, calculated on the SpaCal  $x, y$ -plane:

$$RSP = \tan(THB)(ZS - ZV) - \sqrt{(XS - XV)^2 + (YS - YV)^2}. \quad (\text{A.1})$$

The output parameters are the result of reconstruction and linking procedures performed by one of two algorithms which will be described next. The choice of the algorithm depends on the central vertex existence.

## A.4 Case 1: central vertex exists

If the event vertex is measured with the central trackers <sup>2</sup> and a reasonable uncertainty of its value is provided (chosen to be less than 0.3 cm) then a corridor on the BST with a possibly detected track is well constrained by this vertex and the SpaCal cluster position. In order to start the search for a track in the BST, the track and the acceptance of the track reconstruction are to be defined:

- **track definition:** The use of the SpaCal cluster position and (optionally) the event vertex position as a reference points allows to define a track using two well fitted hits in the BST, contrary to the standard BST stand-alone reconstruction where at least three hits are required. The high signal-to-noise ratio whose averaged value is equal to about 12 (see Section 4.4) permits an effective electronic

---

<sup>1</sup>ndf is calculated as a sum over number of BST hits used in the track fit plus the SpaCal cluster minus two.

<sup>2</sup>This is usually the case for the inelasticity range  $0.05 < y < 0.5$ , where mostly greater than two hadronic final state particles scatter into CTD acceptance providing more than 98% vertex reconstruction efficiency (see Section 6.2).

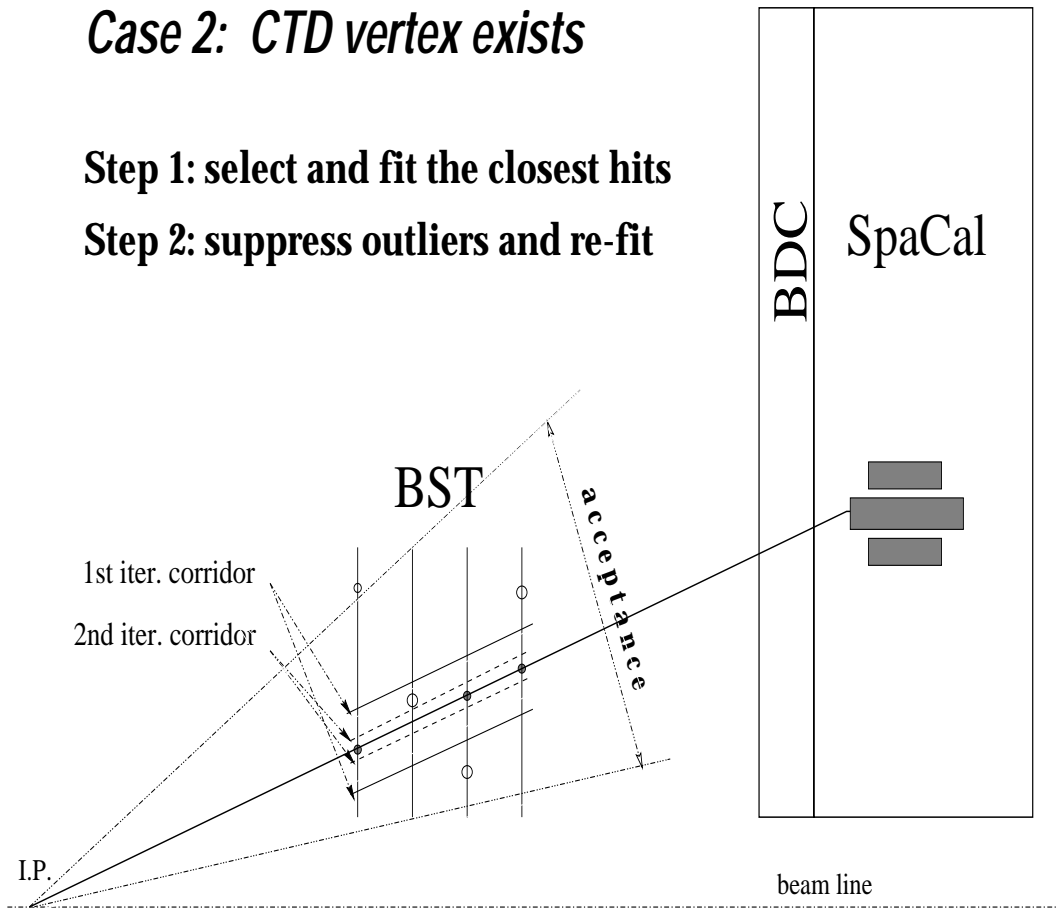


Figure A.1: Illustration of the electron finding procedure for the case when the central vertex exists. The transverse view of the backward part of the H1 detector is schematically represented by the BST (four vertical lines in the center), BDC and SpaCal (two boxes on the right side). A cluster of filled boxes illustrates the electron candidate cluster in the SpaCal is to be validated. The open circles in the BST denote noise hits rejected in the procedure whereas the closed ones correspond to the hits assigned to the electron track. This is depicted by the line connecting these hits, the interaction point (I.P.) and the SpaCal cluster. The BST acceptance, defined by the requirement of crossing at least two planes, is represented by dotted lines. Searching corridors are schematically illustrated by the solid and hatched lines, corresponding to the first and second iterations, respectively (for details see the text).

noise suppression such that the remaining noise made a distortion on the one per mill level. The reduction of the number of hits used for the track reconstruction allows to increase the tracker efficiency by roughly 5% taking into account the single hit efficiency of 92% (see Section 4.5);

- **acceptance definition:** The acceptance of the BST measurement is defined by the requirement of two hits needed for the track reconstruction. In Fig. A.1 the acceptance definition is schematically illustrated. The angular acceptance is limited by the inner radius (5.9 cm) of the sensors belonging to the third BST plane and by the outer radius (12.04 cm) of the sensors from the second BST plane. The acceptance has been calculated via the following relations:

$$\begin{aligned} R_3^{BST} &= \tan(\theta_{sz}) (Z_3 - ZV) + R_v \cos(\phi_{sz} - \phi_v) > 5.9 \text{ cm}, \\ R_2^{BST} &= \tan(\theta_{sz}) (Z_2 - ZV) + R_v \cos(\phi_{sz} - \phi_v) < 12.04 \text{ cm}, \end{aligned} \quad (\text{A.2})$$

where

$$\begin{aligned} \theta_{sz} &= \arctan \left( \frac{\sqrt{(XS-XV)^2 + (YS-YV)^2}}{ZS-ZV} \right), \\ \phi_{sz} &= \arctan \left( \frac{YS-YV}{XS-XV} \right) \end{aligned} \quad (\text{A.3})$$

are the polar and azimuthal angles of the track, respectively. These are calculated using the SpaCal cluster position measurement and the event vertex. The second term in Eqs. A.2 represents the correction due to the beam shift relative to the H1 coordinate system. Here,  $R_v = \sqrt{XV^2 + YV^2}$  and  $\phi_v = \arctan(YV/XV)$  define the vertex position in a cylindrical coordinate system.

If a track is out of the BST acceptance, the validation flag LVAL is set to 9 and the procedure finished. Otherwise, the event is subject to the main algorithm.

The uncertainty of the cluster position in the SpaCal as well as of the  $z$ -vertex position define the corridor for the search of the hits in the BST. The SpaCal spatial resolution is illustrated in Fig. A.2 as a function of the cluster energy. As can be seen, the resolution in data (closed circles) is about 0.35 cm down to about 10 GeV of deposited energy whereas for lower energies a steep rise of the cluster position uncertainty up to 0.85 cm at 4 GeV is observed in the DIS Monte Carlo simulation (open circles). The SpaCal spatial resolution of a definitely electromagnetic cluster is about 0.25 cm at large  $E$  and reaches 0.5 cm at 4 GeV. The SpaCal spatial resolution was parameterized as a function of cluster energy. User can define then the matching criteria himself.

Basically, the SpaCal spatial resolution defines the width of the track search corridor since the  $z$ -vertex reconstruction uncertainty is dominated by a factor  $\tan(\theta_{sz})$  coming from the projection on the track direction. The width of the corridor is calculated for each plane by partial differentiation of Eqs. A.2 yielding the following result:

$$\sigma_i^{corr} = DZV \cdot \frac{Z_i - ZS}{(ZS - ZV)^2} \cdot R_{Sp} \oplus \sigma_{R_{cl}}(E) \cdot \frac{Z_i - ZV}{ZS - ZV}, \quad (\text{A.4})$$

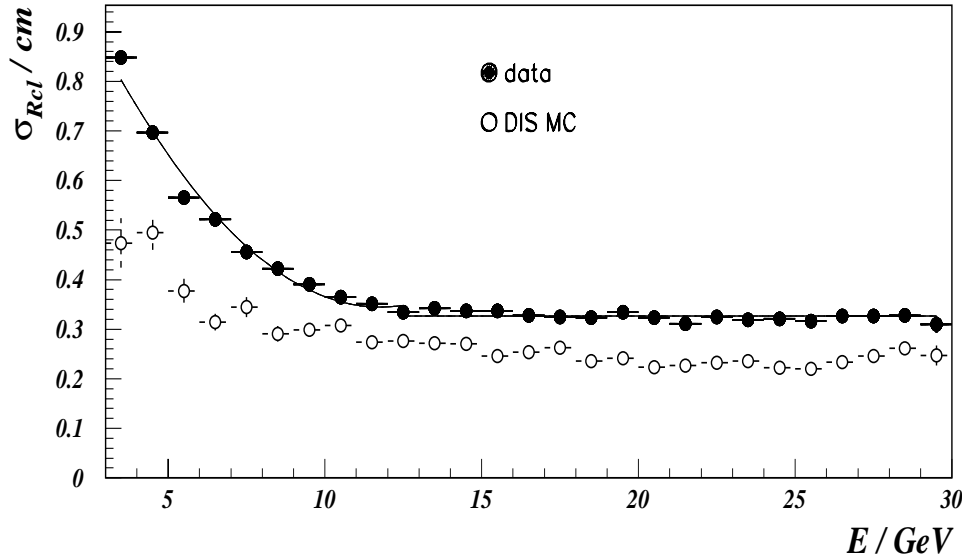


Figure A.2: The SpaCal spatial resolution as a function of electron candidate cluster energy. Closed (open) points represent the spreads of Gaussian fit performed to the distribution of the quantity  $R_{BDC}^{onSpaCal} - R_{SpaCal}$  in energy slices for data (DIS Monte Carlo simulation). The larger deterioration in the data may be due to residual  $\gamma p$  background in the data sample.

where  $Z_i$  means a  $z$  position of BST plane  $i$  and  $\sigma_{R_{cl}}(E)$  represents the parameterization of the SpaCal spatial resolution as a function of the cluster energy. The symbol  $\oplus$  in Eq. A.4 stands for quadratic summation.

The algorithm proceeds with a selection of the BST hit closest to the prediction calculated by Eq. A.2 for each plane within  $\pm 3\sigma_i^{corr}$  corridor in the sector defined by the azimuthal angle measured in the SpaCal. The BST hits are reconstructed in the H1 coordinate system. Since the physics analysis requires to work in the beam coordinate system, the BST hits receive an excentricity correction calculated via the following relation:

$$R_{beam} = \sqrt{R_{H1}^2 - R_v^2 \sin^2(\phi_{sz} - \phi_v)} - R_v \cos(\phi_{sz} - \phi_v). \quad (\text{A.5})$$

If two or more hits are found within the corridor band then the electron candidate cluster is supposed to be preliminary validated. Otherwise, the validation flag LVAL is set to zero and the procedure is stopped.

The reconstruction of the track parameters is performed with a straight line fit<sup>3</sup> to the selected hits. A special error function of the hits was invented to suppress the so-called outliers:

$$\delta R_n = \delta r_{BST} \oplus \sigma_i^{corr} \sqrt{2\pi} \left[ 1 - \exp \left( -\frac{1}{2} \left[ \frac{\Delta R_{sz-BST}}{\sigma_i^{corr}} \right]^2 \right) \right], \quad (\text{A.6})$$

where  $n$  is the number of the hit belonging to the plane  $i$ . Here,  $\delta r_{BST}$  corresponds to the spatial resolution of the BST and equals to 16  $\mu\text{m}$ .  $\Delta R_{sz-BST}$  is the difference of the predicted and the measured radial position of the hit.

The obtained slope and intercept of the straight line are used to refine the hit selection procedure. A second iteration starts with a reset of the validation flag. All previously selected hits are dropped. Now, the searching corridor is narrowed down to 300  $\mu\text{m}$  and the result of the fit from the first iteration is used to predict the hit positions in the BST. Most of the outliers are rejected in the second iteration as schematically shown in Fig. A.1. This allows to drop the error function A.6 used in the first iteration and to use the BST spatial resolution while re-fitting the newly selected hits. The final results for the polar angle of the track and for the reconstruction of the  $z$ -vertex position are calculated according to the following equations:

$$THB = \pi + \arctan(B) \quad \text{and} \quad Z0EL = -A/B, \quad (\text{A.7})$$

where  $A$  and  $B$  are the intercept and the slope of the straight line, respectively, which have been obtained from the fit of the selected hits. The other output parameters are obtained from fits to the combined set of the hits selected in the BST with the SpaCal cluster position or including the event vertex.

## A.5 Case 2: central vertex does not exist

As was described in Section 6.2, for inelasticity  $y < 0.05$  the hadronic final state particles are emitted with polar angles mainly below the acceptance of the central trackers. Due to this fact, the central vertex can not be reconstructed or, if reconstructed, then with an unacceptably high uncertainty. At  $y > 0.5$  the hadronic final state particles are scattered backward and miss the angular acceptance of the central trackers. The decrease of vertex reconstruction efficiency at high  $y$  is, however, not so dramatic due to the fact that the hadronic final state is badly collimated and often some particles are scattered into the CTD. The multiplicity of the hadronic final state is usually low at high  $y$ . Thus, it often does not permit to reconstruct the event vertex with high precision.

The subject of this section is the search algorithm for BST hits linked to the SpaCal electron candidate cluster disregarding the existence of the central vertex. This algorithm is implemented as a subroutine in the main code and is called after all necessary excentricity corrections to the BST hits and SpaCal cluster position are done.

---

<sup>3</sup>This is a good approximation for  $\theta$  down to transverse momenta of 0.1 GeV ( $E'_e = 2$  GeV and  $\theta_e = 177^\circ$ ) of the scattered electron. At this value of the transverse momentum, the reconstruction of the polar angle with a straight line fit gives a bias of about 0.3 mrad.

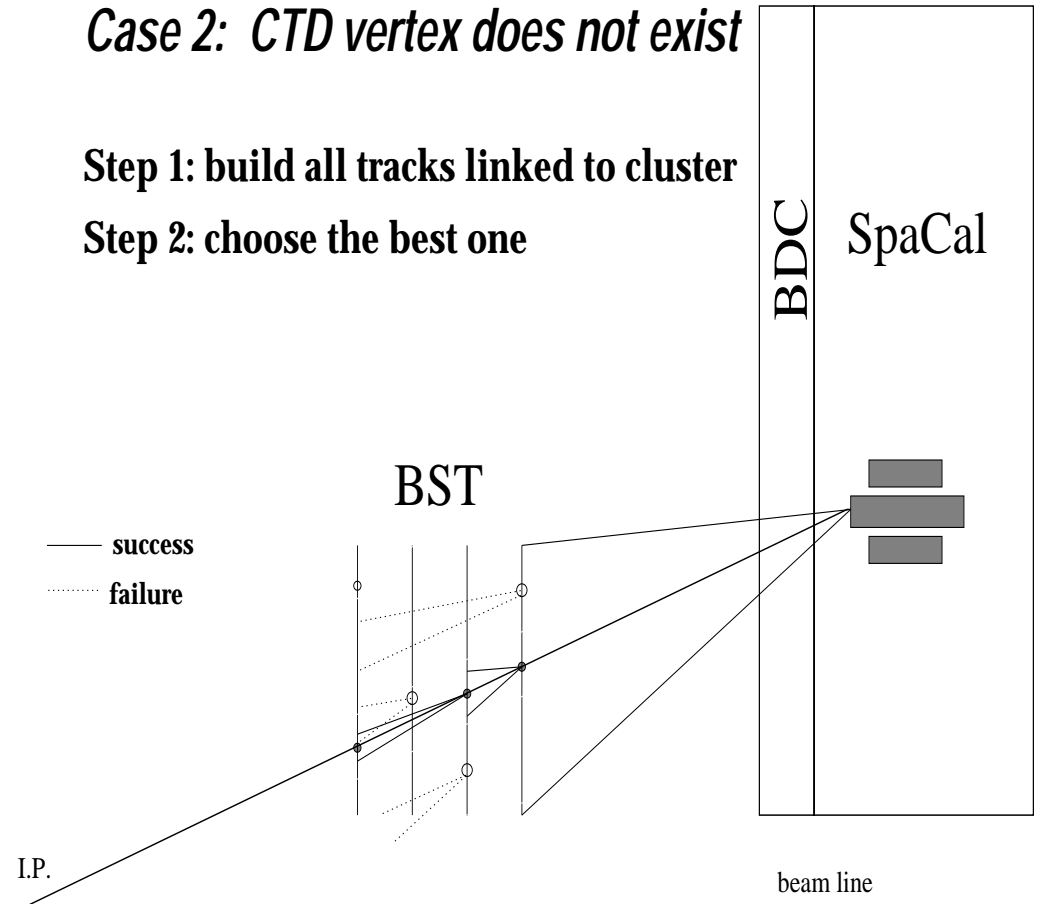


Figure A.3: Illustration of the electron finding procedure disregarding the central vertex existence. The transverse view of the backward part of the H1 detector is schematically represented by the BST (four vertical lines in the center), BDC and SpaCal (two boxes on the right side). A cluster of filled boxes illustrates the electron candidate cluster in the SpaCal to be validated. The open circles in the BST are noise hits rejected in the procedure whereas the closed ones correspond to hits assigned to the electron track which is depicted by the line connecting these hits and extrapolated forwards to the interaction point (I.P.) and backwards to the SpaCal cluster. The opening angles represent the propagated errors which define the search corridors for the BST hits. The successful search is depicted by the solid opening angles whereas unsuccessful ones are represented by the dotted lines (details see in the text).

The search for a track in the BST starts from the electron candidate cluster in the SpaCal which has certain radial resolution  $\sigma_{R_{cl}}(E)$ . This cluster defines the azimuthal angle and thus selects a  $\phi$  sector of the BST for possible track reconstruction. Each hit in the three planes closest to SpaCal is connected by a straight line to the cluster center. This line is extrapolated to the next plane and a closest hit is accepted if it is within a  $5\sigma_{ij}$  corridor defined by the SpaCal spatial resolution via the following relation:

$$\sigma_{ij} = \sigma_{R_{cl}}(E) \cdot \frac{Z_j - Z_i}{Z_i - ZS}, \quad (\text{A.8})$$

where  $Z_j$  and  $Z_i$  are the  $z$  positions of the BST plane  $i$  and  $j$ .

Once the second BST hit was found, the SpaCal information is not used anymore. The following evaluation of the track candidate is based solely on the BST itself. The two found hits are used to predict the next radial position of possible hit by the usual straight line extrapolation. Due to the very high precision of the radial measurement of the BST ( $16 \mu\text{m}$ ), the next hits are searched within  $100 \mu\text{m}$  around the prediction and this corridor is kept constant for simplicity. A schematic representation of the method is illustrated in Fig. A.3. Usually, from one to three track candidates are build in this way. They are checked not to be horizontal or to have a negative polar angle. Finally, the track with a maximum number of assigned hits is chosen.

The hits assigned to the chosen track are transferred to the main program and they are subject for the straight line fits as described in the previous section.

## A.6 Results

The work presented in this thesis is based on the developed “BST electron finder”. For the main results obtained with this code we refer to Chapters 4 and 6. This section is devoted to the internal consistency of the track reconstruction and linking procedures performed with the two independent methods.

For the cross check a sample of events with a well measured  $z$ -vertex with an uncertainty of less than  $0.3 \text{ cm}$  was selected. In Fig. A.4,a) and b) the comparison of the BST acceptance and its external efficiency as a function of the polar angle obtained with the two methods is presented. Both efficiencies represent a good agreement within 1% of the systematic uncertainty whereas the uncertainty of the BST acceptance is rising up to 3% at large polar angles of the scattered electron. This fact was taken into account in the quoted systematic error of the cross section measurement.

The DIS Monte Carlo simulation gives a precise information about the final state electron which allows to check the correctness of the performed electron track reconstruction. The measurement of the scattered electron polar angle is a crucial task of the procedure described here since it is essential for correct reconstruction of the event kinematics and thus the cross section measurement itself. In Fig. A.5,a) the difference between the generated polar angle of the scattered electron and the one reconstructed

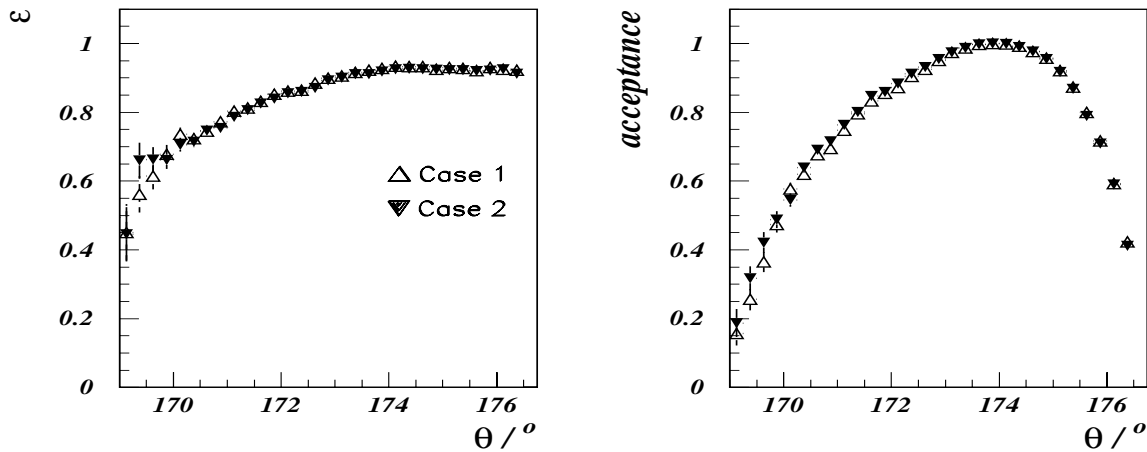


Figure A.4: Comparison of the BST efficiency (left figure) and acceptance (right figure) between the two approaches used in the electron finding procedure.

with the corridor method of the “BST electron finder” is presented for three different assigned hit numbers. For a cross check, the same events were reconstructed with the semi-combinatoric method and the difference with the generated polar angle of the scattered electron is depicted in Fig. A.5,b), also given for three hit numbers. The same comparison was done for the reconstruction of the event vertex. In Fig. A.6,a) and b) the precision of the vertex reconstruction is compared between the two different approaches.

From these comparisons the following conclusions can be drawn:

- Both methods give nearly identical results in terms of:
- the **polar angle** of the final state electron: its reconstruction is unbiased with a resolution of better than 0.33 mrad for 2 or more hit combinations (see Fig. A.5);
- the **z-position** of the event vertex: this is also reconstructed in an unbiased way with a resolution of better than 0.36 cm. Taking into account the  $z$ -vertex uncertainty of about 0.2 cm measured with the central trackers, the quoted value of the BST  $z$ -vertex reconstruction uncertainty in the Monte Carlo simulation, corresponds to the one obtained for data (see Fig. 4.13,b));
- the **efficiency** is reproduced well within the quoted 1% systematic error whereas **acceptance** uncertainty is rising up to 3% on its outermost edges.

Since both methods were proven to agree with each other very well, the semi-combinatorial approach for electron finding was used in the analysis. This made this analysis truly independent of the central tracker vertex reconstruction.

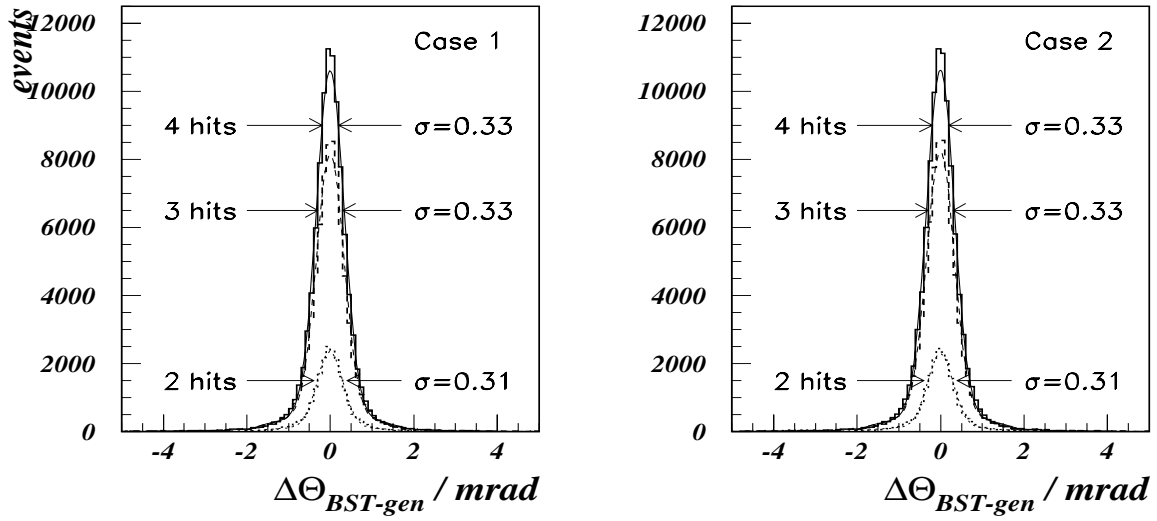


Figure A.5: Comparison of the reconstructed electron polar angle with the generated one performed within the corridor (left figure) and semi-combinatoric (right figure) approach. The comparison is shown for 2, 3 and 4 BST hits defining the electron track.

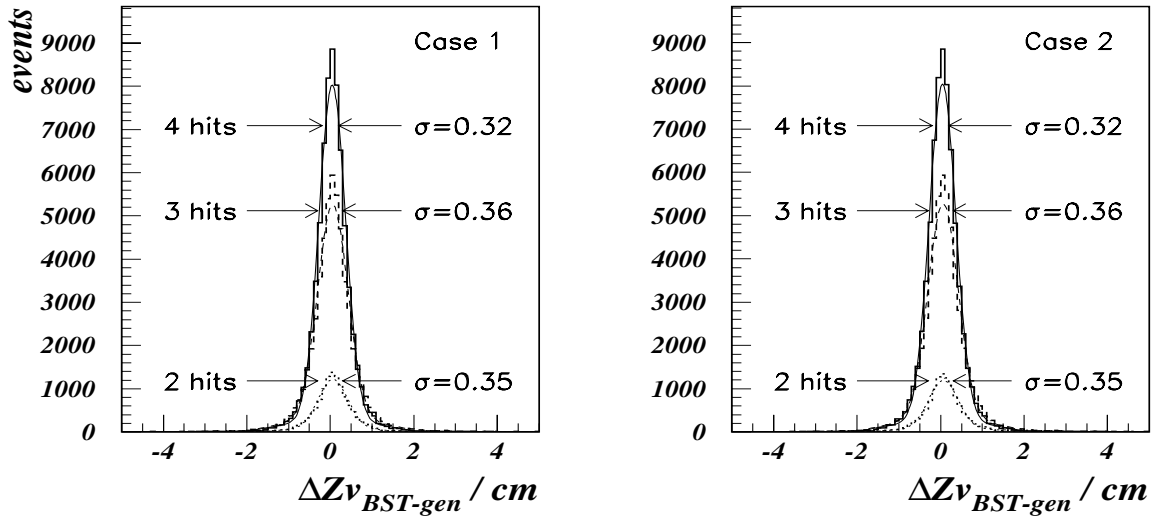


Figure A.6: Comparison of the  $z$ -vertex reconstruction performed within the corridor (left figure) and semi-combinatoric (right figure) approaches. The comparison is shown for 2, 3 and 4 BST hits defining the electron track reconstruction.

# Acknowledgments

First of all I would like to express my sincere gratefulness to my “doctor father” Dr. Max Klein for his permanent support and encourage in doing this work. His high level of requirements helped to form a critical view on any investigation. Special thanks are addressed to the former director of DESY-Zeuthen Prof. Dr. Paul Söding and to his successor Dr. Ulrich Gensch for giving me the possibility to work in this institute.

I wish to thank my colleagues from the H1 group in the institute who introduced me to the technical details of the Backward Silicon Tracker and its operation in the H1 detector: H. Henschel, P. Kostka, R. Lahmann, W. Lange, A. Meissner and M. Winde. An exclusive thanks goes to Th. Naumann for the exciting discussions while working on the tracker alignment and the development of the “BST electron finder” which were of great value for me.

The development of the electron finder allowed me to join the ELAN physics working group whose members introduced me the secrets of the physics analysis. Here, I would like to thank V. Shekelyan, A. Zhokin, A. Meyer, F. Lehner, U. Bassler, G. Bernardi, J. Philips B. Heinemann and T. Kurča. I would like to address a special thanks to A. Wegner and V. Lendermann whose criticism helped to improve the performance of the “BST electron finder”. Especially, I wish to thank my closest colleagues D. Eckstein and R. Wallny with whom I shared all the difficult and exciting moments of the research.

In the separate paragraph, I wish to express my deep respect and gratefulness to my teacher, A.A. Glazov with whom I enjoyed the most my stay in Germany. Ideas borne as a result of our discussions are present in almost each chapter of this thesis.

Not to be lost completely in physics helped me my friends whom I wish also to thank: Tolik Astvatsatourov, Rezo Shanidze, Sanya Somov, Olezhka Veretine, Christopher Wiebusch, Tomas Lastovicka, Mirek Nozhicka and many others. An explicit thanks goes to Ilja Tsurin for his permanent help in preparing parties. :)

Last but not least, I am sincerely grateful to my most beloved women for their strong support and patience during the most stressed periods of the preparation of this work: mother Valentina and wife Silvia.

# Bibliography

- [1] E. Rutherford, *Phil. Mag.* **21** (1911) 669.
- [2] N.F. Mott, *Proc. Roy. Soc.* **A135** (1932) 429.
- [3] M.N. Rosenbluth, *Phys. Rev.* **79** (1950) 615.
- [4] R. Hofstadter, *Rev. Mod. Phys.* **28** (1956) 214.
- [5] M. Yearian and R. Hofstadter, *Phys. Rev.* **110** (1958) 552.
- [6] C. Moeller, *Ann. Phys.* **14** (1932) 531.
- [7] S.D. Drell and J.D. Walecka, *Ann. Phys.* **28** (1964) 33.
- [8] M. Gell-Mann, *Phys. Rev.* **125** (1962) 1067;  
Y. Ne'eman, *Nucl. Phys.* **26** (1961) 222.
- [9] M. Gell-Mann, *Phys. Lett.* **8** (1964) 214.
- [10] C. Zweig, CERN-8192/TH 401 (1964).
- [11] J.D. Bjorken, *Phys. Rev.* **148** (1966) 1467.
- [12] M. Bloom et al., *Phys. Rev. Lett.* **23** (1969) 930.
- [13] R.P. Feynman, *Phys. Rev. Lett.* **23** (1969) 1415.
- [14] C.G. Callan and D.J. Gross, *Phys. Rev. Lett.* **22** (1969) 156.
- [15] J.D. Bjorken and E.A. Paschos, *Phys. Rev.* **185** (1969) 1975.
- [16] D.J. Fox et al., *Phys. Rev. Lett.* **33** (1974) 1504.
- [17] K. Koller, T.F. Walsh et al., *Phys. Lett.* **B72** (1977) 227, Erratum-ibid. **B73** (1978) 504.
- [18] JADE Collaboration, W. Bartel et al., *Phys. Lett.* **B91** (1980) 142.
- [19] H1 Collaboration, I. Abt et al., *Nucl. Phys.* **B407** (1993) 515.
- [20] ZEUS Collaboration, M. Derrick et al., *Phys. Lett.* **B316** (1993) 412.

- [21] M. Glück, E. Reya and A. Vogt, *Z. f. Phys.* **C53** (1993) 127.
- [22] J. Kuti and V.F. Weisskopf, *Phys. Rev.* **D4** (1971) 3418.
- [23] L.N. Hand, *Phys. Rev.* **129** (1963) 1834.
- [24] V. Budnev et al., *Phys. Rep.* **C15** (1975) 181.
- [25] D.H. Perkins, *Introduction to High Energy Physics*, Addison Wesley, (1987).
- [26] D.H. Perkins, Proceedings of the 16th International Conference on High Energy Physics, Chicago-Batavia (1972), 189 (NAL, Batavia 1972).
- [27] O.W. Greenberg, *Phys. Rev. Lett.* **13** (1964) 598;  
M. Han and Y. Nambu, *Phys. Rev.* **B139** (1965) 1006.
- [28] R.K. Ellis, W.J. Stirling and B.R. Webber, *QCD and Collider Physics*, Cambridge University Press, 1996.
- [29] F. Halzen and A.D.Martin, *Quarks and Leptons*, New York, USA: Wiley (1984).
- [30] R.M. Barnett et al., *Phys. Rev.* **D54** (1996) 1.
- [31] J. C. Collins, D. E. Soper and G. Sterman, in *Perturbative Chromodynamics*, edited by A. H. Mueller (World Scientific, Singapore, 1989).
- [32] G. 't Hooft and M. Veltman, *Nucl. Phys.* **B44** (1972) 189.
- [33] Yu.L. Dokshitzer, *Sov. Phys. JETP* **46** (1977) 641;  
V.N. Gribov and L.N. Lipatov, *Sov. J. Nucl. Phys.* **15** (1972) 438 and 675;  
G. Altarelli and G. Parisi, *Nucl. Phys.* **B126** (1977) 298.
- [34] W. Van Neerven, *Deep Inelastic Lepton-Hadron Scattering as a Test of Perturbative QCD*, Proceedings of DIS'99, ed. by J. Blümlein and T. Riemann, *Nucl. Phys.* **B79** (1999) 36;  
G. Sterman, *Recent Progress in QCD*, Invited Talk at DPF'99, Los Angeles, January 1999, hep-ph/9905548, Stony Brook preprint ITB-SB-99-22(1999).
- [35] B. H. Wiik, Proceedings of the XXIV Int. Conf. on High Energy Physics, ed. Springer-Verlag, Berlin (1989) 404.
- [36] H1 Collaboration, Proceedings of the International Conference on High Energy Physics, Warsaw 1996, ICHEP96-pa17-026;  
N. Gogitidze and S. Levonian, Internal Note H1-02/96-471 (1996).
- [37] A.A. Glazov, Ph.D. Thesis, Berlin, Humboldt-University, 1998, DESY-Thesis-1998-005.
- [38] H. Abramowicz et al., *Nucl. Instr. and Meth.* **A180** (1981) 429.

- [39] H1 Collaboration, W. Braunschweig et al., Nucl. Instr. and Meth. **A265** (1988) 419.
- [40] H1 Collaboration, W. Braunschweig et al., Nucl. Instr. and Meth. **A275** (1989) 246.
- [41] H1 Collaboration, C. Adloff et al., DESY 99-107, hep-ex/9909059 (1999), Eur. Phys. J. to appear.
- [42] H1 Collaboration, PRC report 93/02 March 8, (1993).
- [43] J. Katzy, Ph.D. Thesis (in German), Heidelberg (1997).
- [44] W. Eick et al., Nucl. Instr. and Meth. **A386** (1997) 81.
- [45] H1 Spacal Group, Nucl. Instr. and Meth. **A386** (1997) 397.
- [46] H1 Spacal Group, Nucl. Instr. and Meth. **A382** (1996) 395.
- [47] H1 Spacal Group, Nucl. Instr. and Meth. **A374** (1996) 149.
- [48] Proceedings of the Workshop “Physics at HERA”, vol. 1, eds. W. Buchmüller and G. Ingelman, DESY (1992).
- [49] M. Klein, *On the  $Q^2, x$  Range at HERA*, in [48], 71.
- [50] F. Jaquet and A. Blondel, “An ep facility for Europe”, Proceedings, ed. by U. Amaldi, Hamburg (1979).
- [51] U. Bassler and G. Bernardi, Nucl. Instr. and Meth. **A361** (1995) 197.
- [52] K.C. Hoeger, *Measurement for  $x, y, Q^2$  in neutral current events*, in [48], 43; S. Bentvelsen, J. Engelen and P. Kooijman, *Reconstruction of  $(x, Q^2)$  and extraction of structure functions in neutral current scattering at HERA*, in [48], 23.
- [53] G. A. Schuler and H. Spiesberger, Proceedings of the Workshop “Physics at HERA” , Vol. 3, eds. W. Buchmüller and G. Ingelman, Hamburg, DESY (1992), 1449.
- [54] L. Lönnblad, Comp. Phys. Comm. **71** (1992) 15.
- [55] A. Kwiatkowski, H. Spiesberger and H. -J. Möhring, Comp. Phys. Comm. **69** (1992) 155.
- [56] G. Gustafson and U. Petterson, Nucl. Phys. **B306** (1988) 741; B. Andersson et al., Z. Phys. **C43** (1989) 625.
- [57] M. Glück, E. Reya and A. Vogt, Z. Phys. **C67** (1995) 433.
- [58] A. Courau and P. Kessler, Phys. Rev. **D46** (1992) 117.
- [59] G. Marchesini et al., Comp. Phys. Comm. **67** (1992) 465.

- [60] R. Engel and J. Ranft, Phys. Rev. **D54** (1996) 4244.
- [61] A. Capella, U. Sukhatme, C. I. Tan and J. Tran Thanh Van, Phys. Rep. **236** (1994) 227.
- [62] D. Eckstein, Ph.D. Thesis, Humboldt-University of Berlin, in preparation.
- [63] A. Capella, A. Kaidalov, C. Merino and J. Tran Thanh Van. Phys. Lett. **B337** (1994) 358.
- [64] H1 Collaboration, S. Abt et al., DESY preprint 93-103 (1993).
- [65] R. Brun et al., GEANT3 User's Guide, CERN-DD/EE 84-1, Geneva (1987).
- [66] M. Klein, Minutes of the Trigger Meeting, 2.09.1997.
- [67] M. Klein, A. Glazov and R. Wallny, Internal Note H1-07/98-546 (1998).
- [68] J.C. Bizot et al., Internal Note H1-04/98-538 (1998).
- [69] H.C. Schultz-Coulon et al., IEEE 1998 Nuclear Science Symposium, Toronto, Canada, November 1998. IEEE Trans. Nucl. Sci., Vol. **46** (1999) 915.
- [70] T. Kurča, Private communication.
- [71] H1 Collaboration, C. Adloff et al., *Deep-Inelastic ep Scattering at Low  $Q^2$  at HERA*, to be published.
- [72] H1 Collaboration, *Technical Proposal to build Silicon Tracking Detectors for H1*, DESY PRC 92/01, Internal Note H1-06/92-226 (1992).
- [73] N. Wulff, Internal Note H1-08/91-188 (1991).
- [74] H. Henschel et al., *Development of the H1 Backward Silicon Pad Detector*, Contribution to the International Conference on Experimentation, San Miniato, May 1996, to be published.
- [75] R. Horisberger and D. Pitzl. *A novel readout chip for silicon strip detectors with analog pipeline and digitally controled analog signal processing*. Nucl. Instr. and Meth., **A326** (1993) 92.
- [76] W. Eick et al., Nucl. Instr. and Meth. **A386** (1997) 81.
- [77] P. Kostka (author of the BST online reconstruction code), Private communication.
- [78] Th. Naumann (author of the BST offline reconstruction code), Private communication.
- [79] E. Peppel and U. Stösslein, Internal Note H1-04/97-520 (1997).
- [80] I. Abt et al., Nucl. Instr. and Meth. **A386** (1997) 310 and **A386** (1997) 348.

- [81] J. Janoth, Ph.D. Thesis (in German), Heidelberg (1997).
- [82] A. Meyer, Internal Note H1-08/96-486 (1996).
- [83] M. Dirkmann, Internal Note H1-05/96-477 (1996).
- [84] C. Arndt, Diploma Thesis (in German), Hamburg (1995).
- [85] J. Janoth et al., Internal Note H1-11/95-464 (1995).
- [86] P. Verrechia, Internal Note H1-09/95-456 (1995).
- [87] R. Wallny, Ph.D. Thesis, University of Zürich, in preparation.
- [88] V. Lendermann, Minutes of ELAN DESY PWG Meeting, April 1999.
- [89] J.P. Pharabod et al., Internal Note H1-03/96-474.
- [90] A. Zhokin and V. Efremenko, Minutes of ELAN DESY PWG Meeting, 28.7.1995.
- [91] A. Meyer, Ph.D. Thesis, Hamburg (1997).
- [92] A.A. Glazov, Private communication.
- [93] U. Bassler and G. Bernardi, Internal Software Note 51-06 (1995).
- [94] V. Shekelyan, presentation to the ELAN DESY PWG (1996).
- [95] H1 Calorimeter Group, Nucl. Instr. and Meth. **A336** (1993) 499.
- [96] V. Shekelyan, Internal Note H1-04/93-288 (1993).
- [97] H. Kuester, Internal Software Note 45-03 (1994).
- [98] A.A. Glazov, Minutes of ELAN DESY PWG Meeting, 15.09.1998.
- [99] V.V. Arkadov, Minutes of ESCALE DESY PWG Meeting, 12.06.1999.
- [100] A.A. Glazov and V.V. Arkadov, Minutes of ELAN DESY PWG Meetings, end of 1998 and beginning of 1999.
- [101] A. Arbuzov et al., HECTOR 1.00 Manual, DESY 95-185.
- [102] F. Lehner, Ph.D. Thesis, Hamburg (1999).
- [103] T.C. Awes et al., Nucl. Instr. and Meth. **A311** (1992) 130.
- [104] H1 Collaboration, S. Aid et al., Phys. Lett. **B354** (1995) 494.
- [105] V. Shekelyan and R. Wallny, Private communication.
- [106] M. Klein, to appear in Proceedings of the 19th International Symposium on Lepton and Photon Interactions at High Energies, hep-ex/0001059.

- [107] H1 Collaboration, C. Adloff et al., Nucl. Phys. **B497** (1997) 3;  
H1 Collaboration, S. Aid et al., Nucl. Phys. **B470** (1996) 3;  
H1 Collaboration, T. Ahmed et al., Nucl. Phys. **B439** (1995) 471;  
H1 Collaboration, I. Abt et al., Nucl. Phys. **B407** (1993) 575.
- [108] H1 Collaboration, C. Adloff et al., Phys. Lett. **B393** (1997) 452.
- [109] NMC Collaboration, M. Arneodo et al., Nucl. Phys. **B493** (1997) 3.
- [110] A. Cooper et al., Proc. Intern. Workshop “Physics at HERA”, Hamburg 1991, DESY, in press.
- [111] L. Bauerdick, A. Glazov and M. Klein, Proceedings of the Workshop “Future Physics at HERA”, vol. 1, eds. G. Ingelman, A. De Roeck and R. Klanner, DESY (1996) 77.
- [112] A. Bodek, to appear in proceedings of the 35th Workshop “Rencontres de Moriond”.

# Lebenslauf

## Angaben zur Person

Name: Vladimir Arkadov  
Geburt: 24.05.1973 in Novomoskovsk (UdSSR)  
Nationalität: Russisch  
Familienstand: Verheiratet  
Ehegattin: Silviya Arkadova (geb. Vassileva)  
Name des Vaters: Vladimir Arkadov  
Name der Mutter: Valentina Arkadova, geb. Dolzhikova

## Ausbildungsweg

Sep 1990 - Feb 1996 Studium an der Moskauer Ingenieur-Physikalische Universität in der Fachrichtung Experimentelle und Theoretische Physik.  
Jan 1994 - Feb 1996 Pre-diplom und Diplom Thesis im Vereinten Institut für Kernphysik, Dubna.  
Feb 1996 Diplom an der M.I.P.U.  
Sep 1996 Beginn der Dissertation bei Prof. Dr. Th. Lohse an der Humboldt-Universität zu Berlin unter Betreuung von Dr. M. Klein, DESY-Zeuthen.

## Publikationen

1. *Measurement of the Structure Functions  $F_2$  and  $F_L$  at Low  $x$ .*  
V. Arkadov, Proceedings of the 7th International Workshop on Deep Inelastic Scattering and QCD, Nucl. Phys. **B79**, 179 (1999)
2. *Deep-Inelastic ep Scattering at Low  $Q^2$  at HERA.*  
H1 Collaboration (C. Adloff et al.), to be published.

# Selbständigkeitserklärung

Hiermit erkläre ich, die vorliegende Arbeit selbständig ohne fremde Hilfe verfasst zu haben und nur die angegebene Literatur und Hilfsmittel verwendet zu haben.

Vladimir Arkadov  
15.04.00